Stratified Flows with Vertical Layering of Density: Theoretical and Experimental Study of the Time Evolution of Flow Configurations and their Stability

by
Matthew N. J. Moore

A dissertation submitted to the faculty of the University of North Carolina at Chapel Hill in partial fulfillment of the requirements for the degree of Doctor of Philosophy in the Department of Mathematics.

Chapel Hill
2010

Approved by:

Roberto Camassa, Advisor

Richard M. McLaughlin, Advisor

David Adalsteinsson, Committee Member

Laura Miller, Committee Member

Peter J. Mucha, Committee Member

Abstract

MATTHEW N. J. MOORE: Stratified Flows with Vertical Layering of Density: Theoretical and Experimental Study of the Time Evolution of Flow Configurations and their Stability.
(Under the direction of Roberto Camassa and Richard M. McLaughlin.)

A vertically moving boundary in a stratified fluid can create and maintain a horizontal density gradient, or vertical layering of density. We study an idealized two dimensional problem in which a wall moves upwards with constant speed and maintains a viscously entrained boundary layer of heavy fluid. Additionally, we study an axisymmetric analogue of this problem in which the moving wall is replaced by a moving fiber.

We construct exact solutions under the assumptions of steady-state shear flow for both the two dimensional and axisymmetric problems, in the cases in which the domain is either semi-infinite or bounded horizontally. Most attention is focused on the situation in which the density profile has a sharp transition. In the semi-infinite domain, it is found that a relationship between the size of the entrained layer and the towing speed is required to hold for a steady, shear solution to exist. The condition is found to be a result of the over-restrictive assumptions of steady flow in a semi-infinite domain and no such condition is required in the bounded domain. In the bounded domain, a two-parameter family of shear solutions is constructed after the physically-based assumption of vanishing flux is made.

We conduct experiments that successfully create the axisymmetric shear flows from an initially stable stratification. In order to determine the time evolution of the flow observed in the experiments, a lubrication model is developed and is shown to be in excellent agreement with observations. Additionally, we determine the full time evolution of the flow in the case of no stratification, and this solution is asymptotic to the experimental system for short times.

We perform stability analysis on the family of exact shear solutions in both two dimensions and the axisymmetric geometry, using asymptotic and numerical methods. The stability properties of the flow depend strongly on the size of the entrained

layer. A critical layer size is found, below which the flow configuration is stable and beyond which the flow configuration is unstable. This bifurcation is independent of the Reynolds number of the flow and the Reynolds number only affects the magnitude of the amplification or damping of disturbances.

It is found that unstable layer sizes are possible to achieve from the initial value problem of stable stratification. Layer sizes which are predicted to be unstable are observed in the experiment, however the amplification of disturbances is not observed because the rate of amplification is too small.

Experimental measurements show excellent agreement with predictions from the time dependent lubrication model over a large range of times, as well as good agreement with the homogeneous model for short times.

Acknowledgments

I would first like to thank my co-advisors, Rich and Roberto, for their guidance throughout my graduate studies. Over these five years they have provided me with the opportunities and challenges that were necessary for my intellectual growth, and they have imparted a great deal of wisdom to me. I believe that it is lucky to find a good advisor, and I consider myself blessed to have found two.

I would like to thank David Adalsteinsson, Laura Miller, and Peter Mucha for their willingness to serve on my graduate committee for over a year now. Each has provided help and advice to me at various points of my graduate studies. I want to thank Peter for his helpful suggestions regarding current research related to this thesis, in particular on instabilities in miscible fluids. I also want to thank Peter for his support as my course coordinator while I was teaching. I want to thank Laura for her important suggestions and help regarding the experimental part of this thesis as well as her willingness to loan me laboratory equipment. I want to thank David for his help with the methods used to analyze the experimental images, which was performed using his software DataTank. The image analysis became an important part of this thesis, in particular in showing the connection between the theory and the experiment, and I could not have done this part without David's help.

I would like to thank Leandra Vicci for the help she provided with the design of the experiment. I would also like to thank several people at UNC for helpful conversations and suggestions regarding various parts of the project - these people include Ashwin Vaidya, Arvind Santhanakrishnan, Keith Mertens, Brian White, and Jason Metcalfe. Additionally, I have had helpful conversations with a few professors outside of UNC including Tom Peacock, who provided suggestions for the experiment, Howard Stone, who suggested the connection to the work of Landau and Levich, Steve Childress, who provided helpful suggestions for the stability analysis, and Ray Goldstein, who informed me of some related studies.

Of utmost importance, I would like to thank several undergraduate laboratory assistants who provided invaluable assistance to the experimental component of this project while supported on the NSF RTG grant. These people are Nick Cook, Keith Grose, Mark Hemphill, David Hendel, Kiron James, Michelle Labrecque, Marshall Newman, Robert Overman, Johnny Reis, Jordan Roddy, Bailey Watson, and Kuai Yu. I would like to give particular acknowledgement to David Hendel, Marshall Newman, and Kuai Yu who contributed to presentations of this project at various meetings and conferences. Additionally Kuai Yu provided indispensable assistance with the data analysis as well as made original contributions to the analysis methods.

I would like to thank the NSF RTG that supported my graduate work - NSF RTG grant DMS-0502266.

I would like to thank the friends I have made at UNC and my family for providing me with support and humor that I needed during my graduate studies. Finally, I want to thank my wife Jessie for love, support, humor, and patience during this time. I know that I could not have accomplished this goal without her help.

Table of Contents

List of Figures

Chapter 1

Introduction

1.1 Introduction

The flow of fluid with density stratification is a topic of great interest due to its ubiquity in nature as well as its mathematical complexity. Characterization of stratified flows, and in particular the analysis of their stability, has applications in the areas of atmospheric and oceanic sciences and many industrial processes. Flows in which layers of constant density are oriented horizontally, with the gradient of density in the vertical direction, are most typical in natural settings, such as the atmosphere and the oceans, which is of course due to the role of buoyancy. The stability of such flows with primarily vertical density gradients has been studied in great depth, beginning with the seminal work of G.I. Taylor [30] and Goldstein [11]. Although perhaps less common, stratification in which the density gradient is non-vertcial can develop through many natural processes as well as industrial processes [16, 31, 33]. For the purpose of isolating the physical mechanism of non-vertical density gradients, the present study focuses on the most extreme situation in which the density gradient is in the horizontal direction, with isopycnal lines or layers of constant density oriented completely vertically. Hereafter, this orientation will be referred to as vertical density layering.

The initial motivation for this thesis was provided by the experimental and phenomenologically study [1] in which observations were made of a bead falling through a sharp, miscible stratification. The bead, which had higher density than both the top fluid and the bottom fluid, was observed to slow down considerably upon penetrating into the bottom fluid and, within a certain range of parameters, was even observed to

reverse its downward motion and rise over a short distance before ultimately descending once again. The mechanism of this levitation phenomenon was found to be a layer of top fluid entrained by the bead and carried into the bottom fluid, creating positive buoyancy in the system for a period of time. In [6], as an application of new theoretical findings, the details of this mechanism were further illuminated through the concept of fluid drift.

From the effect of entrainment, non-vertical density gradients are created in the system, both within the entrained shell surrounding the sphere as well as within the stem oriented vertically above the sphere - see Figure 1.1 for an experimental image. Furthermore the entrained shell appears to have a definite thickness which can be observed in the images, although the size of the thickness may appear distorted due to optical effects from the varying refractive index of the stratified fluid. The relationship between the thickness of the entrained shell and the other parameters of the experiment, most importantly the strength of the stratification and the rate of descent of the bead, is unknown and is one motivating question for this thesis.

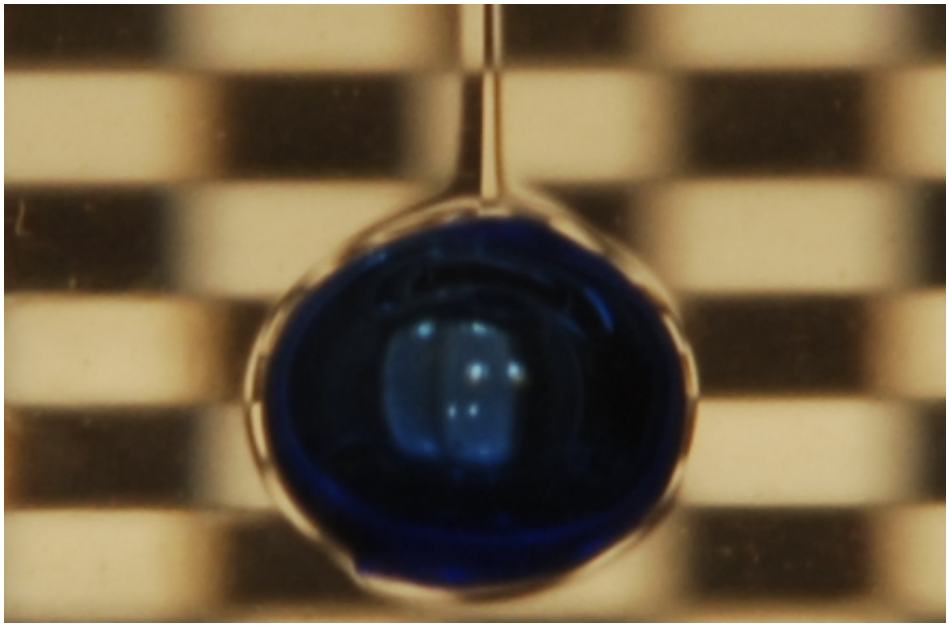

Figure 1.1: 4 mm diameter sphere with density 1.0401 g/cc falling through a sharp stratification with top density 0.9982 g/cc and bottom density 1.0386 g/cc. Based on the sphere velocity in the top layer of 7.6 cm/s and the sphere diameter, the Reynolds number is roughly 300. Upon penetrating into the bottom layer the sphere entrains a visible shell of top fluid. Image from [19]

To determine if the mechanism of vertical density layering can provide useful predictions for stratified flows such as the example above, we consider a theoretical problem in which a vertical boundary moves upwards and entrains a layer of higher density fluid. The resulting stratified flow is assumed to be layered *entirely* in the vertical direction, so as to isolate this mechanism of vertical density layering. The diffusivity of density is neglected so that the stratification may remain sharp. The focus of this thesis will be the exploration of the hydrodynamic properties of such a flow configuration - See Figure 1.2 for an illustration of the flow configuration.

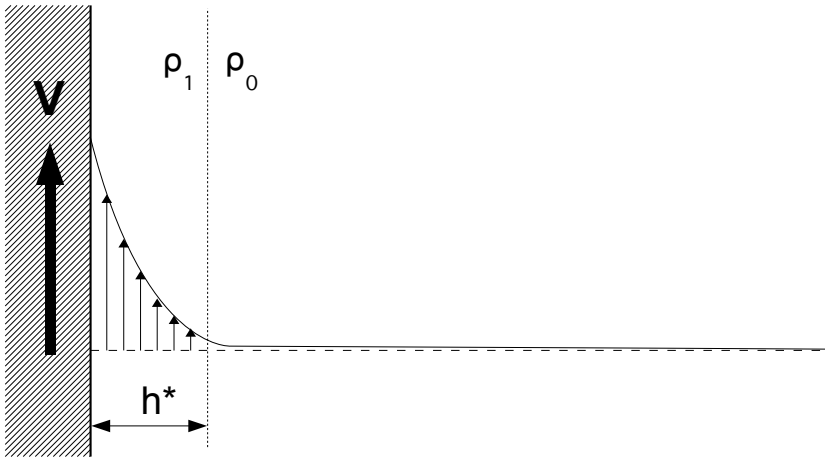

Figure 1.2: Illustration of the idealized two-dimensional flow configuration in a semi-infinite domain.

Two dimensional exact shear solutions will be found in 1.2 in which the vertical boundary is a flat wall, and axisymmetric exact shear solutions will be found in 1.3 in which the vertical boundary is a fiber. We explore the shear solutions in both a semi-infinite domain and a bounded domain. It is found that in the semi-infinite domain, a relationship between the size of the entrained layer and the towing speed is required to be met for a steady, shear solution to exist. Further analysis reveals that this relationship is only the product of the over-restrictive assumptions of steady, shear flow in an unbounded domain, and no such condition is required in a bounded domain.

Motivated by initial analysis of these exact shear solutions, an experiment was conducted to create such flow configuration for the axisymmetric case, and this will be briefly introduced in 1.4 and discussed in greater detail in Chapter 4. In the experiment the vertically layered flow develops from an initial stable stratification, and we

have developed a theoretical model to predict this time evolution using the tools of lubrication theory as well as other tools. This theoretical model bears some resemblance to the theoretical study of coating flows of Landau and Levich [14, 27], and quite possible has applications for miscible coating flows. The model will be discussed in Chapter 2 and the theoretical predictions for the time evolution of the system will be shown to be in excellent agreement with experimental observations in Chapter 4.

In Chapter 2 we also determine the exact full time evolution for the flow in the case that the density is homogeneous. This homogeneous model will be shown to be asymptotic to the stratified problem for short time, and this will be confirmed experimentally in Chapter 4.

The main theoretical finding in this thesis is the determination of the stability properties of the vertically layered flow configurations, presented in Chapter 3, using both asymptotic analysis and numerical analysis in both two dimensions and the axisymmetric geometry. The stability properties of the flow will be shown to depend strongly on the size of the layer of dense fluid that is entrained by the moving boundary. A critical layer size will be found, below which the flow configuration is stable and beyond which the flow configuration is unstable, and precise bifurcation diagrams will be presented to illustrate this. Remarkable the bifurcation properties are independent of the Reynolds number of the flow, and the Reynolds number only affects the magnitude of damping or amplification rates, similar to a result found by Yih [35] for a viscosity-stratified flow.

Motivated by the experimental study, we explore two-dimensional shear flows corresponding to a density profile that is a smooth approximation to a step-function in 1.2. In Chapter 3 we determine the effects of the smooth density transition on the stability properties of the system. In the two-dimensional case, we find that introducing the smooth density transition can slow the amplification rate of perturbations, although the flow is still unstable. Similar axisymmetric analysis would prove much more laborious and has not been performed, yet it may be reasonable to infer these qualitative results would hold in the axisymmetric geometry as well.

Related to the work in this thesis, is the study of Blanchette, Peacock, and Cousin [20], which is an investigation of the stability properties of similar flow configurations with density layered vertically, but with density diffusivity retained. The theoretical problem in this study is a flat, vertical boundary towed upwards through a stable, linear density stratification, which after a sufficient time period creates a flow in which the density gradient has a horizontal component. Since density diffusivity is retained,

the resulting steady-state density gradients are gradual. Blanchette et al. conduct an experiment to create this flow in the laboratory, and they study the stability properties of the flow experimentally as well as numerically, using a Galerkin method.

The present study differs in that density diffusivity is neglected to allow for the effects of sharp density gradients to be studied. Furthermore, asymptotic results will be presented in Chapter 3 that allow for a rigorous understanding of stability characteristics over an unbounded range of parameters. The asymptotic results will be shown to agree with numerical calculations over the parameter range that is accessible by both, and outside of this overlapping range we will have complementary results from the asymptotics and numerics.

Bearing some similarities to the experiment in this thesis is current research on the topic of selective withdrawal, in which a fluid whose viscosity and density differs with the ambient fluid is withdrawn by a suction force. Lister has investigated this problem theoretically [17], and Blanchette and Zhang have performed experiments as well as developed new theoretical models [4]. In these studies, viscous withdrawal is created by a suction force (modeled theoretically as a sink) and surface tension is a significant factor, while in this thesis the mechanism is viscous entrainment by a moving boundary with no surface tension. Nonetheless, the geometry of the interface created in both experiments show similar qualitative features.

Also related to this thesis, is the study by Pesci et al. [21] and Dombrowski et al. [10], in which a jet descends into a linear stratification at low to moderate Reynolds numbers and a coiling instability is observed and understood as a Kelvin-Helmholtz type instability.

In all of these studies [17, 4, 21, 10], density gradients are created that have a horizontal component and additional physical effects are also present in the system. The value of this thesis is the *isolation* of the mechanism of vertical density layering, in particular with sharp density transitions, and the characterization of the resulting flows.

1.2 Two dimensional exact shear solutions

Here, we give a theoretical construction of a two dimensional incompressible shear flow exhibiting vertical layering of density. The diffusivity of the density is assumed

negligible and the dynamic viscosity is assumed constant. We will be primarily interested in sharp stratifications where the density profile is either discontinuous or has a small transition region over which the density changes rapidly, however many of the results apply to arbitrary density profiles.

Consider a fluid domain unbounded in the vertical direction with a flat vertical wall placed at $x = 0$ as a boundary. Two cases will be treated: one in which the domain is bounded to the right by a wall held fixed at $x = L$ (the bounded domain) and another in which the domain is unbounded to the right as $x \to \infty$ (the semi-infinite domain). By allowing the boundary at $x = 0$ to move vertically with uniform speed V, it is possible construct the vertically layered configuration in which there exists a steady-state solution to the governing equations. As the governing equations, we will consider the incompressible Navier-Stokes system for coordinates $\mathbf{x} = (x, z)$, velocity $\mathbf{u}(\mathbf{x}, t) = (u(\mathbf{x}, t), w(\mathbf{x}, t))$ and density $\rho(\mathbf{x}, t)$

$$\begin{aligned} \rho \frac{D}{Dt}\mathbf{u} &= -\nabla p + \mu \Delta \mathbf{u} - \rho g \hat{z} \\ \nabla \cdot \mathbf{u} &= 0 \\ \frac{D}{Dt}\rho &= 0, \end{aligned}$$

where p is pressure, μ is the dynamic viscosity, g is gravity and where D/Dt is the substantive derivative

$$\frac{D}{Dt} = \frac{\partial}{\partial t} + \mathbf{u} \cdot \nabla$$

We will also consider the incompressible Boussinesq approximation

$$\begin{aligned} \frac{D}{Dt}\mathbf{u} &= -\frac{1}{\rho_0}\nabla p + \frac{\mu}{\rho_0}\Delta \mathbf{u} - \frac{g\,\rho}{\rho_0}\,\hat{z} \\ \nabla \cdot \mathbf{u} &= 0 \\ \frac{D}{Dt}\rho &= 0, \end{aligned}$$

with (constant) reference density value ρ_0. The Boussinesq approximation retains density variation only in the buoyancy term $-g\rho\hat{z}/\rho_0$, while neglecting the effects of density variation on the fluid inertia. This approximation is widely used in the theory of stratified theories for its considerable simplification of the governing equations, since the variable $\rho(\mathbf{x}, t)$ only enters into the inhomogeneous term of the momentum equation

and does not multiply any terms involving $\mathbf{u}$. This approximation will not be necessary for the derivation of the class of exact shear solutions, however it will be exploited in the stability analysis of these solutions.

The boundary conditions of the idealized problem are no-slip on all boundaries, and in the semi-infinite problem, decay of the velocity field at infinity

$$\begin{aligned} (u, w) &= (0, V) \qquad \text{at } x = 0 \\ (u, w) &= (0, 0) \qquad \text{at } x = L \text{ or as } x \to \infty \end{aligned}$$

The problem is put in non-dimensional form via the Reynolds number $Re = \rho_0 LV/\mu$ and the Froude number $Fr = V/\sqrt{gL}$, where L is a length scale which will be the location of the right bounding wall in the bounded domain or some characteristic length scale in the semi-infinite problem, and ρ_0 is a characteristic density which will be chosen later. We non-dimensionalize without changing notation

$$\begin{gathered} \frac{\mathbf{u}}{V} \to \mathbf{u} \\ \frac{\mathbf{x}}{L} \to \mathbf{x} \\ \frac{\rho}{\rho_0} \to \rho \\ \frac{tV}{L} \to t \end{gathered}$$

The non-dimensional Navier-Stokes system is given by

$$\begin{aligned} \rho\, Re \frac{D}{Dt}\mathbf{u} &= -\nabla p + \Delta \mathbf{u} - \frac{Re}{Fr^2}\,\rho\,\hat{z} \\ \nabla \cdot \mathbf{u} &= 0 \\ \frac{D}{Dt}\rho &= 0, \end{aligned}$$

and the non-dimensional Boussinesq approximation equations are

$$\begin{aligned} Re\frac{D}{Dt}\mathbf{u} &= -\nabla p + \Delta\mathbf{u} - \frac{Re}{Fr^2}\,\rho\,\hat{z} \\ \nabla\cdot\mathbf{u} &= 0 \\ \frac{D}{Dt}\rho &= 0, \end{aligned}$$

The boundary conditions become

$$(u,w) = (0,1) \qquad \text{at } x = 0 \tag{1.1}$$

$$(u,w) = (0,0) \qquad \text{at } x = 1 \text{ or as } x \to \infty \tag{1.2}$$

depending on if it is the bounded domain or the semi-infinite domain under consideration.

In order to construct a class of exact steady-state solutions with density layered vertically, assume that $\rho = \rho(x)$, and that the velocity profile is a shear flow, $(u,w) = (0,w(x))$. With these assumptions, both the Navier-Stokes equations and the Boussinesq approximation reduce to the same ordinary differential equation for the vertical velocity

$$w''(x) = \frac{Re}{Fr^2}\,(\rho(x) - 1) + \beta \tag{1.3}$$

for some non-dimensional constant β determined by the vertical pressure gradient and with the boundary conditions (1.1) and (1.2) enforced for $w(x)$. Note that the Navier-Stokes equations and the Boussinesq approximation reduce to exactly the same ordinary differential equation since both the time-derivative of velocity and the nonlinear advection term in the Navier-Stokes equations vanish under the assumptions of steady shear flow.

1.2.1 Two dimensional problem in a semi-infinite domain

General density profile

For the semi-infinite case, allow the reference density to be given by its limit to the right $\rho_0 = \lim_{x\to\infty}\rho(x)$ and allow the characteristic length-scale L undetermined for the

moment. Since the velocity decays as $x \to \infty$, the constant β must vanish and (1.3) reduces to

$$w''(x) = \frac{Re}{Fr^2}\,(\rho(x) - 1)$$

which may be solved by quadrature for an arbitrary profile $\rho(x)$.

$$w(x) = \frac{Re}{Fr^2}\int_x^\infty \int_v^\infty \rho(u) - 1 \;\; du\, dv \tag{1.4}$$

It is assumed that $\rho(x)$ tends to 1 sufficiently fast to be twice integrable, for example the condition $\lim_{x\to\infty} x^{2+\varepsilon}(\rho(x) - 1) = 0$ for $\varepsilon > 0$ is sufficient. This general solution satisfies the boundary condition to the right (1.2) and for the no-slip boundary condition at the left wall (1.1) to be satisfied the following condition for the density profile must be satisfied

$$\frac{Re}{Fr^2}\int_0^\infty \int_v^\infty \rho(u) - 1 \;\; du\, dv = 1 \tag{1.5}$$

This condition imposes a strong constraint on the semi-infinite system for there to exist a steady solution.

Two-fluid system

Consider the special case with two fluids of differing densities: ρ_0 is the density of the ambient fluid to the right (as well as the characteristic density) and ρ_1 is the higher density of the fluid entrained by the moving wall, so that the density profile is discontinuous at the the interface between the fluids positioned at h^* (dimensional), with jump $\Delta\rho = \rho_1 - \rho_0$ (dimensional). Let the characteristic length-scale L be given by the size of the entrained fluid h^*. Then the density profile in non-dimensional form is given by

$$\rho(x) = 1 + \frac{\Delta\rho}{\rho_0}\,H(1 - x)$$

where $H(x)$ is the heavy-side step function which is 0 if $x < 0$ and 1 if $x > 0$. Let the non-dimensional parameter α be given by

$$\alpha = \frac{Re}{Fr^2}\frac{\Delta\rho}{\rho_0} = \frac{g\Delta\rho\, h^{*2}}{\mu V}$$

Then the general solution for the velocity profile (1.4) becomes a piece-wise function

$$w(x) = \alpha \begin{cases} \frac{1}{2}(x-1)^2 & \text{if} \quad 0 \leq x \leq 1 \\ 0 & \text{if} \quad 1 < x < \infty \end{cases}$$

and the condition (1.5) reduces to the condition that $\alpha = 2$. Returning to dimensional parameters, this condition uniquely determines the size of the entrained layer as a function of the other parameters

$$h^* = \sqrt{\frac{2\mu V}{g\Delta\rho}} \tag{1.6}$$

Remarkably in the semi-infinite setting, it is only necessary to insist that a steady-shear solution exist in order to obtain a relationship between the towing speed and the size of the entrained layer (for a fixed viscosity and density difference). This is due to the fact the steady-state assumption and the condition that the velocity decay as $x \to \infty$ are stronger conditions than in a bounded domain, and it is noted that for a homogeneous fluid there is no such stead-state solution in a semi-infinite domain. In fact from Stokes' first problem, in which a flat wall bounding a semi-infinite fluid initial at rest is towed impulsively parallel to itself, it seen that the shear velocity profile continues to diffuse indefinitely. See [2] pp.189-190 and [22] pp. 194-196. Although the existence of a steady-state solution for a stratified fluid in a semi-infinite domain and the resulting condition for the size of the entrained layer was of initial interest to this investigation, the experimental study has disconfirmed the analogous prediction for the layer size in the axisymmetric setting and we have found no physical significance for it other than the fact that it does correctly predict the scaling of the layer size in terms of the other parameters though in error by a multiplicative factor. Therefore, we have come to regard (1.6) as a mathematical curiosity resulting from over-restrictive conditions placed on the system, and later we present an accurate condition for the determination of h^* which can be extended to the limit of the semi-infinte domain and replace prediction (1.6).

1.2.2 Two dimensional problem in bounded domain

General density profile

Consider the problem in which a fixed vertical wall bounds the fluid domain to the right and the position of the wall determines the characteristic length scale L, while the reference density is the density of the fluid adjacent to this right wall. In general the differential equation (1.3) must be solved for a free parameter β given by the gradient of pressure and there is no such reduction to eliminate this degree of freedom as there is in the semi-infinite domain. The general solution of (1.3) is given by

$$w(x) = \frac{Re}{Fr^2} \int_x^1 \int_v^1 \rho(u) - 1 \;\; du\, dv + A_1\,(x-1) + A_2\, x(x-1) \tag{1.7}$$

where A_1 and A_2 are constants with $\beta = 2A_2$. The boundary condition $w(1) = 0$ is automatically satisfied and the boundary condition $w(0) = 1$ determines A_1 as a function of the density profile.

$$A_1 = -1 + \frac{Re}{Fr^2} \int_0^1 \int_v^1 \rho(u) - 1 \;\; du\, dv$$

In order to determine the constant A_2 and obtain a unique solution for the velocity profile, we will make the physically-based assumption that net flux in the vertical direction vanishes

$$\int_0^1 w(x)dx = 0 \tag{1.8}$$

This condition will always hold for instance in an experimental tank in which there is a recirculating flow. Although the fluid recirculates, the flow may be approximately parallel along a horizontal line that is near the middle of the tank. There are other possible physically-based conditions to impose, for example enforcing that the pressure at the right wall is hydrostatic. However, the agreement obtained between the experimental observations and the theoretical predictions for the time-evolution presented in Chapter 2, which also relies on the vanishing flux condition, justifies that condition (1.8) is the correct condition to enforce to accurately model the dynamics of the experiment.

Note that in the bounded domain, even with the additional assumption of vanishing

flux, there is always a unique steady solution for the velocity profile given *any* density profile with no restriction analogous to equation (1.5) in the semi-infinite domain.

Two-fluid system

Consider a miscible two-fluid system in the bounded domain, in which a layer of size h^* of denser fluid is viscously entrained by the moving wall and let $h = h^*/L$ be the non-dimensionalized layer size. See Figure 1.3 for an illustration of the flow configuration.

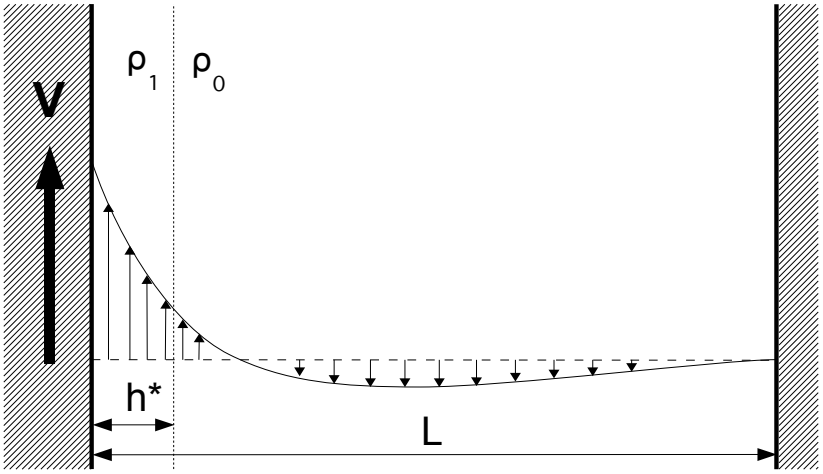

Figure 1.3: Illustration of the two-dimensional flow configuration in the bounded domain.

The non-dimensionalized density profile is given by

$$\rho(x) = 1 + \frac{\Delta\rho}{\rho_0} H(h - x) \tag{1.9}$$

Let the non-dimensional parameter κ be given by

$$\kappa = \frac{Re}{Fr^2}\frac{\Delta\rho}{\rho_0} = \frac{g\Delta\rho L^2}{\mu V}$$

The general solution for the velocity profile (1.7) reduces to

$$w(x;h) = \kappa\, w_{pw}(x;h) + A_1(h)(x-1) + A_2(h)x(x-1) \tag{1.10}$$

where the constants A_1 and A_2 now depend on h, and $w_{pw}(x;h)$ is a piecewise function given by

$$w_{pw}(x;h) = \begin{cases} \frac{1}{2}(x-h)^2 & \text{if} \quad 0 \le x \le h \\ 0 & \text{if} \quad h < x \le 1 \end{cases}$$

$A_1(h)$ is determined by enforcing the boundary condition $w(0) = 1$, giving

$$A_1(h) = -1 + \frac{1}{2}\kappa h^2$$

and $A_2(h)$ is determined by enforcing the condition of vanishing flux (1.8), giving

$$A_2(h) = 3 - \frac{3}{2}\kappa h^2 + \kappa h^3$$

It is again emphasized that there is no conditional relationship between κ and h analogous to (1.6) for there to be a steady solution, as a unique steady solution exists for any such choice of κ and h in the bounded domain. With κ and h both arbitrary, we have therefore obtained a two-parameter family of exact shear solutions exhibiting vertical density layering.

The streamfunction ψ is related the velocity componentes by $w = \partial\psi/\partial x$ and $u = -\partial\psi/\partial z$. The stream-function corresponding to the family of exact solutions (1.10) is given by

$$\psi(x;h) = \kappa\, \psi_{pw}(x;h) + \frac{1}{2}A_1(h)(x-1)^2 + \frac{1}{6}A_2(h)(2x^3 - 3x^2 + 1) \tag{1.11}$$

where

$$\psi_{pw}(x;h) = \begin{cases} \frac{1}{6}(x-h)^3 & \text{if} \quad 0 \le x \le h \\ 0 & \text{if} \quad h < x \le 1 \end{cases}$$

See Figure 1.4 for a plot of the stream-function and velocity profile for this exact

solution.

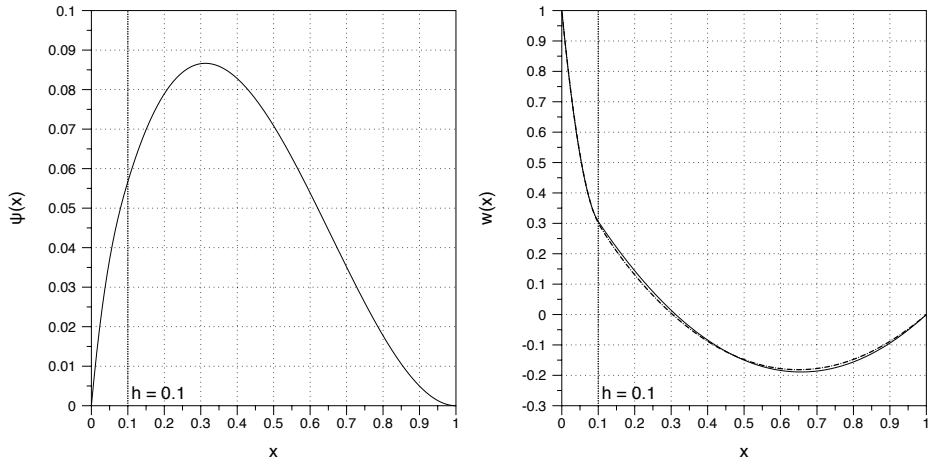

Figure 1.4: Plot of the stream-function (1.11) and velocity profile (1.10) with $\kappa = 100$ and $h = 0.1$. Also plotted in the right panel is the velocity profile (1.13) corresponding to a smoothed density profile with $\lambda = 0.04\,h$ (dot-dash line) which lies very close to the solid line.

Smoothed density transition

It is desirable to investigate the effects of introducing a smooth transition between the two fluid layers in the configuration above, particularly in light of the fact that in the experiment miscible fluids are used and therefore there is some amount of mixing that occuring between the two fluids. In the experiment, care is taken to confine this transitional region as small as possible, and it is general much smaller than the entire size of the entrained layer of denser fluid. Therefore we would like to investigate the flow in which the fluid density is approximately a step-function with the sharp change in density located at $x = h$ as before, however with a smooth transition introduced which is confined to a region with non-dimensional length-scale λ, where $\lambda \ll h$.

Perhaps the most canonical functional form to smoothly approximate a step-function is either a hyperbolic tangent or an error function. The error function has the advantage that it can be used to construct a similarity solution to the diffusion equation which would carry some physical significance here since the density does diffuse, although on a long time-scale. However, in order to solve for the velocity profile two quadratures must be taken of the density profile, and this is not available in closed form for either

the hyperbolic tangent function or the error function. Therefore, we instead employ and arctangent functional form for the density profile so that the velocity profile may be obtained in closed form. Let the density profile be given by

$$\rho(x) = 1 - \frac{\Delta\rho}{\rho_0}\left(\frac{1}{\pi}\arctan\left(\frac{x-h}{\lambda}\right) - \frac{1}{2}\right) \tag{1.12}$$

The differential equation for the velocity profile (1.3) becomes

$$w''(x) = \beta - \kappa\left(\frac{1}{\pi}\arctan\left(\frac{x-h}{\lambda}\right) - \frac{1}{2}\right)$$

The exact solution to this differential equation can be written in closed form as

$$\begin{aligned} w(x) =& A_0(h,\lambda) + A_1(h,\lambda)\,(x-1) + A_2(h,\lambda)\,x(x-1) \\ &- \frac{\kappa}{2\pi}\left((x-h)^2 - \lambda^2\right)\arctan\left(\frac{x-h}{\lambda}\right) \\ &+ \frac{\kappa\lambda}{2\pi}(x-h)\log\left(1 + \frac{(x-h)^2}{\lambda^2}\right) \end{aligned} \tag{1.13}$$

where the coefficients A_0, A_1, and A_2 are chosen to satisfy the boundary conditions and the vanishing net flux condition. Solving for A_0 by enforcing $w(1) = 0$ gives

$$A_0(h,\lambda) = \frac{\kappa}{2\pi}\left((1-h)^2 - \lambda^2\right)\arctan\left(\frac{1-h}{\lambda}\right) - \frac{\kappa\lambda}{2\pi}(1-h)\log\left(1 + \frac{(1-h)^2}{\lambda^2}\right)$$

Solving for A_1 by enforcing $w(0) = 1$ gives

$$A_1(h,\lambda) = -1 + A_0(h,\lambda) + \frac{\kappa}{2\pi}(h^2 - \lambda^2)\arctan\frac{h}{\lambda} - \frac{\kappa\lambda h}{2\pi}\log\left(1 + \frac{h^2}{\lambda^2}\right)$$

Finally, A_2 is obtained by enforcing the vanishing flux condition. For convenience we define the quantities

$$I_1(h,\lambda) \equiv 3\int_0^1 \left((x-h)^2 - \lambda^2\right)\arctan\left(\frac{x-h}{\lambda}\right)dx$$

and

$$I_2(h,\lambda) \equiv 2\int_0^1 (x-h)\log\left(1+\frac{(x-h)^2}{\lambda^2}\right)dx$$

These quantities are given in closed form by

$$I_1(h,\lambda) = (x-h)\left((x-h)^2-3\lambda^2\right)\arctan\left(\frac{x-h}{\lambda}\right)\Bigg|_0^1 - \frac{\lambda}{2}(1-2h) + 2\lambda^3\log\left(\frac{(1-h)^2+\lambda^2}{h^2+\lambda^2}\right)$$

and

$$I_2(h,\lambda) = (x-h)^2\log\left(1+\frac{(x-h)^2}{\lambda^2}\right)\Bigg|_0^1 + 2h - 1 + \lambda^2\log\left(\frac{(1-h)^2+\lambda^2}{h^2+\lambda^2}\right)$$

The coefficient A_2 can be expressed in terms of these quantities as

$$A_2(h,\lambda) = 6A_0(h,\lambda) - 3A_1(h,\lambda) - \frac{\kappa}{\pi}I_1(h,\lambda) + \frac{3\kappa\lambda}{2\pi}I_2(h,\lambda)$$

See Figure 1.5 for plots of these density and velocity profiles as compared to the density and velocity profiles obtained in the two-fluid system. The comparison of the full velocity profiles is shown in the right panel of 1.4, and a zoom of this plot near the towed boundary is shown in the right panel of 1.5 so that the velocity profiles can be discerned.

1.3 Three dimensional axisymmetric shear solutions

Now consider the axisymmetric analog of the above problem, in which the flat wall is replaced by an axisymmetric fiber of radius a^* that is towed vertically through the fluid at speed V entraining a layer of higher density fluid. We will again consider both cases in which the fluid domain is unbounded exterior to the fiber in the radial direction, and the case in which an exterior cylinder of radius L bounds the annular fluid domain.

Here, the axisymmetric coordinates are the radial coordinate r and the vertical

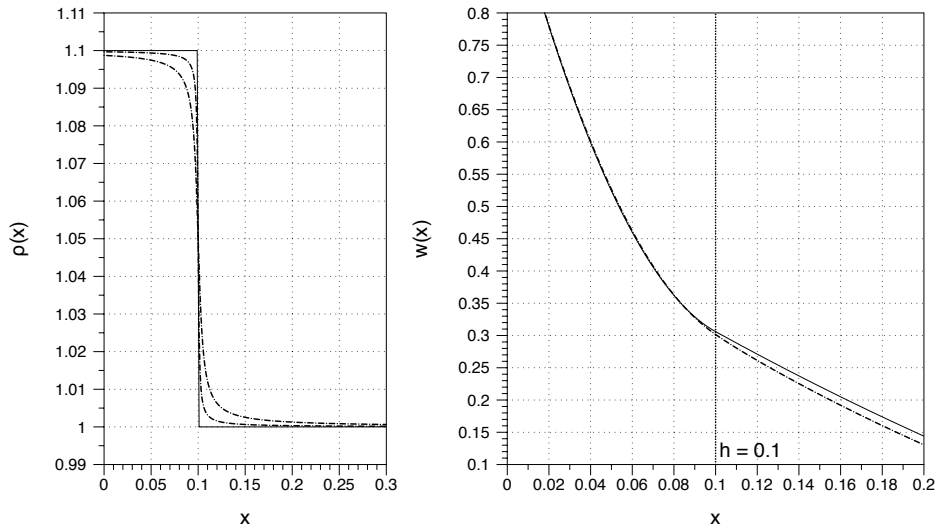

Figure 1.5: Left panel: the density profile (1.12) with $\lambda = 0$ (solid line), $\lambda = 0.01\,h$ and $\lambda = 0.04\,h$ (dot-dash lines). Right panel: a zoom of the corresponding velocity profiles (1.13) for small x, with $\lambda = 0$ (solid line), and $\lambda = 0.04\,h$ (dot-dash line). In all plots $\kappa = 100$ and $h = 0.1$.

coordinate z, with corresponding velocity components u_r and w respectively. The variables are non-dimensionalized, and $a = a^*/L$ is the non-dimensional fiber radius. The non-dimensional axisymmetric Boussinesq approximation equations are given by momentum equations

$$Re\left(\frac{\partial u_r}{\partial t} + u_r\frac{\partial u_r}{\partial r} + w\frac{\partial u_r}{\partial z}\right) = -\frac{\partial p}{\partial r} + \frac{1}{r}\frac{\partial}{\partial r}\left(r\frac{\partial u_r}{\partial r}\right) + \frac{\partial^2 u_r}{\partial z^2} - \frac{1}{r^2}u_r$$
$$Re\left(\frac{\partial w}{\partial t} + u_r\frac{\partial w}{\partial r} + w\frac{\partial w}{\partial z}\right) = -\frac{\partial p}{\partial z} + \frac{1}{r}\frac{\partial}{\partial r}\left(r\frac{\partial w}{\partial r}\right) + \frac{\partial^2 w}{\partial z^2} - \frac{Re}{Fr^2}\,\rho$$

along with incompressibility

$$\frac{1}{r}\frac{\partial}{\partial r}\left(r u_r\right) + \frac{\partial w}{\partial z} = 0$$

and conservation of mass

$$\frac{\partial \rho}{\partial t} + u_r\frac{\partial \rho}{\partial r} + w\frac{\partial \rho}{\partial z} = 0$$

and the boundary conditions

$$(u_r, w) = (0, 1) \qquad \text{at } x = a \tag{1.14}$$

$$(u_r, w) = (0, 0) \qquad \text{at } x = 1 \text{ or as } x \to \infty \tag{1.15}$$

The second boundary conditions depends on whether the bounded domain or the semi-infinite domain is considered. Under the assumptions of steady shear, the Boussinesq approximation reduces to the ordinary differential equation for $w(r)$

$$w''(r) + \frac{1}{r} w'(r) = \frac{Re}{Fr^2} \left(\rho(r) - 1\right) + \beta \tag{1.16}$$

with the same boundary conditions (1.14) and (1.15) enforced for $w(r)$.

1.3.1 Axisymmetric problem in semi-infinite domain

In the semi-infinite domain the constant β must vanish due to the constraint that the velocity field decays as $x \to \infty$, and the solution of (1.16) can be expressed in terms of quadratures

$$w(r) = \frac{Re}{Fr^2} \int_r^\infty \frac{1}{v} \int_v^\infty \left(\rho(u) - 1\right) \, u \, du \, dv \tag{1.17}$$

Enforcing that boundary condition $w(a) = 1$ results in the following constraint on the density profile for a stead-state solution to exist in the semi-infinite domain

$$\frac{Re}{Fr^2} \int_a^\infty \frac{1}{v} \int_v^\infty \left(\rho(u) - 1\right) \, u \, du \, dv = 1 \tag{1.18}$$

For the special case of a two-fluid system with density discontinuity $\Delta\rho = \rho_1 - \rho_0$ positioned at h^* (dimensional) which is taken as the characteristic length-scale $L = h^*$, the non-dimensionalized density profile becomes

$$\rho(r) = 1 + \frac{\Delta\rho}{\rho_0} H(1 - r)$$

Let the non-dimensional parameter α be given by

$$\alpha = \frac{Re}{Fr^2}\frac{\Delta\rho}{\rho_0} = \frac{g\Delta\rho\, h^{*2}}{\mu V}$$

Then the general solution for the velocity profile (1.17) reduces to

$$w(r) = \frac{\alpha}{4}\begin{cases} r^2 - 1 - 2\log r & \text{if} \quad a \le r \le 1 \\ 0 & \text{if} \quad 1 < r < \infty \end{cases}$$

and the constraint (1.18) simplifies to $\alpha\left(-2\log a - 1 + a^2\right) = 4$. In terms of dimensional quantities this constraint is

$$\frac{g\Delta\rho\, h^{*2}}{\mu V}\left(-2\log\frac{a^*}{h^*} - 1 + \frac{a^{*2}}{h^{*2}}\right) = 4 \tag{1.19}$$

Thus, just as in the two-dimensional problem, a condition on the size of the entrained layer is necessary for there to exist a steady-state solution and again this is due to the over-restrictive nature of the assumptions of steady shear flow in unbounded domains. As aforementioned an experiment was performed to approximately create axisymmetric shear flows with vertical density layering and the experimental measurements disconfirm this semi-infinite domain theoretical prediction for the size of the entrained layer. The semi-infinite prediction correctly captures the scaling of h^* relative to the other parameters, but is in error by a multiplicative constant. Later in this thesis, theory for the time-evolution of the system from the initial value problem will be presented which correctly predicts this multiplicative constant and is in agreement with experimental measurements.

1.3.2 Axisymmetric problem in bounded domain

Consider the problem in which an exterior cylinder, whose radius will be taken as the characteristic length-scale L encloses an annular fluid domain, with the fiber being towed vertically through the interior of the domain as before. As in the semi-infinite setting, the velocity profile can be represented by quadratures for any given density

profile

$$w(r) = \frac{Re}{Fr^2} \int_r^1 \frac{1}{v} \int_v^1 (\rho(u) - 1)\ u\, du\, dv + A_1 \log r + A_2(r^2 - 1) \tag{1.20}$$

where A_1 and A_2 are constants. This solution automatically satisfies the no-slip boundary condition on the exterior cylinder $w(1) = 0$, and A_1 and A_2 are determined by enforcing the no-slip boundary condition on the fiber $w(a) = 1$ as well as the vanishing flux condition for the axisymmetric domain

$$\int_a^1 w(r)\, r\, dr = 0 \tag{1.21}$$

Therefore in the bounded domain, for an arbitrary density profile there exists a corresponding unique steady shear velocity profile.

Now consider the special case of a two-fluid system with density difference $\Delta\rho = \rho_1 - \rho_0$ and with h^* the position of the interface so that $h^* \geq a^*$ must hold. The corresponding non-dimnensional interface position is $h = h^*/L$ and $h \geq a$ must hold. The general shear velocity profile (1.20) becomes

$$w_0(r; a, h) = \kappa w_{pw}(r; a, h) + A_1(a, h) \log r + A_2(a, h)(r^2 - 1) \tag{1.22}$$

where the constants A_1 and A_2 depend on both a and h and $w_{pw}(r; h)$ is the piece-wise function

$$w_{pw}(r; a, h) = \frac{1}{4} \begin{cases} r^2 - h^2 - h^2 \log \frac{r^2}{h^2} & \text{if} \quad a \leq r \leq h \\ 0 & \text{if} \quad h < r < 1 \end{cases}$$

We define the following for parameters convenience

$$\eta^2(a, h) = h^2 \left(\log \frac{h^2}{a^2} - 1 \right) + a^2 \tag{1.23}$$

$$\mu(a) = 1 + \log a - 2a^2 + a^4(1 - \log a) \tag{1.24}$$

It is straightforward to check that $\eta^2 \geq 0$ as long as $h \geq a$, by checking that the derivative of η^2 with respect to h^2 is non-negative for $h \geq a$ and by the fact that if

$h = a$ then $\eta^2 = 0$. Enforcing the boundary condition $w(a) = 1$ and the vanishing flux condition (1.21), gives the coefficients $A_1(a,h)$ and $A_2(a,h)$ in terms of these parameters

$$\begin{aligned}\mu A_1(a,h) =& 1 - \frac{\kappa}{4}\eta^2 - 2a^2 + \frac{\kappa}{4}(h^2 - a^2)^2 \\ &+ a^2\left(a^2 - \frac{\kappa}{4}h^2\left(h^2 - a^2 - a^2\log\frac{h^2}{a^2}\right)\right)\end{aligned}$$

$$\mu A_2(a,h) = -1 + \frac{\kappa}{4}\eta^2 + a^2 - 2a^2\log a - \frac{\kappa}{4}\left(a^2\eta^2 - (h^2 - a^2)^2\log a\right)$$

Thus as in the two-dimensional problem, in the bounded domain there is no additional condition required for a steady solution to exist, and we have a two-parameter family of exact shear solutions parameterized by κ and h.

In the axisymmetric problem the stream function $\psi(r,z,t)$ is related to the velocity components through

$$\begin{aligned} w &= \frac{1}{r}\frac{\partial\psi}{\partial r} \\ u_r &= -\frac{1}{r}\frac{\partial\psi}{\partial z}\end{aligned}$$

The stream function corresponding to the family of exact solutions (1.22) is given by

$$\psi(r;a,h) = \kappa\psi_{pw}(r;a,h) + \frac{1}{4}A_1(1 - r^2 + 2r^2\log r) + \frac{1}{4}A_2(r^2 - 1)^2 \tag{1.25}$$

where

$$\psi_{pw}(r;a,h) = \frac{1}{16}\begin{cases} r^4 - h^4 - 4h^2r^2\log\frac{r}{h} & \text{if} \quad a \le r \le h \\ 0 & \text{if} \quad h < r < 1 \end{cases}$$

See Figure 1.6 for a plot of the stream-function and velocity profile.

Notice that compared to the two-dimensional velocity profile shown in Figure 1.4, the negative component of the axisymmetric velocity profile need not be as strong in order to cancel with the positive component and satisfy the vanishing flux condition due to the axisymmetric $r\,dr$ integration element.

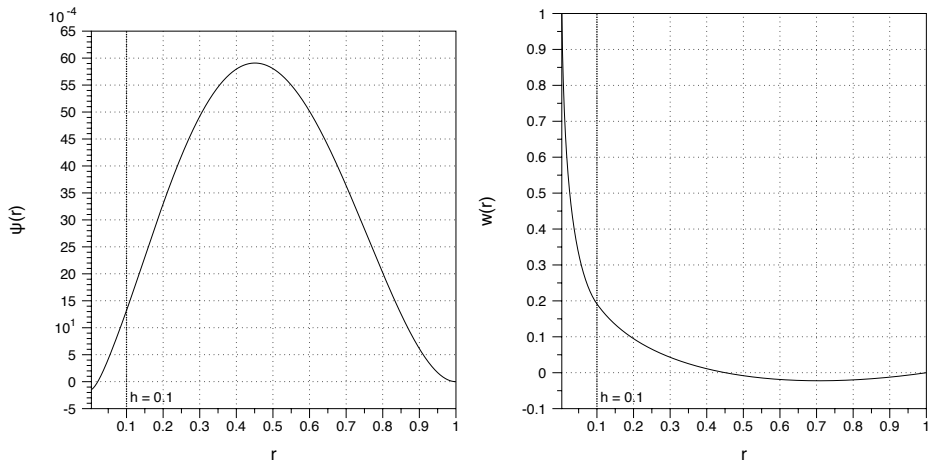

Figure 1.6: Stream-function (1.25) and velocity profile (1.22) with $\kappa = 25$, $a = 0.004$, and $h = 0.1$.

1.4 Experimental investigation

Motivated by the preliminary analysis of shear solutions, we designed an experiment to create the vertically layered flow configuration in the axisymmetric context. In the experiment, a narrow fiber is towed vertically through an initially stable stratification, entraining a layer of high density fluid and carrying it upwards. The initial stratification is sharp (with a transition region typically much less than 1 cm) and a dynamic interface between the entrained high density fluid and the ambient fluid is created. After a sufficient period of time (typically less than a minute), the interface becomes nearly vertical in a large portion of the experimental tank, suggesting the successful creation of a parallel flow. Figure 1.7 shows a sequence of experimental images in which a solution of corn-sryup and water is used. The bottom batch also has salt added to increase its density and dye added to make it visible.

In the experiment shown in Figure 1.7, the viscosity is roughly 30 Poise as measured with a falling sphere viscometer. We use 15 lb or 30 lb test monofilament fishing line as the fiber and it is towed with the SureStep 23055 stepper motor. Additional experimental details are provided in Chapter 4.

The experimental observations of the dynamic evolution of the interface, as it approaches the vertical configuration, motivated the development of a theoretical model to describe the creation of the shear flows from an initial value problem in which the fluid is at rest and stably stratified. This model is presented in Chapter 2, and

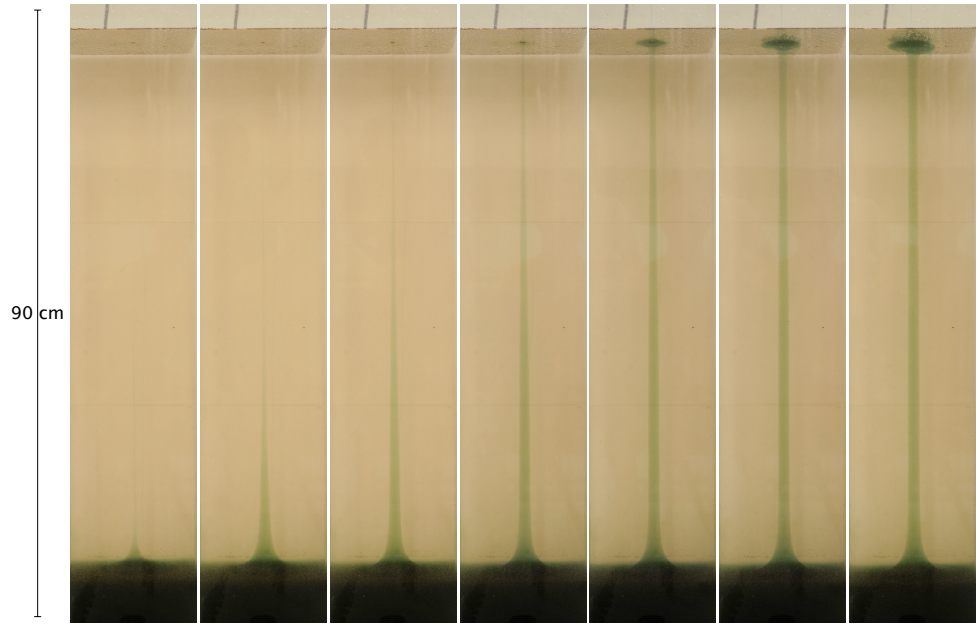

Figure 1.7: A fiber of radius $a^* = 0.019$ cm is towed upwards at 1.7 cm/s through stratified corn syrup with top density 1.41 g/cc and bottom density 1.38 g/cc, and entrains a layer of the dyed bottom fluid. Reynolds number is roughly 0.7 and $\kappa = 49$. Time between successive images is 20 seconds.

Chapter 4 documents excellent agreement between the theoretical predictions and the experimental observations. This agreement justifies the physically based assumption of vanishing vertical flux (1.8) and (1.21) used in the construction of the class of shear solutions (1.10) and (1.22) in the bounded domain. Additionally, the predictions provided by the semi-infinite analysis do not match experimental measurements since in the experiment the external boundary serves to create the vanishing flux condition which is not satisfied by the semi-infinite velocity profiles.

The condition of vanishing vertical flux holds to a close approximation in the experiment, with a small deviation occurring during a transient period in which the height of fluid in an auxiliary chamber lowers and the height of fluid in the main chamber rises as the fiber is towed upwards through the main chamber and downwards through the auxiliary chamber. Once the shear stress imposed by the fiber on the fluid balances the pressure head differential between the auxiliary chamber and the main chamber, the vanishing flux condition holds to an even closer approximation with the only deviation being from the small amount of fluid attached to the fiber and pulled completely out of the experimental tank.

The duration of the experiment varied with the viscosity and density values used, but was always less than 20 minutes and most typically roughly 5 minutes. We have experimentally measured an upper bound on the diffusivity of salt in corn syrup solutions of $1.3 \times 10^{-5}\text{cm}^2/\text{s}$ - see the Appendix B. Assuming this diffusivity value, the region of strong density transition can grow to no more than 0.12 cm after 20 minutes, which is much smaller than the typical size of the entrained layer which is on the order of 1 cm. This provides justification to the assumption that the diffusivity of density can be neglected.

Additionally, the flow configuration in the experiment does not create enhanced diffusivity in the horizontal direction. In pipe flow an enhanced diffusivity is created in the direction parallel to the flow [29]. However, in the experiments conducted here, layers of constant density are oriented vertically, parallel to the flow, and therefore the flow can only potentially enhance diffusion in this vertical direction (if at all). Therefore, if this effect of enhanced diffusivity is present, it does not occur in the direction that would increase the size of the sharp density transition.

Chapter 2

Time Evolution

Motivated by experimental observations of the evolving interface, we have developed a theoretical model to describe the time evolution of the system from an initial value problem in which the stratification is stable. Here we focus on the situation in which the density profile is discontinuous, so that two fluids are divided by a miscible interface, and diffusion across this interface is neglected. As the boundary (a flat wall in two dimensions or a fiber in three dimensions) is towed upwards it viscously entrains a boundary layer of higher density fluid. If the domain is unbounded in the vertical direction, then the flow is approximately parallel far away from the miscible fluid interface. On the other hand if the domain is bounded vertical, for instance by a flat rigid surface above and below, a recirculating flow will develop from the towing of the boundary as the flux across any imaginary surface in the domain must necessarily vanish. If the height of the domain is sufficiently large as compared to the width of the domain, then the flow can by approximately parallel throughout a large region of the domain excluding the very top and the very bottom of the domain in which there will be horizontal flow. Additionally, the vertical flux across any horizontal plane will vanish justifying the vanishing flux conditions (1.8) and (1.21) placed on the steady, shear solutions.

In the case of the experiment in which fluid domain is bounded above by a free-surface instead of a rigid surface, this condition of vanishing flux does not hold exactly in order to allow for transient motion of the free-surface as well as a pressure head differential between the auxiliary chamber and the main chamber. However, assuming that the free-surface motion is small (relative to the width of the domain for instance),

the vanishing flux condition will hold to a close approximation during this transient period. Once the pressure head differential and the free-surface become steady the condition holds to an even closer approximation, with the only deviation being the small amount of corn syrup that is attached to the fiber and is removed completely from the experimental tank.

In Section 2.1 Lubrication theory is used in order to determine the evolution of the flow and of the miscible interface under certain suitable conditions. The lubrication approximation simplifies the governing system of partial differential equations through the assumption that the flow is nearly parallel, with the variation in the flow being much stronger in the direction perpendicular to the flow than in the parallel direction - see [2] pp. 218. In order to use the lubrication approximation, we assume that after some amount of time the moving boundary has developed a sufficiently large entrained layer so that the miscible interface is oriented nearly vertically through a large portion of the domain, and in addition the flow is nearly parallel in that region. The lubrication approximation is not valid for shorter times when the miscible interface is close to its initial horizontal orientation, or for any times in the region of the domain that is near the position initial horizontal interface, as the interface will always be highly curved in this region.

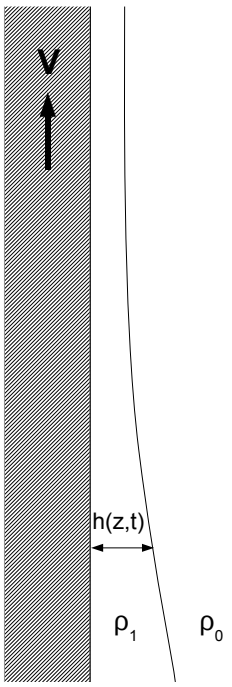

Figure 2.1: Illustration of the lubrication assumption.

In Section 2.2, we determine the full time evolution for the system in which the density is homogeneous and the domain is unbounded vertically so that the flow is parallel for all time. This problem is analogous to Stokes' first problem - see [2] pp.189-190 and [22] pp. 194-196 - except in a bounded domain and with the constraint of vanishing flux (1.8) and (1.21), which makes it a nontrivial modification. The resulting time dependent solution that describes the evolution of a material surface within the homogeneous fluid, will be asymptotic to the evolution of the interface in the stratified fluid in the limit of vanishing density difference, as well as the limit of short time. Since the lubrication approximation is not valid for short time, this homogeneous model provides a complementary description for the time-evolution of the system.

In Chapter 4 the lubrication model will be shown to be in excellent agreement with

experimental observations. The homogeneous density model will demonstrate good agreement for very short times, while departing from the experimental observations for longer times.

2.1 Lubrication theory

2.1.1 Two dimensional lubrication theory

In the non-dimensional exact shear solution (1.10) a vertically flat, miscible interface located at $x = h$ divides two fluids of differing densities. As a generalization allow the miscible interface to be given by $x = h(z,t)$. Assume a nearly parallel flow so that h is a slowly varying in the vertical direction.

$$\frac{\partial h}{\partial z} = O(\varepsilon) \ll 1$$

Assume the following expansion for the velocities compenents

$$\begin{aligned} w(x,z,t) &= w_0(x;h(z,t)) + \varepsilon\, w_1(x;h(z,t)) && (2.1)\\ u(x,z,t) &= 0 + \varepsilon\, u_1(x;h(z,t)) && (2.2) \end{aligned}$$

The density profile is given by a step-function

$$\rho(x,z,t) = 1 + \frac{\Delta\rho}{\rho_0}\, H(h(z,t) - x) \tag{2.3}$$

The non-dimensional Boussinesq approximation equations in component form are given by

$$\begin{aligned} Re(u_t + uu_x + wu_z) &= -p_x + u_{xx} + u_{zz} && (2.4)\\ Re(w_t + uw_x + ww_z) &= -p_z + w_{xx} + w_{zz} - \frac{Re}{Fr^2}\rho && (2.5)\\ u_x + w_z &= 0 && (2.6)\\ \rho_t + u\rho_x + w\rho_z &= 0 && (2.7) \end{aligned}$$

The only component which is not zero to leading order in ε is the equation for vertical momentum, which reduces to the ordinary differential equation for w_0

$$w_0{}''(x;h) = \frac{Re}{Fr^2}\left(\rho(x;h) - 1\right) + \beta$$

This is the same as equation (1.3) with parametric dependence on h made explicit. The solution is given by

$$w_0(x;h(z,t)) = \kappa\, w_{pw}(x;h) + A_1(h)(x-1) + A_2(h)x(x-1) \tag{2.8}$$

which is identical to the shear flow solution (1.10) with the only difference being that here $h = h(z,t)$. Imposing the boundary conditions and the vanishing flux condition gives the exact same expressions for the coefficients $A_1(h)$ and $A_2(h)$ as was found for the shear solution.

A hyperbolic partial differential equation governing the evolution of the miscible interface $h(z,t)$ may be derived in two different ways. First, consider the $O(\varepsilon)$ term of the incompressibility equation (2.6), in light of the expansion (2.1) and (2.2). This yields

$$-\varepsilon u_1 = \frac{\partial h}{\partial z}\int_0^x \frac{\partial}{\partial h} w_0(s;h)\, ds$$

Now, consider the $O(\varepsilon)$ term of the density advection (2.7) with the density profile (2.3) inserted. This gives

$$\frac{\Delta\rho}{\rho_0}\,\delta(x-h)\left(\frac{\partial h}{\partial t} - \varepsilon u_1 + w_0\frac{\partial h}{\partial z}\right) = 0$$

Inserting u_1 and evaluating at $x = h$ gives the hyperbolic partial differential equation for $h(z,t)$

$$\frac{\partial h}{\partial t} + \left(w_0(h;h) + \int_0^h \frac{\partial}{\partial h} w_0(s;h)\, ds\right)\frac{\partial h}{\partial z} = 0 \tag{2.9}$$

The second method to derive this partial differential equation for $h(z,t)$ does not depend on the asymptotic corrections to the Boussinesq approximation equations, but rather relies on a simple balance of fluxes along with incompressibility. Consider a narrow control volume of the denser entrained fluid, bounded below by z_1 and above

by z_2, bounded to the left by $x = 0$ and to the right by the extent of the entrained layer $x = h$. The volume of the control region is given by

$$V_c \equiv \int_{z_1}^{z_2} h(z,t)dz$$

The vertical flux within this control region across any horizontal line is given by

$$F(z,t) \equiv \int_0^{h(z,t)} w(s,z,t)ds$$

The time rate of change of the total volume of the control region must be balanced by the vertical flux through lines $z = z_1$ and $z = z_2$, as given by

$$\frac{dV_c}{dt} + F(z_2) - F(z_1) = 0$$

Passing to the limit $\Delta z = z_2 - z_1 \to 0$, gives

$$\frac{\partial}{\partial t}h(z,t) + \frac{d}{dz}F(z,t) = 0 \tag{2.10}$$

Now define $J(h)$ as the vertical flux, to leading order in the lubrication approximation, within the entrained layer

$$J(h) \equiv \int_0^h w_0(s;h)ds \tag{2.11}$$

Therefore, $J(h(z,t)) = F(z,t)$ to leading order in ε, and substitution of this relationship into (2.10), gives the hyperbolic partial differential equation

$$\frac{\partial h}{\partial t} + \frac{dJ}{dh}\frac{\partial h}{\partial z} = 0 \tag{2.12}$$

Computing dJ/dh from the definition (2.11), shows that this is exactly the same hyperbolic partial differential equation (2.9) as derived from the asymptotic corrections to the Boussinesq approximation equations.

The partial differential equation (2.12) requires an initial condition and so in sub-

sequent discussion assume the initial condition is given by $h(z,0) = f(z)$ for some function satisfying the lubrication assumption that df/dz is small.

Characteristics

Computing $J(h)$ directly from its definition (2.11) gives

$$J(h) = \frac{1}{3}h(1-h)^2(3-\kappa h^2+\kappa h^3)$$

and computing the derivative with respect to h gives

$$\frac{dJ}{dh} = 1 - 4h + 3h^2 - \kappa h^2\left(1 - 4h + 5h^2 - 2h^3\right) \tag{2.13}$$

With dJ/dh made explicit, the method of characteristics can by applied to the hyperbolic partial differential equation (2.12). Along characteristic curves, allow $z = z(t)$ with $dz/dt = dJ/dh$. Then computing the total derivative of h with respect to time gives

$$\frac{dh}{dt} \equiv \frac{\partial h}{\partial t} + \frac{\partial h}{\partial z}\frac{dz}{dt} = \frac{\partial h}{\partial t} + \frac{dJ}{dh}\frac{\partial h}{\partial z}$$

which vanishes due to the partial differential equation (2.12). Therefore $h(t) = h(z(t),t)$ is constant along characteristic curves, and the differential equation for $z(t)$ may be solved in closed form, yielding the characteristic map

$$z(t) = z_0 + t\,\left(1 - 4h_0 + 3h_0^2 - \kappa h_0^2\left(1 - 4h_0 + 5h_0^2 - 2h_0^3\right)\right) \tag{2.14}$$

where $h_0 \equiv f(z_0)$.

In order to obtain an explicit solution to (2.12) the characteristic map would need to be inverted explicitly, which would prove intractable even for very simply initial conditions due to the fact that h_0 enters (2.14) as a quintic polynomial. However, the long-time behavior of the system my be determined by simply evaluating the root structure of dJ/dh. Let h_∞ be defined as the long-time limiting layer size $h_\infty \equiv \lim_{t\to\infty} h(z,t)$ if it exists. For suitable initial conditions, it can be expected that $h(z,t)$ will tend to a root of dJ/dh in long-time, since the characteristics travel with speed

zero at such a root. Certainly initial conditions exists for which $h(z,t)$ does not tend to such a root, for instance if the solution shocks, or if the initial condition is trivial such as $f(z) = c$ for a constant c that is not a root of dJ/dh, or if the initial condition is such that $dJ/dh(f(z))$ is nowhere zero. However, for a large variety of initial conditions with $dJ/dh(f(z)) = 0$ for some z, h_∞ exists and is given by a root of dJ/dh.

A root of (2.13) must satisfy

$$\kappa h^2(1 - 4h + 5h^2 - 2h^3) = 1 - 4h + 3h^2$$

Allow κ to become asymptotically large, while by definition h must always lie within the interval $(0, 1)$. By dominant balances, either h^2 or $p(h) \equiv 1 - 4h + 5h^2 - 2h^3$ must be asymptotically small and of the order $1/\kappa$. Therefore, to leading order in large κ, two roots of dJ/dh are given by $h^{(1)} = 1/\sqrt{\kappa}$, and $h^{(2)} = 1/2$, which are candidates for the limiting value h_∞. We mainly focus attention on the first root $h^{(1)}$ since this will correspond to the limiting value of h_∞ that is accessible via the initial value problem in which the fluid is initially at rest and stably stratified. This gives the prediction $h_\infty \sim 1/\sqrt{\kappa}$. Returning to dimensional variables, the corresponding prediction for the time-limiting value of the entrained layer size h^*_∞ is

$$h^*_\infty = \sqrt{\frac{\mu V}{g\Delta\rho}} \qquad \text{as } \kappa \to \infty \tag{2.15}$$

This expression, valid to leading order for large κ, is independent of the width of the domain L. Additionally, if $L \to \infty$ with all other parameters fixed, then $\kappa \to \infty$ so that (2.15) is valid. Therefore, in the limit in which the bounded domain tends to a semi-infinite domain, the lubrication theory yields a prediction for the size of the entrained layer to replace the prediction (1.6), with the difference being a multiplicative factor of $\sqrt{2}$.

The above analysis bears some similarities to the seminal work done by Landau and Levich [14] on the coating behavior of a fluid dragged upwards by a flat plate. They study an idealized problem in which a flat, vertical plate is towed vertically out of a fluid and is viscously coated by a layer of the fluid, with a constant surface-tension present at the air-fluid interface, and they determine the limiting value of the fluid coating

thickness high in the domain. Lubrication theory is used in the upper region of the domain where the thickness of the coated layer varies slowly in the vertical direction. They find a steady-state solution to the nonlinear third order ordinary differential equation which results from the lubrication approximation with the retention of surface tension, where the limiting value of the coating thickness is left undetermined. A second asymptotic solution is found in the region far away from the plate in which the fluid-air interface is approximately a steady meniscus. In the asymptotic regime in which capillary forces dominate, the limiting value of the coating thickness can be determined by enforcing that these two asymptotic solutions match over an intermediate interval.

The analysis presented in this thesis differs from that of Landau and Levich in that here the *full time evolution* of a fluid-fluid interface is considered and it is assumed that there is not surface tension at this interface. Therefore the nonlinear third-order *ordinary* differential equation derived from lubrication theory by Landau and Levich, is replaced here by a non-linear first order *partial* differential equation. Further, the prediction for the coating thickness given by Landau and Levich is related inversely to the surface tension to the power 1/6 and this result is valid only when capillary forces are dominant, while surface tension does not enter the analysis here. A possible topic for future research is the effects of surface tension on the dynamic evolution of the flow.

Similarity Solution

It is possible to obtain a similarity solution to (2.12) under the conditions that κ is asymptotically large and $h = O(1/\sqrt{\kappa})$. Inserting the leading order term of (2.13) gives the simplified partial differential equation

$$\frac{\partial h}{\partial t} + (1 - \kappa h^2)\frac{\partial h}{\partial z} = 0 \tag{2.16}$$

We seek a similarity solution of the form $h(z,t) = t^\alpha F(t^\beta(z-t)) = t^\alpha F(\xi)$ where $\xi = t^\beta(z-t)$. Substitution into equation (2.16), gives that $2\alpha + \beta = -1$, and yields the ordinary differential equation for $F(\xi)$

$$\alpha F(\xi) + (\beta\xi - \kappa F^2(\xi))F'(\xi) = 0$$

We take $\beta = 0$ and $\alpha = -\frac{1}{2}$, so that this differential equation is separable and reduces to

$$\kappa(F^2(\xi))' + 1 = 0$$

with solution

$$F(\xi) = \sqrt{-\frac{\xi}{\kappa}}$$

This yields the similarity solution for $h(z,t)$

$$h(z,t) = t^\alpha F(\xi) = \sqrt{\frac{t-z}{\kappa t}} \qquad \text{for} \quad z \leq t \tag{2.17}$$

Taking the limit as $t \to \infty$ of (2.17) for a fixed value of z naturally gives the same limiting value of $h_\infty = \sqrt{1/\kappa}$ as was found from the characteristics method, and provides some good confirmation of this result.

2.1.2 Lubrication theory in axisymmetric geometry

As in the two dimensional case, lubrication theory is used to derive a hyperbolic partial differential for the layer thickness $h(z,t)$ in the axisymmetric geometry. The governing partial differential equation is derived by a balance of fluxes and incompressibility. Define a control region of entrained fluid which is bounded below by $z = z_1$, above by $z = z_2$, to the left by $r = a$, and to the right by $r = h(z,t)$. The volume of this region is

$$V_c \equiv \pi \int_{z_1}^{z_2} h^2(z,t) - a^2 \, dz$$

Define the vertical flux across a line as

$$F(z,t) = 2\pi \int_a^{h(z,t)} w(r,z,t)\, r \, dr$$

Balancing the flux within the control volume gives

$$\frac{dV_c}{dt} + F(z_2) - F(z_1) = 0$$

Letting $\zeta(z,t) = h^2(z,t)$ and passing to the limit as $\Delta z \to 0$ gives

$$\frac{\partial}{\partial t}\zeta(z,t) + \frac{1}{\pi}\frac{d}{dz}F(z,t) = 0 \tag{2.18}$$

Define $J(h)$ as the vertical flux, to leading order in the lubrication approximation, within the entrained layer.

$$J(h) \equiv 2\pi \int_a^h w_0(r;h)\, r\, dr \tag{2.19}$$

Let $\hat{J}(\zeta) \equiv J(h)$, so that to leading order in the lubrication approximation, we have $\hat{J}(\zeta(z,t)) = F(z,t)$. Substitution of this leading order relationship into (2.18) yields the partial differential equation for $\zeta(z,t)$

$$\frac{\partial \zeta}{\partial t} + \frac{1}{\pi}\frac{d\hat{J}}{d\zeta}\frac{\partial \zeta}{\partial z} = 0$$

Since $\zeta(z,t) = h^2(z,t)$, we have that

$$\frac{\partial \zeta}{\partial \cdot} = 2h\frac{\partial h}{\partial \cdot}$$

so that as long as $h(z,t) \neq 0$, $h(z,t)$ satisfies the partial differential equation

$$\frac{\partial h}{\partial t} + \frac{1}{\pi}\frac{d\hat{J}}{d\zeta}\frac{\partial h}{\partial z} = 0 \tag{2.20}$$

Characteristics

Since $w_0(r;h(z,t))$ is defined as the sum of three components in (1.22), define the flux $J(h)$ as the sum of three components.

$$J(h) = \kappa J_{pw}(h) + A_1(h)J_1(h) + A_2(h)J_2(h)$$

where the components are given by

$$\begin{aligned} J_{pw}(h) &= 2\pi \int_a^h w_{pw}(r;h)\, r\, dr = \frac{\pi}{8}\left(h^4 - a^4 - 2a^2h^2 \log\frac{h^2}{a^2}\right) \\ J_1(h) &= 2\pi \int_a^h \log r\, r\, dr = \frac{\pi}{2}\left(a^2 - h^2 + h^2 \log h^2 - a^2 \log a^2\right) \\ J_2(h) &= 2\pi \int_a^h (r^2 - 1)\, r\, dr = -\frac{\pi}{2}\left(2(h^2 - a^2) - (h^4 - a^4)\right) \end{aligned}$$

From this, it is possible to compute $d\hat{J}/d\zeta$

$$\begin{aligned} \frac{\mu}{\pi}\frac{d\hat{J}(\zeta)}{d\zeta} = &\left(1 - \frac{\kappa}{2}\eta^2\right)(1 + \log h) \\ &- \left(h^2 + a^2 + a^2 \log\frac{h^2}{a^2}\right) + \frac{\kappa}{2}\left(-h^4 + a^4 + (3h^4 + a^4)\log\frac{h}{a}\right) \\ &+ h^2a^2(1 - 2\log a) + a^4 \log h \\ &+ \frac{\kappa}{2}h^2a^2\left(h^2 - a^2\right) + \frac{\kappa}{2}h^2(h^4 + a^4)\log a \\ &+ \frac{\kappa}{2}h^2a^2\left(-3h^2 + a^2 + a^2 \log\frac{h^2}{a^2}\right)\log h \end{aligned} \tag{2.21}$$

where μ and η are defined by 1.24 and 1.23. The quantity $(d\hat{J}/d\zeta)/\pi$ gives the speed of characteristics for the partial differential equation (2.20). Applying the method of characteristics gives the characteristic map

$$z(t) = z_0 + \frac{1}{\pi}\frac{d\hat{J}}{d\zeta}\, t \tag{2.22}$$

The laboratory experiments are conducted in the parameter regime in which κ is typically large and the ordering $a \ll h \ll 1$ holds. With this asymptotic scaling the leading order expression for the flux is given by

$$\begin{aligned} J(h) \sim &\frac{\pi}{2 + 2\log a}\left(1 - \frac{\kappa}{4}\eta^2\right)\left(h^2(1 + \log h^2) - a^2(1 + \log a^2)\right) \\ &+ \frac{\pi\kappa}{8}\left(h^4 - a^4 - 2a^2h^2 \log\frac{h^2}{a^2}\right) \quad \text{for } \kappa \gg 1,\ a \ll h \ll 1 \end{aligned}$$

It is then possible to compute the speed of characteristics in this asymptotic regime, which is given by

$$\frac{1}{\pi}\frac{d\hat{J}(\zeta)}{d\zeta} \sim \frac{1+\log h}{1+\log a}\left(1-\frac{\kappa}{2}\eta^2\right) \qquad \text{for } \kappa \gg 1,\ a \ll h \ll 1 \tag{2.23}$$

As in two dimensions, for suitable initial conditions h_∞ is given by a root of (2.23), which implies that to leading order h_∞ satisfies

$$\kappa\left(h^2 \log\frac{h^2}{a^2} - h^2 + a^2\right) \sim 2 \qquad \text{for } \kappa \gg 1,\ a \ll h \ll 1$$

In terms of dimensional quantities, h^*_∞ satisfies

$$\frac{g\Delta\rho\, h^{*2}}{\mu V}\left(-2\log\frac{a^*}{h^*} - 1 + \frac{a^{*2}}{h^{*2}}\right) \sim 2 \qquad \text{for } \kappa \gg 1,\ a^* \ll h^* \ll L \tag{2.24}$$

Notice that this formula for the value of h^*_∞ derived from lubrication theory differs from the formula (1.19) derived from the analysis in the semi-infinite domain by a factor of two.

2.2 Full time evolution for homogeneous fluid

In the limit as $\Delta\rho \to 0$, the evolution of the fluid interface can be approximated by that of a material surface placed in a homogeneous fluid. Therefore, we compute the exact velocity field and material surface evolution for this case of homogeneous fluid in which either a wall (2D) or a fiber (axisymmetric geometric) is impulsively set into motion to a constant speed at $t = 0$. This problem is similar to Stokes' first problem - see [2] pp.189-190 and [22] pp. 194-196 - the modification being that we solve the problem in a domain bounded in the horizontal direction and enforce the vanishing net flux condition for all time. The introduction of the vanishing net flux condition introduces some interesting mathematical complexity into the problem through the pressure gradient, and it is not a trivial modification of Stokes' first problem as the resulting eigenvalue problem has an operator that is the sum of a differential operator

and a functional.

It is noted that there is the potential to augment the homogeneous Stokes solution with an additional term that accounts for the density variation. For example, in [5] the problem of a sphere descending through a sharp stratification in Stokes flow is solved using an analytical-numerical hybrid method in which the steady homogeneous Stokes solution is augmented by a density anomaly term; the density anomaly is the region of the fluid having a density value that is different than its original value. The Green's function for a single point force exterior to a sphere in free space as found by Oseen [18] is used to accomplish this in [5]. Similar methods adapted to the axisymmetric geometry of the experiment have been briefly explored using slender body theory. However, complications have been found that stem from the breakdown of slender body asymptotics in a certain limit, and thus this method has not been pursued further. However, the density anomaly perspective shows that the homogeneous solution found here, in addition to being asymptotic to the full problem for small $\Delta\rho$, is asymptotic to the full problem for short time since the volume of the density anomaly is small.

2.2.1 Two dimensional case

We solve the problem for the flow of homogeneous fluid between two flat vertical walls. The fluid is initial at rest and the wall located at $x = 0$ is impulsively set into motion at $t = 0$ to a nondimensional towing speed of 1. Exact solutions for all time are obtained under the assumptions of shear flow and vanishing flux (1.8). Under these assumptions, the Navier-Stokes system reduces to a partial differential equation for the vertical velocity $w(x, t)$

$$Re\frac{\partial w}{\partial t} = -\frac{\partial p}{\partial z} + \frac{\partial^2 w}{\partial x^2} \tag{2.25}$$

$$w(0, t) = 1 \tag{2.26}$$

$$w(1, t) = 0 \tag{2.27}$$

$$w(x, 0) = \begin{cases} 1 & \text{if} \quad x = 0 \\ 0 & \text{if} \quad 0 < x < 1 \end{cases} \tag{2.28}$$

along with the constraint of vanishing vertical flux (1.8). Due to the assumption of shear flow, the vertical pressure gradient is constant in space however does depend on time. Let

$$\frac{\partial p}{\partial z} = \beta(t)$$

Integrating the Navier-Stokes system over the interval $[0, 1]$ and using the vanishing flux condition gives the following constraint on $\beta(t)$

$$\beta(t) = w_x(1, t) - w_x(0, t) \tag{2.29}$$

Assume a separation of variables for the velocity profile

$$w(x, t) = \sum_{n=0}^{\infty} a_n \, w_n(x) \, e^{-\lambda_n t/Re}$$

From the relationship (2.29), this gives

$$\beta(t) = \sum_{n=0}^{\infty} a_n \, \beta_n \, e^{-\lambda_n t/Re}$$

where

$$\beta_n = w_n'(1) - w_n'(0) \tag{2.30}$$

With the separation of variables the partial differential equation reduces to an infinite system of ordinary differential equations given by

$$w_n''(x) + \lambda_n w_n(x) = \beta_n \tag{2.31}$$

We will view this as an inhomogeneous differential equation, with inhomogeneity β_n for the purpose of finding an exact solution. However, since β_n is dependent on $w_n(x)$ this is in actuality a homogeneous differential equation, which can be verified by checking that $w_n(x) = 0$ is a solution. The solution to the differential equation viewed

as an inhomogeneous equation is given by

$$w_n(x) = A_n \sin\sqrt{\lambda_n}x + B_n \cos\sqrt{\lambda_n}x + \frac{\beta_n}{\lambda_n}$$

which can be found by inspection since the inhomogeneity is simply a constant.

For $n > 0$, w_n must satisfy homogeneous Dirichlet boundary conditions. To satisfy $w_n(0) = 0$, we must have

$$B_n = -\frac{\beta_n}{\lambda_n}$$

If $\sin\sqrt{\lambda_n} = 0$, then to satisfy $w_n(1) = 0$, we must have $\cos\sqrt{\lambda_n} = 1$ which is equivalent to n being even. A_n is then arbitrary, and to satisfy (2.30), we must take $\beta_n = 0$. Therefore, in the case that $\sin\sqrt{\lambda_n} = 0$, the eigenfunctions are given by scalar multiples of

$$w_n(x) = \sin\sqrt{\lambda_n}x$$

These are exactly the even eigenvalues and eigenfunctions of the more familiar system

$$w_n''(x) + \lambda_n w_n(x) = 0 \tag{2.32}$$

and are given explicitly by $\lambda_n = \pi^2 n^2$ for even n.

If $\sin\sqrt{\lambda_n} \neq 0$, then to satisfy $w_n(1) = 0$ we must have

$$A_n = -\frac{\beta_n}{\lambda_n}\,\frac{1 - \cos\sqrt{\lambda_n}}{\sin\sqrt{\lambda_n}}$$

and to satisfy the constraint (2.30), we must have

$$1 - \frac{2}{\sqrt{\lambda_n}}\,\frac{1 - \cos\sqrt{\lambda_n}}{\sin\sqrt{\lambda_n}} = 0 \tag{2.33}$$

Using this constraint the coefficient A_n simplifies

$$A_n = -\frac{\beta_n}{2\sqrt{\lambda_n}}$$

Therefore, in the case that $\sin\sqrt{\lambda_n} \neq 0$, the eigenfunctions are given by scalar multiples of

$$w_n(x) = \sin\sqrt{\lambda_n}x - \frac{2}{\sqrt{\lambda_n}}\left(1 - \cos\sqrt{\lambda_n}x\right) \tag{2.34}$$

These eigenvalues and eigenfunctions are modifications of the odd eigenvalues and eigenfunctions to the corresponding problem (2.32), and are asymptotic to the eigenvalues and eigenfunctions of (2.32) as $n \to \infty$, as can be seen from the asymptotic limit of (2.33) and (2.34) for large λ_n.

To cover both the cases in which $\sin\sqrt{\lambda_n} = 0$ and $\sin\sqrt{\lambda_n} \neq 0$, we can multiply (2.33) by $\sin\sqrt{\lambda_n}$ so that the resulting function becomes zero in the case that $\sin\sqrt{\lambda_n} = 0$ and $\cos\sqrt{\lambda_n} = 1$. This yields

$$f(\lambda) = \sin\sqrt{\lambda} - \frac{2}{\sqrt{\lambda}}\left(1 - \cos\sqrt{\lambda}\right) = 0 \tag{2.35}$$

so that $f(\lambda_n) = 0$ is the eigenvalue condition for all eigenvalues, both even and odd - see figure 2.2. Since the even eigenvalues are given explicitly by $\lambda_n = \pi^2 n^2$ for n even, it is only necessary to determine the odd eigenvalues by finding roots of $f(\lambda)$. The first four odd eigenvalues are

$$\begin{aligned}
\lambda_3 &= 80.762914 \\
\lambda_5 &= 238.71806 \\
\lambda_7 &= 475.59948 \\
\lambda_9 &= 791.43124
\end{aligned}$$

For convenience, λ_1 has been omitted so that we have that the n^{th} eigenvalue of the problem (2.31) is asymptotic to the n^{th} eigenvalue of the problem (2.32) in the limit as $n \to \infty$. This omission can be understood heuristically by recognizing that the first eigenfunction of the simpler system (2.32) does not satisfy the vanishing flux condition (1.8), and neither will any slight modification of it, unlike the other odd eigenfunctions.

For $n = 0$, $w_0(x)$ must satisfy the inhomogeneous boundary conditions and the

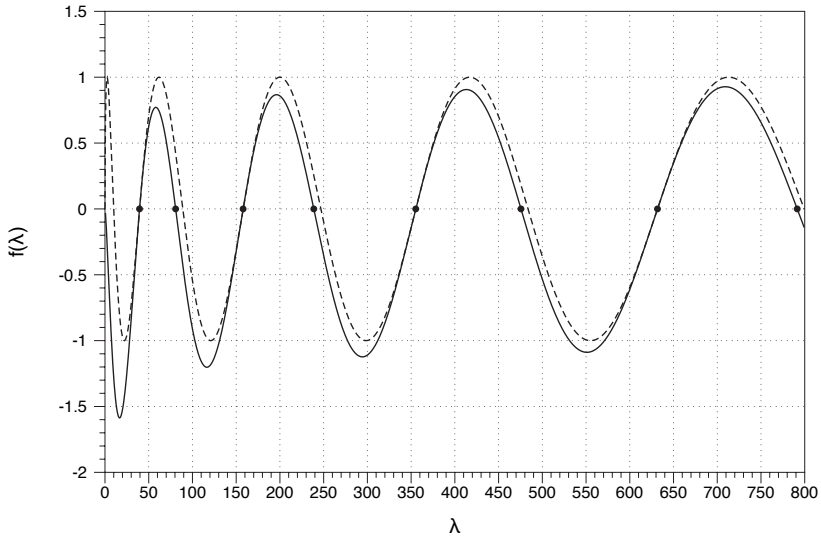

Figure 2.2: Eigenvalues of (2.31) are given as roots of $f(\lambda)$ (solid line) from equation (2.35). The dashed line shows the analogous function for the simpler related problem (2.32).

vanishing flux condition, and is therefore given by

$$w_0(x) = (1-x)(1-3x) = 1 - 4x + 3x^2 \tag{2.36}$$

with $a_0 = 1$. This is simply the steady state solution to (2.25).

Operator L_1

Let X_1 be the space of functions

$$X_1 = \left\{ u \in \mathcal{C}^2(0,1) \,\middle|\, u, u', u'' \in L^2(0,1), u(0) = u(1) = 0, \int_0^1 u(x)dx = 0 \right\}$$

Allow the standard inner product for functions $u(x), v(x) \in X_1$

$$\langle u, v \rangle = \int_0^1 u(x)\, v(x)\, dx$$

Let L_1 act on elements of X_1 as

$$L_1 u = u''(x) - u'(1) + u'(0)$$

so that the system (2.25) becomes

$$\begin{aligned} Re\frac{\partial w}{\partial t} &= L_1 \tilde{w}_t \\ w(x,0) &= \begin{cases} 1 & \text{if} \quad x = 0 \\ 0 & \text{if} \quad 0 < x < 1 \end{cases} \end{aligned}$$

for $\tilde{w}_t(x) = w(x,t)$ and $\tilde{w}_t \in X_1$.

The linear operator L_1 can be expressed as the sum of a differential operator and a functional

$$L_1 = \frac{d^2}{dx^2} + \delta'(x-1) - \delta'(x)$$

where the $\delta'(x)$ terms are functionals and these are not meant to be interpreted as variable coefficients of a differential operator. Note that if $u \in X_1$ then $L_1 u$ is also mean-zero, but may not have vanishing boundary conditions.

L_1 acts symmetricallly on functions in X_1 since if both u and v are elements of X_1 then

$$\langle u, L_1 v \rangle = \int_0^1 u(x)\, v''(x)\, dx - (v'(1) - v'(0)) \int_0^1 u(x) dx$$

Since u is mean zero the second integral vanishes, and integrating by parts we get

$$\langle u, L_1 v \rangle = \int_0^1 u(x)''\, v(x)\, dx$$

where the boundary terms vanish due to the boundary conditions on u and v. Finally, we see that this is equal to $\langle L_1 u, v \rangle$, since v is mean zero also. Therefore L_1 is a symmetric linear operator with respect to the standard inner product on X_1 and so its eigenfunctions are orthogonal with respect to this inner product.

Projection

In order to solve for the full time evolution of (2.25), the coefficients $\{a_n\}_{n=2}^{\infty}$ must be determined to satisfy the essentially zero initial condition (essentially zero since it is zero everywhere except $x = 0$). The coefficient a_0 and the function $w_0(x)$ determine the steady state solution and thus are already determined. Therefore the condition

$$\sum_{n=0}^{\infty} a_n w_n(x) = 0 \qquad x \in (0,1)$$

simplifies to the condition

$$\sum_{n=2}^{\infty} a_n w_n(x) = -w_0(x) \qquad x \in (0,1)$$

and thus to determine the coefficients $\{a_n\}_{n=2}^{\infty}$, $-w_0(x)$ must be projected onto the set of orthogonal eigenfunctions $\{w_n\}_{n=2}^{\infty}$. Projection gives

$$a_n = -\frac{1}{\|w_n\|^2} \int_0^1 w_0(x)\, w_n(x)\, dx$$

The first four coefficients are given by

$$\begin{aligned} a_2 &= -0.31830989 \\ a_3 &= -0.22254816 \\ a_4 &= -0.15915494 \\ a_5 &= -0.12944562 \end{aligned}$$

See Figure 2.3 for plots of the eigenfunctions as well as the projection of the $-w_0(x)$ onto the first four eigenfunctions.

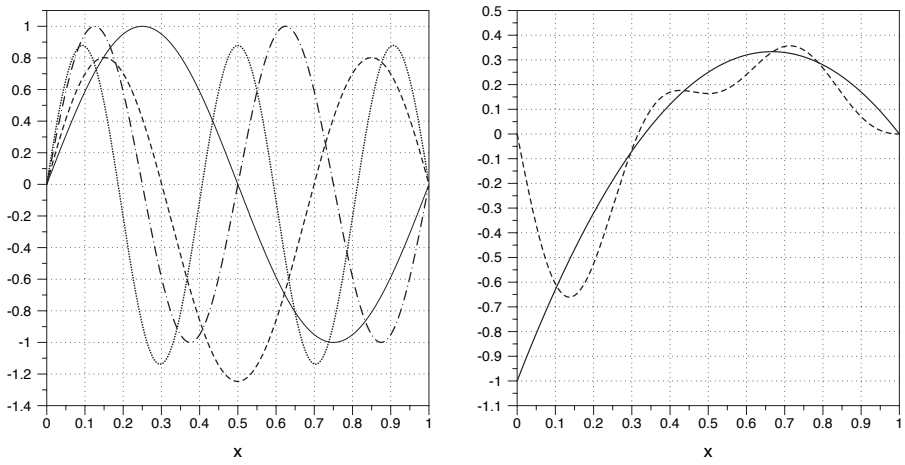

Figure 2.3: Two dimensional homogeneous density problem. Left panel: the first four eigenfunctions $w_2(x)$, $w_3(x)$, $w_4(x)$, and $w_5(x)$ given respectively by the solid line, dashed line, dot-dash line, and dotted line. Right panel: the negative of the steady state solution (solid line) given by equation (2.36), and the projection of $-w_0(x)$ onto the first four eigenfunctions (dashed line).

Inversion of L_1 and completeness of eigenfunctions

In light of the fact that the first eigenfunction of the simpler problem (2.32) does not seem to have a counterpart in the modified problem (2.31), the concern may arise that the space of eigenfunctions of (2.31) is not complete in X_1. Notice that this space of eigenfunctions is certainly not complete in $L^2(0,1)$, since all eigenfunctions are mean-zero and therefore any linear combination will be mean-zero as well, while there are certainly functions in $L^2(0,1)$ which are not mean-zero. Below, it will be shown that the space of eigenfunctions is complete in X_1 by directly inverting the operator L_1 and expressing the inverse as an integral operator for which there are completeness results.

Let X_2 be the space of square-integrable functions with mean zero

$$X_2 = \left\{ v \in L^2(0,1) \,\middle|\, \int_0^1 v(x)dx = 0 \right\}$$

For $v \in X_2$, let

$$L_2(v) = \int_0^x \int_0^y v(z)dzdy + Ax + Bx(x-1)$$

where A is chosen so that $L_2(v)$ vanishes at $x = 1$

$$A = -\int_0^1 \int_0^y v(z)dzdy$$

and B is chosen to enforce that $L_2(v)$ is mean zero

$$B = 3A + 6\int_0^1 \int_0^x \int_0^y v(z)dzdydx$$

It is straightforward to check that if $u = L_2(v)$, then $u \in X_1$ and that $L_1 u = v$.

It can be checked that $L_1 : X_1 \to X_2$ is one-to-one, for if $L_1 u = u''(x) - u'(1) + u'(0) = 0$, then u must be quadratic. However, u must satisfy homogeneous boundary conditions and have mean zero which implies that u has a third root between $x = 0$ and $x = 1$, which contradicts the fact that u is quadratic unless u is identically zero. Since $L_1 : X_1 \to X_2$ is one-to-one and $L_1 \circ L_2 : X_2 \to X_2$ is the identity, then L_1 is invertible and the inverse is L_2.

L_2 may be expressed as an integral operator

$$L_2(v) = \int_0^1 K(x, y)v(y)dy$$

with kernel

$$K(x, y) = (x - y)\chi_{[0,x)}(y) + x(y - 1) + 3xy(x - 1)(y - 1)$$

This can be shown through repeated integration by parts. The kernel $K(x, y)$ must be symmetric since the operator L_2 is the inverse of the symmetric operator L_1 and therefore must be symmetric itself. In fact, $K(x, y)$ may be expressed in a form in which the symmetric is clear

$$K(x, y) = -\min(x, y) + xy + 3xy(x - 1)(y - 1)$$

Since $K(x, y)$ is a symmetric, L^2-integrable kernel, the Hilbert-Schmidt theorem

guarantees that the set of eigenfunctions is complete in the range of L_2 - see [32] pp.110-111. Since L_1 is the inverse of L_2, they share the same space of eigenfunctions, and the above implies that this eigenfunction space is complete in both the spaces X_1 and X_2.

2.2.2 Axisymmetric case

We solve the problem for the flow between two concentric cylinders of a homogeneous fluid, initial at rest, with the inner cylinder impulsively set in motion to a non-dimensional towing speed of 1 at $t = 0$. The non-dimensional radius of the inner cylinder is a and that of the outer cylinder is 1. We can obtain exact solutions for all time under the assumptions of shear flow and vanishing flux (1.21). Under these assumptions, the axisymmetric Navier-Stokes system reduces to a partial differential equation for the vertical velocity $w(r,t)$

$$
\begin{aligned}
Re\frac{\partial w}{\partial t} &= -\frac{\partial p}{\partial z} + \frac{1}{r}\frac{\partial}{\partial r}\left(r\frac{\partial w}{\partial r}\right) && (2.37)\\
w(a,t) &= 1 && (2.38)\\
w(1,t) &= 0 && (2.39)\\
w(r,0) &= \begin{cases} 1 & \text{if} \quad r = a \\ 0 & \text{if} \quad a < r < 1 \end{cases} && (2.40)
\end{aligned}
$$

Due to the assumption of shear flow, the vertical pressure gradient is constant in space however does depend on time. Let

$$\frac{\partial p}{\partial z} = \beta(t)$$

Integrating the Navier-Stokes system over the interval $[a, 1]$ with the integration element $r\,dr$ and using the vanishing flux condition (1.21), gives the following constraint on $\beta(t)$

$$\beta(t) = \frac{2}{1-a^2}\left(w_r(1,t) - a\,w_r(a,t)\right) \tag{2.41}$$

Assume a separation of variables for the velocity profile

$$w(r,t) = \sum_{n=0}^{\infty} a_n \, w_n(r) \, e^{-\lambda_n t/Re} \tag{2.42}$$

From the relationship (2.41), this gives

$$\beta(t) = \sum_{n=0}^{\infty} a_n \, \beta_n \, e^{-\lambda_n t/Re}$$

where

$$\beta_n = \frac{2}{1-a^2} \left(w'(1) - a \, w'(a) \right) \tag{2.43}$$

With this separation of variables the partial differential equation reduces to the infinite system of ordinary differential equations

$$w_n''(r) + \frac{1}{r} w_n'(r) \lambda_n w_n(r) = \beta_n \tag{2.44}$$

For $n > 0$, w_n must satisfy homogeneous Dirichlet boundary conditions at $r = a$ and $r = 1$. As in the two-dimensional case, this will be viewed as an inhomogeneous differential equation, with inhomogeneity β_n for the purpose of finding an exact solution, even though it is actually a homogeneous differential equation through the dependence of β_n on $w_n(x)$. The solution to differential equation viewed as an inhomogeneous equation is given by

$$w_n(r) = A_n J_0\Big(\sqrt{\lambda_n} r\Big) + B_n Y_0\Big(\sqrt{\lambda_n} r\Big) + \frac{\beta_n}{\lambda_n} \tag{2.45}$$

where J_0 and Y_0 are Bessel functions of the first and second kind respectively.

Enforcing (2.43) gives

$$\frac{1-a^2}{2\sqrt{\lambda_n}} \beta_n = A_n \left(J_0'\Big(\sqrt{\lambda_n}\Big) - a \, J_0'\Big(a\sqrt{\lambda_n}\Big) \right) + B_n \left(Y_0'\Big(\sqrt{\lambda_n}\Big) - a \, Y_0'\Big(a\sqrt{\lambda_n}\Big) \right)$$

For convenience we define the quantities

$$u(\lambda) = \frac{2}{(1-a^2)\sqrt{\lambda}}\left(J_0'\left(\sqrt{\lambda}\right) - a\,J_0'\left(a\sqrt{\lambda}\right)\right)$$
$$v(\lambda) = \frac{2}{(1-a^2)\sqrt{\lambda}}\left(Y_0'\left(\sqrt{\lambda}\right) - a\,Y_0'\left(a\sqrt{\lambda}\right)\right)$$

So that

$$\frac{\beta_n}{\lambda_n} = A_n u_n + B_n v_n$$

where $u_n \equiv u(\lambda_n)$ and $v_n \equiv v(\lambda_n)$. Then the homogeneous boundary conditions become

$$w_n(a) = A_n\left(J_0\left(a\sqrt{\lambda_n}\right) + u_n\right) + B_n\left(Y_0\left(a\sqrt{\lambda_n}\right) + v_n\right) = 0 \tag{2.46}$$
$$w_n(1) = A_n\left(J_0\left(\sqrt{\lambda_n}\right) + u_n\right) + B_n\left(Y_0\left(\sqrt{\lambda_n}\right) + v_n\right) = 0 \tag{2.47}$$

Enforcing these homogeneous boundary conditions gives the condition that

$$\begin{aligned} f(\lambda) =& J_0\left(a\sqrt{\lambda}\right)Y_0\left(\sqrt{\lambda}\right) - J_0\left(\sqrt{\lambda}\right)Y_0\left(a\sqrt{\lambda}\right) \\ &+ u(\lambda)\left(Y_0\left(\sqrt{\lambda}\right) - Y_0\left(a\sqrt{\lambda}\right)\right) - v(\lambda)\left(J_0\left(\sqrt{\lambda}\right) - J_0\left(a\sqrt{\lambda}\right)\right) = 0 \end{aligned}$$

Using the Bessel function identity for Wronskians [15] p. 113

$$W(J_0(z), Y_0(z)) = \frac{2}{\pi z}$$

and the identities [15] p.100

$$J_0'(z) = -J_1(z)$$
$$Y_0'(z) = -Y_1(z)$$

this simplifies somewhat to

$$\begin{aligned} f(\lambda) =& J_0\Big(a\sqrt{\lambda}\Big)Y_0\Big(\sqrt{\lambda}\Big) - J_0\Big(\sqrt{\lambda}\Big)Y_0\Big(a\sqrt{\lambda}\Big) - \frac{8}{\pi(1-a^2)\lambda} \\ &- \frac{2}{(1-a^2)\sqrt{\lambda}}\Big(J_0\Big(a\sqrt{\lambda}\Big)Y_1\Big(\sqrt{\lambda}\Big) - J_1\Big(\sqrt{\lambda}\Big)Y_0\Big(a\sqrt{\lambda}\Big)\Big) \\ &- \frac{2\,a}{(1-a^2)\sqrt{\lambda}}\Big(J_0\Big(\sqrt{\lambda}\Big)Y_1\Big(a\sqrt{\lambda}\Big) - J_1\Big(a\sqrt{\lambda}\Big)Y_0\Big(\sqrt{\lambda}\Big)\Big) \end{aligned} \tag{2.48}$$

The advantage of (2.48) is that the asymptotic order for large λ is clear. The first four eigenvalues found as roots of (2.48) are

$$\begin{aligned} \lambda_1 &= 31.743781 \\ \lambda_2 &= 77.47376 \\ \lambda_3 &= 146.95512 \\ \lambda_4 &= 233.12874 \end{aligned}$$

As in the two dimensional case, we draw an analogy to the simpler system in which the vanishing flux condition is not enforced and $\beta \equiv 0$. This gives the system of ordinary differential equations

$$w_n''(r) + \frac{1}{r}w_n'(r)\lambda_n w_n(r) = 0 \tag{2.49}$$

The eigenvalue condition for this simplified problem is

$$J_0\Big(a\sqrt{\lambda_n}\Big)Y_0\Big(\sqrt{\lambda_n}\Big) - J_0\Big(\sqrt{\lambda_n}\Big)Y_0\Big(a\sqrt{\lambda_n}\Big) = 0 \tag{2.50}$$

As $n \to \infty$ the eigenvalues given by (2.48) are asymptotic to the eigenvalues given by (2.50) - see Figure 2.4.

We solve for the eigenfunctions by solving for A_n and B_n in (2.46) and (2.47), to

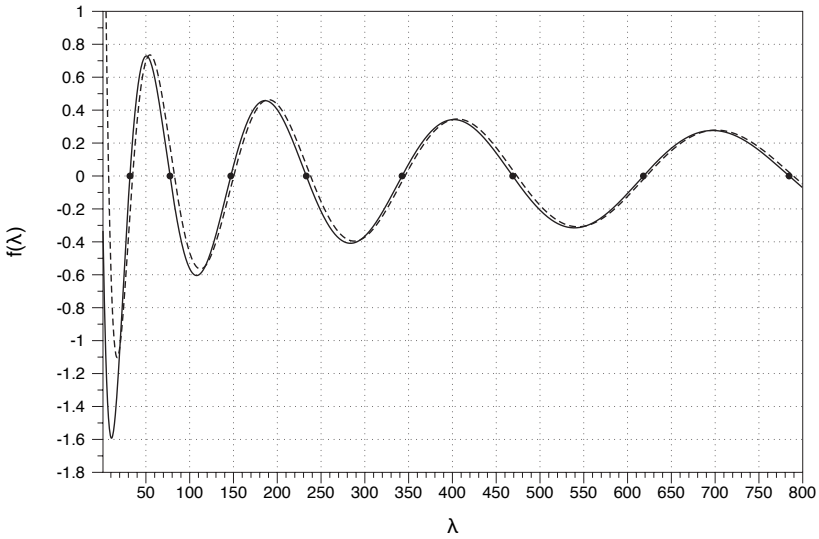

Figure 2.4: Axisymmetric homogeneous density problem with $a = 0.004$. The eigenvalues of (2.44) are given as roots of $f(\lambda)$ (solid line) from equation (2.48). The dashed line shows the related eigenvalue condition (2.50) for the simpler system (2.49).

get

$$\begin{aligned} A_n &= Y_0\Big(\sqrt{\lambda_n}\Big) + v_n \\ B_n &= -J_0\Big(\sqrt{\lambda_n}\Big) - u_n \end{aligned}$$

The eigenfunctions are then given by scalar multiples of

$$\begin{aligned} w_n(r) = &\Big(Y_0\Big(\sqrt{\lambda_n}\Big) + v_n\Big)\Big(J_0\Big(\sqrt{\lambda_n}r\Big) + u_n\Big) \\ &- \Big(J_0\Big(\sqrt{\lambda_n}\Big) + u_n\Big)\Big(Y_0\Big(\sqrt{\lambda_n}r\Big) + v_n\Big) \end{aligned} \tag{2.51}$$

For $n = 0$, $w_0(r)$ must satisfy the inhomogeneous boundary conditions and the vanishing flux condition (1.21)and is therefore given by

$$w_0(r) = A_1 \log r + A_2(r^2 - 1) \tag{2.52}$$

where

$$\begin{aligned} \mu A_1 &= 1 - 2a^2 + a^4 \\ \mu A_2 &= -1 + a^2 - 2a^2 \log a \end{aligned}$$

This is simply the steady state solution to (2.37).

Projection

Much like in the two-dimensional case, the axisymmetric operator is symmetric with respect to the inner product

$$\langle u, v \rangle = \int_a^1 u(r)v(r)\, r dr$$

and thus has an orthogonal set of eigenfunctions with respect to this inner product. As before the coefficients $\{a_n\}_{n=1}^{\infty}$ are determined be projection of $-w_0(r)$ onto the orthogonal set of eigenfunctions.

$$a_n = -\frac{1}{\|w_n\|^2} \int_0^1 w_0(r)\, w_n(r)\, r\, dr$$

The first four coefficients are given by

$$\begin{aligned} a_1 &= 0.39998275 \\ a_2 &= -0.35866133 \\ a_3 &= 0.32557042 \\ a_4 &= -0.30911197 \end{aligned}$$

Figure 2.5 shows the eigenfunctions and the projection of $-w_0(r)$ onto the first four eigenfunctions.

The time-dependent velocity profile $w(r, t)$ given by (2.42) can be used to solve for the full time evolution of a marked material surface within the fluid. Let the initial material surface be a plane oriented perpendicular to the flow placed at $z = 0$, and for

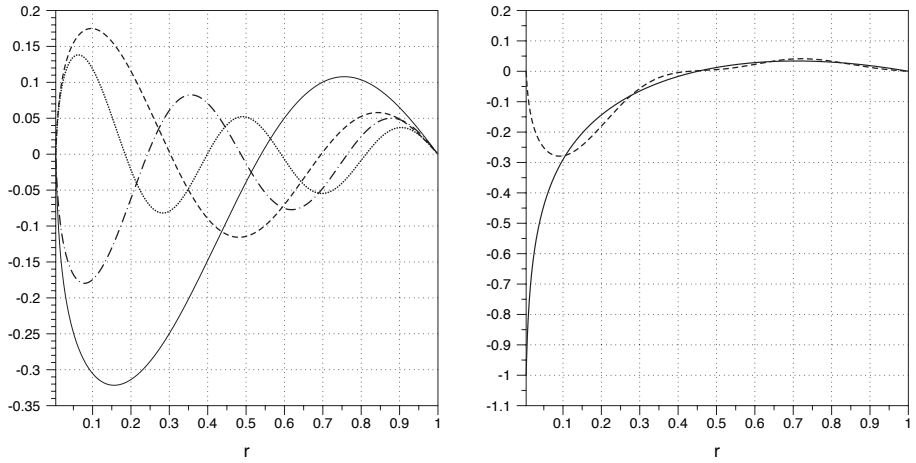

Figure 2.5: Axisymmetric homogeneous density problem with $a = 0.004$. Left panel: the first four eigenfunctions $w_1(r)$, $w_2(r)$, $w_3(r)$, and $w_4(r)$ from equation (2.51) shown respectively by the solid line, dashed line, dot-dash line, and dotted line. Right panel: the negative of the steady state solution (2.52) and the projection of $-w_0(r)$ onto the first four eigenfunctions (dashed line).

all $t \geq 0$ let the position of the material surface be described by $z = g(r,t)$. Then for all $t \geq 0$

$$g(r,t) = \int_0^t w(r,s)ds$$

and upon substitution and integration of (2.42) this becomes

$$g(r,t) = w_0(r)\,t + Re \sum_{n=1}^{\infty} \frac{a_n}{\lambda_n}\, w_n(r) \left(1 - e^{-\lambda_n t/Re}\right) \tag{2.53}$$

The transient modes of the velocity profile decay exponential as $t \to \infty$ in (2.42), with the slowest decaying mode tending to zero at roughly the rate $\exp(-31.7\,t\,/\,Re)$, and they also decay exponential in λ_n as $\lambda_n \to \infty$. However, the effect of these transient modes on the evolution of the material surface do not decay as $t \to \infty$ as is seen in (2.53), and decay at the much slower rate of $1/\lambda_n$ as $\lambda_n \to \infty$. Therefore, while the relative error made by replacing the exact expression for $w(r,t)$ by the steady solution $w_0(t)$ is on the order of $\exp(-\lambda_1\,t\,/\,Re)$ in the velocity field for large time, the relative error in the evolution of the material surface is on the order of $Re\,\lambda_1^{-1}\,t^{-1}$ for large time. This much larger error justifies the need to retain the higher order modes in the

determination of the evolution of the material surface given by equation (2.53).

Chapter 3

Stability Analysis

In this Chapter we analyze the two-parameter family of exact shear solutions, (1.10) in two-dimensions and (1.22) in the axisymmetric geometry, using linear stability analysis. We derive a fourth order ordinary differential equation with an unknown eigenvalue c that governs the stability properties of the shear solutions. A long-wave regular perturbative expansion is used in order to solve for the eigenvalue branch with largest imaginary component, corresponding to the least stable (or most unstable) mode.

Since the governing stability operator is fourth order, the eigenvalue condition is that the determinant of a four-dimensional matrix vanish. This eigenvalue condition is simplified considerably for the long-wave expansion by the choice of basis solutions in addition to the Leibniz formula which allows a determinant to be expressed in terms of determinants of sub-matrices. These combine to give the much simpler eigenvalue condition that the determinant of a two-dimensional matrix vanish, for which the eigenvalue can be found explicitly for asymptotically long waves. It is noted that if diffusivity of density is retained, as in [20], then the resulting stability operator becomes sixth order, and additionally the shear solutions (1.10) and (1.22) are not steady-state solutions.

In both the two-dimensional case and the axisymmetric case, the leading order long-wave propagation speed of disturbances from the stability analysis matches exactly the speed of characteristics found from lubrication theory. This is due to the fact that the lubrication assumption that the interface varies slowly in the vertical direction corresponds exactly to the long-wave limit of infinitesimal interfacial perturbations, and it provides good confirmation of both the lubrication analysis and the linear stability analysis since the calculations are largely independent of one another.

In both two dimensions and three dimensions the leading order term of the eigenvalue yields only a real component, corresponding to propagation of disturbances with neither damping nor amplification. Therefore, stability characteristics are determined at the first correction in the long-wave expansion.

At the first correction, the family of shear solutions (1.10) and (1.22) parameterized by κ and h exhibit bifurcations in the (κ, h) plane. For a fixed κ, the solutions are stable for small values of h and become unstable as h increases beyond a critical scale. Furthermore, this critical scale for instability is smaller than the time-limiting value of the entrained layer size h_∞ from lubrication theory, so that unstable flow configurations are attainable from the initial value problem. Remarkably, the bifurcation behavior is found to be independent of the Reynolds number as the Reynolds number enters the eigenvalue expression only as a multiplicative factor and influences the magnitude, but not the sign, of its imaginary component. This is similar to the result found by Yih [35] for a viscosity-stratified flow.

In section 3.3 we present a shooting method to determine the spectrum of the stability operator numerically. The shooting method shows excellent agreement with the long-wave asymptotic results in the appropriate limit of the wavenumber tending to zero, and provides spectral information outside of this long-wave limit. Additionally, the shooting method allows us to analyze the two-dimensional shear solutions with a smoothed density profile (1.13). We find that for an unstable two-fluid flow configuration, the introduction of a smooth density transition can slow the amplification rate of disturbance, although the flow can remain unstable. Finally, the shooting method confirms the role of the Reynolds number as only a multiplicative factor in the imaginary component of the eigenvalue, even up to a Reynolds number of 10 and a wavenumber of 10 which is well outside of the validity of the asymptotic results.

3.1 Two dimensional stability analysis

3.1.1 Stability operator

Let the background density and stream-function be given by $\rho_B(x)$ and $\psi_B(x)$ respectively. We analyze the Boussinesq approximation equations for infinitesimal perturbations of the background state. The perturbed stream-function and density profiles

are assumed to take the form

$$\begin{aligned}\psi(x) &= \psi_B(x) + \varepsilon\hat{\psi}(x)e^{ik(z-ct)} \\ \rho(x) &= \rho_B(x) + \varepsilon\hat{\rho}(x)e^{ik(z-ct)}\end{aligned}$$

We will use the streamfunction formulation of the Boussinesq approximation equations so that the pressure variable is eliminated and incompressibility is satisfied automatically

$$Re\frac{\partial}{\partial t}(\Delta\psi) - Re\frac{\partial\psi}{\partial z}\frac{\partial}{\partial x}(\Delta\psi) + Re\frac{\partial\psi}{\partial x}\frac{\partial}{\partial z}(\Delta\psi) = \Delta^2\psi - \frac{Re}{Fr^2}\frac{\partial\rho}{\partial x}$$

After linearizing around our exact solutions we obtain a system of ordinary differential equations for the perturbation streamfunction and denisty with undetermined eigenvalue c

$$(D^2-k^2)^2\hat{\psi} - i\,k\,Re\,\left((w_B-c)(D^2-k^2)\hat{\psi} - w_B''\hat{\psi}\right) - \frac{Re}{Fr^2}D\hat{\rho} = 0 \qquad (3.1)$$

$$\hat{\rho} = \frac{\rho_B'}{w_B-c}\hat{\psi} \qquad (3.2)$$

Homogeneous boundary conditions are imposed on $\hat{\psi}(x)$ and $\hat{\psi}'(x)$ at $x = 0$ and $x = 1$.

In general, the density profile is related to the velocity profile by

$$\frac{Re}{Fr^2}\rho_B'(x) = w_B'''(x)$$

Substitution of this relationship into (3.1) and (3.2), and dropping that hat notation for ψ gives the simplified stability operator

$$(D^2-k^2)^2\psi - i\,k\,Re\,\left((w_B-c)(D^2-k^2)\psi - w_B''\psi\right) - D\left(\frac{w_B'''}{w_B-c}\psi\right) = 0 \qquad (3.3)$$

Non-Boussinesq operator

We also derive the stability operator for the Navier-Stokes equations in which the Boussinesq approximation is not made, so that the inertial effects of density variations are not neglected. For the full Navier-Stokes system we do not utilize the streamfunction

formulation but instead add the perturbations directly to the momentum equations, and the pressure may be eliminated through differentiation and subtraction. The resulting stability operator is

$$(D^2-k^2)^2\psi - i\,k\,Re\,\rho_B\left((w_B-c)(D^2-k^2)\psi - w_B''\psi\right) - D\left(\frac{w_B'''}{w_B-c}\psi\right) \\ -i\,k\,Fr^2\,w_B'''\left((w_B-c)\psi' - w_B'\psi\right) = 0 \tag{3.4}$$

Here $Fr^2 = V^2/gL$ is the square of the Froude number. Without the Boussinesq approximation both the background velocity profile w_B and density profile ρ_B enter into the operator in a nontrivial fashion. If we take $\rho_B \equiv 1$ and $Fr^2 = 0$ in (3.4) we obtain the operator for the Boussinesq approximation (3.3).

3.1.2 Two-fluid system as special case of general stability operator

For the special case of a two-fluid system with velocity profile given by (1.10), we have the relationship

$$w_B'''(x) = \frac{Re}{Fr^2}\rho_B'(x) = -\kappa\delta(x-h)$$

where $\delta(x)$ is the delta-distribution. Substitution of this relationship into (3.3) gives the simplified stability equation for the case of a two-fluid system

$$(D^2-k^2)^2\psi - i\,k\,Re\,\left((w_B-c)(D^2-k^2)\psi - w_B''\psi\right) + \frac{\kappa\,\psi(h)}{w_h-c}\delta'(x-h) = 0 \tag{3.5}$$

This ordinary differential equation is an extension of the classic Orr-Somerfeld equation, with the additional $\delta'(x-h)$ term arising from the vertical density layering. Since this additional term is only supported at $x = h$, we may divide the interval $0 < x < 1$ into two subintervals $0 < x < h$ and $h < x < 1$, in which $\psi_L(x)$ and $\psi_R(x)$ must respectively satisfy the classical Orr-Somerfeld equation with matching conditions imposed at $x = h$. The Orr-Somerfeld equation to be satisfied in each interval is simply

$$(D^2-k^2)^2\psi - i\,k\,Re\,\left((w_B-c)(D^2-k^2)\psi - w_B''\psi\right) = 0 \tag{3.6}$$

The matching conditions are that $\psi_L(h) = \psi_R(h)$, $\psi'_L(h) = \psi'_R(h)$, and $\psi'''_L(h) = \psi'''_R(h)$, and the jump condition on the second derivative imposed by the presence of the $\delta'(x-h)$ term is

$$\left[D^2\psi\right] = -\frac{\kappa\psi(h)}{w_h - c} \tag{3.7}$$

where $\left[D^k\psi\right] \equiv \lim_{x\to h^+} D^k\psi(x) - \lim_{x\to h^-} D^k\psi(x)$.

For the full Navier-Stokes equations (without the Boussinesq approximation made) the stability equation for the two-fluid system becomes

$$(D^2-k^2)^2\psi - i\,k\,Re\,\rho_B\left((w_B-c)(D^2-k^2)\psi - w''_B\psi\right) + \frac{\kappa\,\psi(h)}{w_h-c}\delta'(x-h) \\ +i\,k\,\kappa\,Fr^2\,\delta(x-h)\left((w_B-c)\psi' - w'_B\psi\right) = 0$$

3.1.3 Two-fluid system dynamic interface stability derivation

Alternatively, the stability operator (3.5) can be derived directly from the two-fluid system in which we treat two homogeneous fluids with appropriate conditions at the interface of the fluids. We add a sinusoidal perturbation to the interface, positioned at $x = \xi(z,t)$ where

$$\xi(z,t) = h + \varepsilon\hat{\rho}e^{ik(z-ct)} \tag{3.8}$$

and as before allow perturbations to the velocity field through streamfunction perturbations, which is now defined in two separate domains.

$$\psi(x,z,t) = \begin{cases} \psi_L(x) + \varepsilon\hat{\psi}_L(x)e^{ik(z-ct)} & \text{if} \quad 0 \le x \le \xi(z,t) \\ \psi_R(x) + \varepsilon\hat{\psi}_R(x)e^{ik(z-ct)} & \text{if} \quad \xi(z,t) < x \le 1 \end{cases} \tag{3.9}$$

We have gained no generality by including the constant $\hat{\rho}$ in the perturbation of the density interface. The purpose of this term is simply for convenience in comparing the relative magnitude of the streamfunction perturbation to the interface perturbation and for later comparison to the previous derivation.

The kinematic condition at the fluid interface is

$$\frac{\partial\xi}{\partial t} + w(\xi,z,t)\frac{\partial\xi}{\partial z} = \hat{u}(\xi,z,t) \tag{3.10}$$

After substitution of (3.8) and (3.9), and subsequent linearization for small ε, this condition becomes

$$\hat{\rho} = -\frac{\hat{\psi}(h)}{w_h - c} \tag{3.11}$$

The streamfunction perturbations $\hat{\psi}_L(x)$ and $\hat{\psi}_R(x)$ must separately satisfy the classic Orr-Somerfeld equation (3.6), with the additional conditions of continuity of velocity and continuity of stress at the dynamic interface $x = \xi(z,t)$. We will linearize these conditions for small values of ε, and therefore we compute the Taylor expansion in ε of the quantities

$$\begin{aligned} w_B(\xi) &= w_B(h) + \varepsilon {w_B}'(h)\hat{\rho}\, e^{ik(z-ct)} + O(\varepsilon^2) \\ {w_B}'(\xi) &= {w_B}'(h) + \varepsilon {w_B}''(h)\hat{\rho}\, e^{ik(z-ct)} + O(\varepsilon^2) \end{aligned}$$

After linearization we have

$$\begin{aligned} \frac{\partial u_{1,2}}{\partial z}(\xi) &= \varepsilon\, k^2\, \hat{\psi}_{1,2}(h)\, e^{ik(z-ct)} + O(\varepsilon^2) \\ \frac{\partial u_{1,2}}{\partial x}(\xi) &= -\varepsilon\, i\, k\, \hat{\psi}'_{1,2}(h)\, e^{ik(z-ct)} + O(\varepsilon^2) \\ \frac{\partial w_{1,2}}{\partial z}(\xi) &= \varepsilon\, i\, k\, \hat{\psi}'_{1,2}(h)\, e^{ik(z-ct)} + O(\varepsilon^2) \end{aligned}$$

Most importantly we expand

$$\frac{\partial w_{1,2}}{\partial x}(\xi) = w'_B(h) + \varepsilon e^{ik(z-ct)} \left(\hat{\rho}\, w''_B(h) + \hat{\psi}''_{1,2}(h) \right) + O(\varepsilon^2)$$

Thus we need

$$\left[D^2 \hat{\psi} \right] = -\hat{\rho}\, [w''_B]$$

from the exact solution (1.10) we have that $[w''_B] = -\kappa$. Finally substitution of the relationship (3.11) gives a jump condition for the second derivative of $\hat{\psi}$ identical to that derived from the general case (3.7).

This derivation of the stability operator involving a perturbed fluid-fluid interface is perhaps a more classic derivation. However, we note that the use of the equivalent operator (3.5) which employs distributions as variable coefficients, appears to allow for

more efficient calculation in many cases.

3.1.4 Long wave asymptotic expansion

We seek to solve the eigenvalue problem (3.5) for long waves corresponding to small values of k. Since the terms kRe and k^2 enter (3.5) analytically, it is natural to seek a joint power expansion in these terms corresponding to a regular perturbation series. Let

$$\psi(x) = \psi_0(x) + kRe\,\psi_1(x) + k^2\psi_2(x) + O\left(k^2Re^2, k^3Re, k^4\right) \tag{3.12}$$

$$c = c_0 + kRe\,c_1 + k^2c_2 + O\left(k^2Re^2, k^3Re, k^4\right) \tag{3.13}$$

In the case that $k \ll Re$ and $k\,Re \ll 1$, corresponding to a fixed Reynolds - long wave limit, the first corrections to the leading order eigenfunction and eigenvalue will be ψ_1 and c_1 respectively. In the case that $Re \ll k$ and $k^2 \ll 1$, corresponding to a long wave - low(er) Reynolds limit, the first correction will be ψ_2 and c_2 respectively. Imaginary coefficients enter (3.5) in combination with the coefficient kRe and so information on the imaginary component of c, and thus stability information, will be obtained at order kRe. Therefore we are most interested in obtaining the kRe correction corresponding to long waves.

Notice that the expansions (3.12) and (3.13) are valid for any fixed Reynolds number so long as k is small enough that $kRe \ll 1$. Thus, for sufficiently long waves, some stability information will be obtained from this expansion for any fixed Reynolds number.

Note that modes corresponding to the classic Orr-Somerfeld equation, with $c = O(k\,Re)^{-1}$ to leading order, are also present and exhibit large damping proportional to $(k\,Re)^{-1}$ as $k\,Re \to 0$ as in the homogeneous problem - see [9] pp. 158-164. Since the behavior of these modes are identical to that in the homogeneous Orr-Somerfeld equation and they are always damped in the asymptotic regime under consideration, they will not be discussed any further.

In order to treat the $\delta'(x-h)$ term in (3.5), we will need to compute a series

expansion in $k\,Re$ and k^2, for coefficient of $\delta'(r-h)$

$$\begin{aligned}\frac{\kappa\,\psi(h)}{w_h-c} =& \frac{\kappa}{w_h-c_0}\left(\psi_0(h)+k\,Re\,\psi_1(h)+k^2\psi_2(h)\right)\left(1-\frac{k\,Re\,c_1+k^2c_2}{w_h-c_0}\right)^{-1}\\ &+O\left(k^2Re^2,k^3Re,k^4\right)\end{aligned}$$

For we convenience let

$$\gamma=\frac{\kappa}{w_h-c_0}$$

Performing a geometric expansion and simplifying gives

$$\begin{aligned}\frac{\kappa\,\psi(h)}{w_h-c} =& \gamma\psi_0(h)+\gamma\,k\,Re\,\left(\psi_1(h)+\frac{\gamma\psi_0(h)}{\kappa}c_1\right)\\ &+\gamma\,k^2\left(\psi_2(h)+\frac{\gamma\psi_0(h)}{\kappa}c_2\right)+O\left(k^2Re^2,k^3Re,k^4\right)\end{aligned}$$

3.1.5 Leading order

Balancing the leading order terms in (3.5) with respect to the long wave expansion (3.12) and (3.13) gives the homogeneous ordinary differential equation for $\psi_0(x)$

$$D^4\psi_0(x)+\gamma\psi_0(h)\delta'(x-h)=0$$

with homogeneous boundary conditions

$$\psi_0(0)=\psi_0'(0)=\psi_0(1)=\psi_0'(1)=0$$

The solution to this equation can be written as

$$\psi_0(x)=b_1^0f_1(x))+b_2^0f_2(x)+b_3^0f_3(x)+b_4^0f_4(x)+\gamma\psi_0(h)\psi_{pw}(x)$$

Each $f_k(x)$ has a vanishing fourth derivative

$$\begin{aligned} f_1(x) &= (x-1)^2 \\ f_2(x) &= x(x-1)^2 \\ f_3(x) &= x^2 \\ f_4(x) &= x^2(x-1) \end{aligned}$$

The piecewise function $\psi_{pw}(x)$ is given by

$$\psi_{pw}(x) = \begin{cases} \frac{1}{2}(x-h)^2 & \text{if} \quad 0 \le x \le h \\ 0 & \text{if} \quad h < x \le 1 \end{cases}$$

and satisfies the jump conditions imposed by a $\delta'(x-h)$ term

$$D^4\psi_{pw} + \delta'(x-h) = 0$$

These functions have been chosen to simplify the boundary conditions as much as possible. In order to treat the boundary conditions we form the following matrices

$$\mathbf{M_1} = \begin{pmatrix} f_1(0) & f_2(0) & f_3(0) & f_4(0) \\ f_1'(0) & f_2'(0) & f_3'(0) & f_3'(0) \\ f_1(1) & f_2(1) & f_3(1) & f_4(1) \\ f_1'(1) & f_2'(1) & f_3'(1) & f_4'(1) \end{pmatrix} = \begin{pmatrix} 1 & 0 & 0 & 0 \\ -2 & 1 & 0 & 0 \\ 0 & 0 & 1 & 0 \\ 0 & 0 & 2 & 1 \end{pmatrix}$$

$$\begin{aligned} \mathbf{M_2} &= \begin{pmatrix} \psi_{pw}(0) \\ \psi_{pw}'(0) \\ 0 \\ 0 \end{pmatrix} \cdot \begin{pmatrix} f_1(h) & f_2(h) & f_3(h) & f_4(h) \end{pmatrix} \\ &= \begin{pmatrix} \frac{1}{2}h^2 \\ -h \\ 0 \\ 0 \end{pmatrix} \cdot \begin{pmatrix} (1-h)^2 & h(1-h)^2 & h^2 & -h^2(1-h) \end{pmatrix} \end{aligned}$$

We let

$$\mathbf{M} = \mathbf{M_1} + \gamma \mathbf{M_2}$$

In order to satisfy the homogeneous boundary conditions, the matrix problem must be satisfied

$$\mathbf{M} \cdot \mathbf{b_0} = \mathbf{0}$$

where $\mathbf{b_0} = (b_1^0, b_2^0, b_3^0, b_4^0)$. We can use the Leibniz rule to choose γ (and therefore c_0) so that the $\det \mathbf{M} = 0$. In block form,

$$\mathbf{M} = \begin{pmatrix} \mathbf{A} & \mathbf{B} \\ \mathbf{C} & \mathbf{D} \end{pmatrix}$$

The Leibniz formula gives $\det \mathbf{M} = \det \mathbf{D} \det(\mathbf{A} - \mathbf{B}\mathbf{D}^{-1}\mathbf{C})$. Since $\det \mathbf{D} = 1$ and $\mathbf{C}$ is the zero matrix, for $\det \mathbf{M} = 0$ we must have that $\det \mathbf{A} = 0$. $\mathbf{A}$ is given by

$$\mathbf{A} = \begin{pmatrix} 1 + \frac{1}{2}\gamma h^2(h-1)^2 & \frac{1}{2}\gamma h^3(h-1)^2 \\ -2 - \gamma h(h-1)^2 & 1 - \gamma h^2(h-1)^2 \end{pmatrix} \tag{3.14}$$

This results in the condition on γ

$$\gamma = \frac{2}{h^2(1-2h)(1-h)^2}$$

Solving for c_0 gives

$$c_0 = w_h - \frac{\kappa}{\gamma} = w_h - \frac{1}{2}\kappa h^2(1-2h)(1-h)^2$$

From the exact solution (1.10), we get

$$w_h = (1-h)(1-3h) - \frac{1}{2}\kappa h^2(1-2h)(1-h)^2$$

Upon substitution, this gives a compact expression for the leading order term of the eigenvalue

$$c_0 = (1 - \kappa h^2)(1 - 4h) + h^2(3 - 5\kappa h^2) + 2\kappa h^5 \tag{3.15}$$

which has been ordered to respect the asymptotic regime of $\kappa \gg 1$ and $h = O(1/\sqrt{\kappa})$. This expression matches the formula for the characteristics speeds (2.13) exactly since the propagation of long-wave disturbances corresponds exactly to the propagation of characteristics under the lubrication approximation. Figure 3.2 shows the zero-curves of c_0 which corresponds to the curves along which disturbances propagate at zero speed. Additional, since c_0 corresponds exactly to the characteristics speeds given by lubrication theory, the lower zero-curve shown in Figure 3.2 can also be interpreted as h_∞ as a function of κ. Note that the zero-curve of c_0 is independent of the Reynolds number.

At the next order, we will need to solve for the leading order eigenfunction $\psi_0(x)$. Solving for the coefficients gives the linear space of

$$\mathbf{b_0} = (h^2,\, -2h(1-h),\, 0,\, 0)$$

and so the leading order eigenfunction is given by scalar multiples of

$$\psi_0(x) = \begin{cases} h^2(x-1)^2 - 2h(1-h)x(x-1)^2 - (x-h)^2 & \text{if} \quad 0 \le x \le h \\ h^2(x-1)^2 - 2h(1-h)x(x-1)^2 & \text{if} \quad h < x \le 1 \end{cases} \tag{3.16}$$

3.1.6 First correction

We may substitute the γ found in the leading order calculation in order to obtain the simplification

$$\frac{\gamma\psi_0(h)}{\kappa} = -\frac{2}{\kappa}$$

At order $k\,Re$, $\psi_1(x)$ solves the inhomogeneous ordinary differential equation

$$D^4\psi_1(x) + \gamma\left(\psi_1(h) - \frac{2}{\kappa}c_1\right)\delta'(x-h) = i(v - c_0)D^2\psi_0 - iv''\psi_0 \tag{3.17}$$

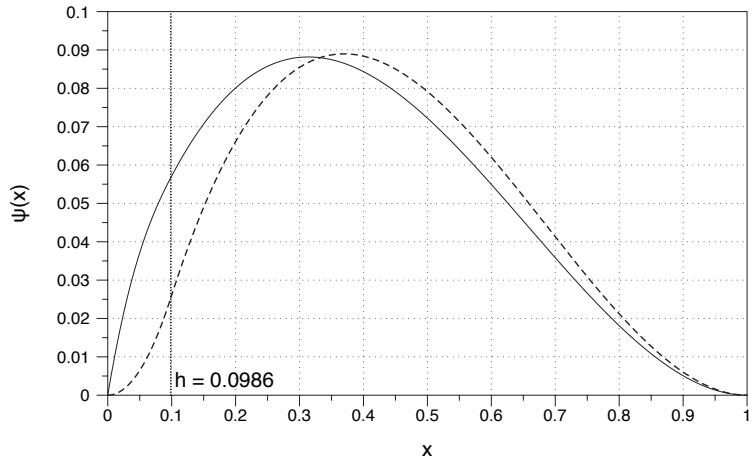

Figure 3.1: The solid line shows the streamfunction for the background shear solution for the two-dimensional two-fluid system, equation (1.11), with $\kappa = 100$ and $h = h_\infty = 0.0986$. The dashed line shows the leading order eigenfunction $\psi_0(x)$ given by stability analysis: equation (3.16) rescaled by the factor -4 for the sake of comparison. The vertical dotted line shows the position of the density discontinuity h.

with homogeneous boundary conditions

$$\psi_1(0) = \psi_1'(0) = \psi_1(1) = \psi_1'(1) = 0$$

The solution can be written as

$$\begin{aligned}\psi_1(x) =& b_1^1 f_1(x) + b_2^1 f_2(x) + b_3^1 f_3(x) + b_4^1 f_4(x) \\ &+ \gamma \left(\psi_1(h) - \frac{2}{\kappa} c_1 \right) \psi_{pw}(x) + \psi_p(x)\end{aligned}$$

$\psi_p(x)$ is a piecewise function

$$\psi_p(x) = \begin{cases} p_L(x) & 0 \le x \le h \\ p_R(x) & h < x \le 1 \end{cases}$$

where $p_L(x)$ and $p_R(x)$ are particular solutions to the inhomogeneous differential equation with the initial conditions

$$p_{L,R}(h) = p'_{L,R}(h) = p''_{L,R}(h) = p'''_{L,R}(h) = 0 \tag{3.18}$$

To satisfy the homogeneous boundary conditions we must have that

$$\begin{aligned}
b_1^1 f_1(0) + b_2^1 f_2(0) + \gamma\psi_1(h)\psi_{pw}(0) &= p_L(0) + \frac{2}{\kappa}c_1\psi_{pw}(0) \\
b_1^1 f_1'(0) + b_2^1 f_2'(0) + \gamma\psi_1(h)\psi'_{pw}(0) &= -p'_L(0) + \frac{2}{\kappa}c_1\psi'_{pw}(0) \\
b_3^1 f_3(1) + b_4^1 f_4(1) &= -p_R(1) \\
b_3^1 f_3'(1) + b_4^1 f_4'(1) &= -p'_R(1)
\end{aligned}$$

The last two equations allow us to solve for b_3^1 and b_4^1 directly. Let

$$\mathbf{D} = \begin{pmatrix} f_3(1) & f_4(1) \\ f_3'(1) & f_4'(1) \end{pmatrix} = \begin{pmatrix} 1 & 0 \\ 2 & 1 \end{pmatrix}$$

Then b_3^1 and b_4^1 are given by

$$\begin{pmatrix} b_3^1 \\ b_4^1 \end{pmatrix} = -\mathbf{D^{-1}} \begin{pmatrix} p_R(1) \\ p'_R(1) \end{pmatrix}$$

For convenience let

$$\zeta = b_3^1 f_3(h) + b_4^1 f_4(h)$$

Then b_1^1 and b_2^1 are determined by

$$\mathbf{A}\begin{pmatrix} b_1^1 \\ b_2^1 \end{pmatrix} = -\begin{pmatrix} p_L(0) \\ p'_L(0) \end{pmatrix} + \gamma\left(\zeta + \frac{2\,c_1}{\kappa}\right)\begin{pmatrix} \psi_{pw}(0) \\ \psi'_{pw}(0) \end{pmatrix} \equiv \mathbf{y}$$

where $\mathbf{A}$ is defined by equation (3.14). Upon substitution of γ, $\mathbf{A}$ simplifies to

$$\mathbf{A} = \frac{1}{h(1-2h)} \begin{pmatrix} 2h(1-h) & h^2 \\ -2(1+h-2h^2) & -h(1+2h) \end{pmatrix}$$

For the matrix problem to have a solution, it is required by the Fredholm alternative that $\mathbf{y}$ is orthogonal to the null-space of the adjoint of $\mathbf{A}$, which is given by the linear space of

$$\mathbf{v} = \begin{pmatrix} v_1 \\ v_2 \end{pmatrix} = \begin{pmatrix} 1+2h \\ h \end{pmatrix}$$

For convenience, let

$$\mathbf{y} = \begin{pmatrix} y_1 \\ y_2 \end{pmatrix} = \begin{pmatrix} \alpha_1 \\ \alpha_2 \end{pmatrix} + c_1 \begin{pmatrix} \beta_1 \\ \beta_2 \end{pmatrix}$$

Then from the definition of $\mathbf{y}$, α_1 and α_2 are given by

$$\begin{pmatrix} \alpha_1 \\ \alpha_2 \end{pmatrix} = -\begin{pmatrix} p_L(0) \\ p_L'(0) \end{pmatrix} + \gamma\zeta \begin{pmatrix} \psi_{pw}(0) \\ \psi_{pw}'(0) \end{pmatrix}$$

and β_1 and β_2 are given by

$$\begin{pmatrix} \beta_1 \\ \beta_2 \end{pmatrix} = \frac{2\,\gamma}{\kappa} \begin{pmatrix} \psi_{pw}(0) \\ \psi_{pw}'(0) \end{pmatrix}$$

Enforcing that $\mathbf{y}$ is orthogonal to $\mathbf{v}$, gives

$$c_1 = -\frac{\alpha_1 v_1 + \alpha_2 v_2}{\beta_1 v_1 + \beta_2 v_2} \tag{3.19}$$

In order to obtain the values for $p_L(0), p_L'(0), p_R(1), p_R'(1)$ we solve the fourth order inhomogeneous differential equation (3.17) with the specified initial conditions (3.18) using Mathematica. See Appendix C for the explicit values and Appendix E for the generating Mathematica script. Then we substitute the obtained values into (3.19).

The resulting exact expression for c_1 is

$$c_1 = -\frac{i}{840}(1-h)^3\kappa h^3\Big\{20 - 38\kappa h^2 + h(-153 + 222\kappa h^2) + h^2(339 - 476\kappa h^2) + h^3(-198 + 438\kappa h^2) - 146\kappa h^6\Big\} \tag{3.20}$$

This expressions has been ordered to respect the asymptotic scaling $\kappa \gg 1$ and $h = O(1/\sqrt{\kappa})$.

3.1.7 Two-dimensional stability discussion

Since the expression for c_1 is imaginary this indicates damping or amplification of disturbances depending on the sign of c_1. Figure 3.2 shows the zero-curves of c_1 which corresponds to curves of long-wave neutral stability, with regions of stability indicated by shading. Since the stability transition occurs for long waves, the zero-curve of formula (3.20) gives the exact neutral stability curve with no approximation made. The neutral stability curve is independent of the Reynolds number, as the Reynolds number only affects the magnitude of damping or amplification.

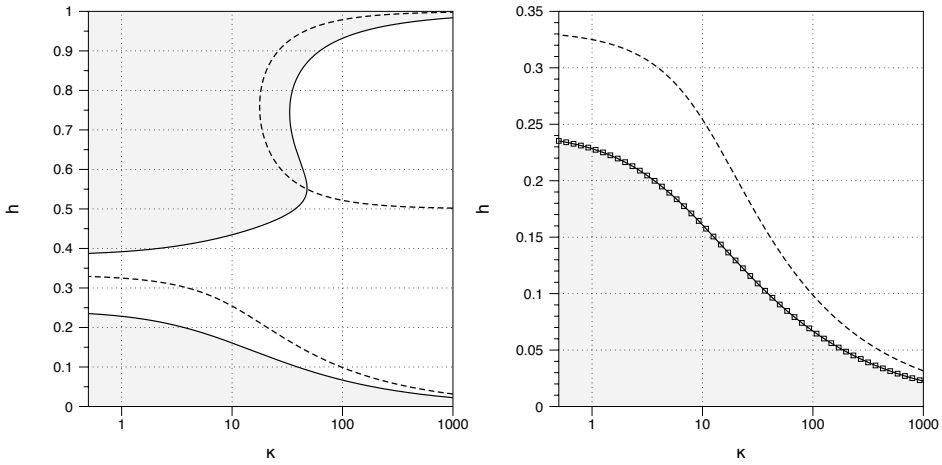

Figure 3.2: Two-dimensional bifurcation diagram. Left panel: zero-curves of c_0 (dashed line) from equation (3.15) and c_1 (solid line) from equation (3.20), with shading indicating regions of stability. Right panel: a blowup of the left panel for small h along with the neutral stability curve found by the shooting method (boxes), with the fixed values of $Re = 1$ and $k = 0.01$, showing nearly exact agreement with the zero-curve of c_1.

Consider the limit to the semi-infinite domain with $L \to \infty$ and all other dimensional parameters fixed. This implies that $\kappa \to \infty$ and $h \to 0$, and so the leading order correction for c_1 is simply

$$c_1 \sim -\frac{i\,\kappa h^3}{420}\left(10 - 19\kappa h^2\right) \tag{3.21}$$

In this limit to the semi-infinite domain, lubrication theory gives the limiting value for the size of the entrained layer as $h_\infty \sim 1/\sqrt{\kappa}$. Substitution of this limiting value of h into the formula for c_1 gives

$$c_1 \sim \frac{3\,i}{140\sqrt{\kappa}}$$

Since this is a positive imaginary component, this indicates that in the limit to the semi-infinite domain the entrained layer will grow to a size that is unstable. However, the growth rate of disturbances tends to zero in this limit since $\kappa \to \infty$.

3.1.8 Comparison to previous work

The stability problem (3.3) can be understood in the context of previous work. Benjamin [3] and Yih [34] have studied the stability of fluid flowing down an inclined plane with a free surface in two dimensions, and Kao [12, 13] has extended this by considering the effects of a stratified two-fluid system flowing down an inclined plane, although he did not consider arbitrary density profiles. In addition Yih has studied the stability of flow with viscous stratification [35] in two dimensions, which although is quite different physically from the present study bears many mathematical similarities to it.

Finally, Sangster [23] studied the problem of the flow of a two-fluid system down an inclined surface with a rigid lid (no free-surface) in two dimensions, with and without surface tension at the fluid-fluid interface. Therefore, the present study corresponds to the problem studied by Sangster for an inclination of 90°, zero surface-tension, and the addition that one of the boundaries is towed at a fixed rate. Sangster did not investigate the time-evolution of the thickness of one stream relative to the other, but only considered the stability analysis for a fixed ratio of the bottom fluid thickness to top fluid thickness. Through the use of a long-wave expansion (as used here) in addition to a truncated Frobenius series for the eigenfunction (not used here), Sangster obtained approximations to the real and imaginary components of the eigenvalue c. The analysis

of Sangster was limited to the condition that the thickness of the lower stratum be greater than that of the upper, which is exactly the opposite of the situation of primary attention in the current investigation. In this thesis, primary attention is given to the situation in which the size of the entrained layer (corresponding to the lower-stratum in Sangster's study) is small, although much of the analysis presented here does not require this condition. Finally, Sangster's calculations are rather laborious and the resulting eigenvalue expressions are not shown to simplify as do the calculations presented here, which result in the comparatively compact expressions (3.15) and (3.20). As will be seen in the axisymmetric problem, the corresponding expressions do not simplify to such compact expressions.

In the investigations of Yih [34] and Kao [12, 13], there were found "hidden neutral modes" which are analogous to the modes found here. These modes are termed hidden since they arise from the misalignment of isopycnals with gravity in [3, 34, 12, 13], and the viscous stratification in [35], and they vanish if these physical conditions are not present, for instance in homogeneous flows. Further the modes are neutral to leading order for long waves. Thus the modes found in the present study lie under this classification of hidden neutral modes.

In order to understand the connections to these previous investigations, we consider a two-dimensional stratified fluid flow bounded by two walls of infinite extent which enclose a channel (no free surface present) that is inclined with respect to gravity by an angle θ. One wall of the channel is towed at speed U_0 which may be zero, and the density profile is arbitrary. See figure (3.3) for a diagram.

We let $\mathbf{x} = (x_1, x_2)$ be the horizontal and vertical coordinates with respect to the channel walls and let $\mathbf{u} = (u_1, u_2)$ be the corresponding velocities. The nondimensional Boussinesq approximation equations are given by

$$\begin{aligned} Re\frac{D}{Dt}\mathbf{u} &= -\nabla p + \Delta\mathbf{u} + \frac{Re}{Fr^2}\,\rho\,(\sin\theta, -\cos\theta) \\ \nabla\cdot\mathbf{u} &= 0 \\ \frac{D}{Dt}\rho &= 0, \end{aligned}$$

We allow for an arbitrary density profile varying only in the vertical direction $\rho_B(x_2)$, and a shear velocity profile $u_1 = U(x_2)$ as our background solution. The density and

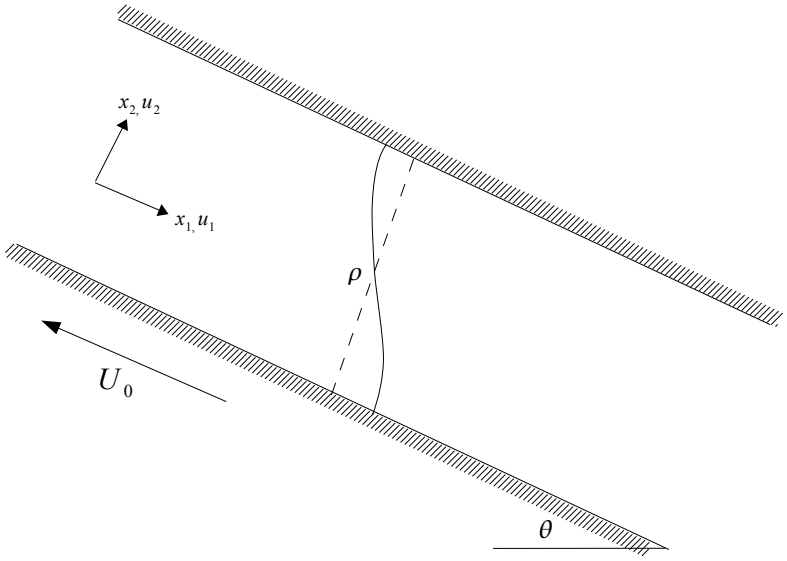

Figure 3.3: Diagram of stratified flow through a channel inclined with respect to gravity.

velocity are related by

$$U''(x_2) + \frac{Re}{Fr^2} \sin\theta \ \rho_B(x_2) + \beta = 0 \tag{3.22}$$

where as before β is a constant arising for the horizontal pressure gradient.

A streamfunction ψ exists with relation to the velocities

$$\begin{aligned} u_1 &= -\frac{\partial \psi}{\partial x_2} \\ u_2 &= \frac{\partial \psi}{\partial x_1} \end{aligned}$$

The streamfunction formulation of the Boussinesq approximation is

$$Re\frac{\partial}{\partial t}(\Delta\psi) - Re\frac{\partial\psi}{\partial x_2}\frac{\partial}{\partial x_1}(\Delta\psi) + Re\frac{\partial\psi}{\partial x_1}\frac{\partial}{\partial x_2}(\Delta\psi) = \Delta^2\psi - \frac{Re}{Fr^2}\left(\cos\theta\,\frac{\partial\rho}{\partial x_1} + \sin\theta\,\frac{\partial\rho}{\partial x_2}\right)$$

We allow for perturbation around the background solutions

$$\begin{aligned}\psi(x) &= \psi_B(x) + \varepsilon\hat{\psi}(x)e^{ik(z-ct)} \\ \rho(x) &= \rho_B(x) + \varepsilon\hat{\rho}(x)e^{ik(z-ct)}\end{aligned}$$

from which we derive the stability equation for streamfunction and density perturbations

$$\begin{aligned}(D^2-k^2)^2\psi - i\,k\,Re\,\left((U_B-c)(D^2-k^2)\psi - U_B''\psi\right) \\ - \frac{Re}{Fr^2}\left(ik\cos\theta\;\hat{\rho} + \sin\theta\;D\hat{\rho}\right) = 0 \\ \hat{\rho} = -\frac{\rho_B'}{U_B-c}\hat{\psi}\end{aligned}$$

where $D = d/dx_2$. Substitution of $\hat{\rho}$ gives

$$\begin{aligned}(D^2-k^2)^2\psi - i\,k\,Re\,\left((U_B-c)(D^2-k^2)\psi - U_B''\psi\right) \\ + ik\cos\theta\,\frac{Re}{Fr^2}\frac{\rho_B'}{U_B-c}\psi + \sin\theta\,\frac{Re}{Fr^2}D\left(\frac{\rho_B'}{U_B-c}\psi\right) = 0\end{aligned} \tag{3.23}$$

To the knowledge of the author, this stability operator for arbitrary background density profiles has not been previously documented. The previous investigation [3, 34, 12, 13, 35] have focused on the special case of a two-fluid system and thus the effects of the terms involving ρ_B in (3.23) entered analysis in the boundary conditions at the fluid-fluid interface only.

We now give an understanding of each component of the stability operator (3.23) in light of previous work and the present study. The top line of the operator is simply the classic Orr-Somerfeld equation for homogeneous fluid flow and does not give rise to neutral modes at leading order in the long-wave expansion. Indeed all modes are damped for sufficiently long waves or low Reynolds for the Orr-Somerfeld equation.

The term multiplying $\cos\theta$ arises from the horizontal component of density layering, and can be understood as part of the Taylor-Goldstein equation for the inviscid limit. Indeed the term ρ_B'/Fr^2 is the local Richardson number for the inviscid Boussinesq approximation, and in the case of $\theta = 0$ and $Re \to \infty$ we obtain the Taylor-Goldstein

equation exactly. Therefore, we will refer to this term multiplying $\cos\theta$ as the Taylor-Goldstein term. Notice that the wavenumber k multiplies the Taylor-Goldstein term and so it does not enter at the leading order of the long-wave expansion and therefore cannot give rise to leading order neutral modes. Therefore, for example in the case of $\theta = 0$ all modes will be damped for sufficiently long waves.

The term multiplying $\sin\theta$ arises from the vertical component of the density layering and we will refer to it as the vertical density layering term. Since this term is not multiplied by the wavenumber, it enters the leading order equation for the long-wave expansion, and further since the eigenvalue c is present in this term, it allows for $c = O(1)$ to leading order in this expansion. Thus this term is necessary in (3.23) for the presence of hidden neutral modes and it is the presence of this term in the stability operator that is the focus of the current study.

For further simplification we can substitute the relationship between the background density and velocity profiles

$$\sin\theta \frac{Re}{Fr^2}\rho_B'(x_2) = -U_B'''(x_2)$$

into (3.23) to obtain a stability operator in which we have eliminated ρ_B

$$\begin{aligned}(D^2-k^2)^2\psi - i\,k\,Re\,\left((U_B-c)(D^2-k^2)\psi - U_B''\psi\right)\\ - ik\cot\theta\,\frac{U_B'''}{U_B-c}\psi - D\left(\frac{U_B'''}{U_B-c}\psi\right) = 0\end{aligned} \tag{3.24}$$

The previous investigations [3, 34, 12, 13] have only studied the effects of the vertical density layering term in conjunction with the Taylor-Goldstein term, and once again these terms only entered in the boundary conditions at the fluid-fluid interface. In the Orr-Somerfeld equation the first power of k only enters in product with Re, while in the Taylor-Goldstein term k is not in product with Re. Therefore, in the long-wave expansion of c, the first correction will be a function of Re if the Taylor-Goldstein term is present and therefore there is the potential for a stability transition to occur as the Reynolds number is varied, as has been seen in [3, 34, 12, 13]. In the current study however, the vertical density layering term has been isolated so that there is no Taylor-Goldstein term present in the stability operator. In this case, the first power

of k only enters the operator in product with Re and so the first correction to c has trivial dependence on Re as it is only a scaling factor in the magnitude of the first correction, as seen in (3.12), (3.13), and (3.20). Therefore, the flow configuration under current investigation in which the density layering is completely vertical has the interesting feature that *its stability or instability to long waves is independent of the Reynolds number, and only depends on the density profile.* Of course the magnitude of the growth or decay rates of disturbances does depend on the Reynolds number. This interesting feature was also found by Yih [35] in the stability analysis of a flow with viscous stratification.

We point out a few notes regarding (3.24). First, the simplification (3.24) is not valid for $\theta = 0$ since in this case we must have $U_B''' \equiv 0$. Next, In the case that $\theta = \pi/2$ so that the channel is oriented vertically, we obtain the stability operator (3.3). Technically, for this comparison we would need to make the substitutions $x_2 \to x, x_1 \to -z, U_B \to -w_B, k \to -k, c \to -c$, since the z-direction is opposite of the x_1-direction for $\theta = \pi/2$. However, by two fortuitous sign cancellations the substitution may be made naively with the correct stability operator obtained.

Finally, if $c = U_B$ somewhere in the flow then the stability operator (3.23) is singular due to both the Taylor-Goldstein term and the vertical density layering term, and further the vertical density layering term promotes the degree of the singularity. In the generic case in which $U_B'(x_2) \neq 0$ at the point that $c = U_B$, then the singularity is promoted by the vertical density layering term from first order to second order, and therefore the singularity remains regular. However in the inviscid limit of (3.23), the Taylor-Goldstein equation has only a regular singular point while the vertical density layering term creates an irregular singular point. It should be noted however that viscosity is necessary for the existence of the background solution (3.22) if $\theta \neq 0$

3.2 Axisymmetric stability analysis

We perform linear stability analysis on the family of exact shear solutions given by (1.22) and (1.25) by adding perturbations to the axisymmetric streamfunction and

the density field

$$\begin{aligned}\psi(r) &= \psi_B(r) + \varepsilon\hat{\psi}(r)e^{ik(z-ct)} \\ \rho(r) &= \rho_B(r) + \varepsilon\hat{\rho}(r)e^{ik(z-ct)}\end{aligned}$$

We introduce the operator $\mathcal{L}$ in order to treat differentiation in cylindrical coordinates

$$\mathcal{L}f(r) \equiv r\left(\frac{f'(r)}{r}\right)' = f''(r) - \frac{1}{r}f'(r)$$

and the square of this operator is given by

$$\mathcal{L}^2 f(r) = f''''(r) - \frac{2}{r}f'''(r) + \frac{3}{r^2}f''(r) - \frac{3}{r^3}f'(r)$$

After linearizing the Boussinesq approximation equations around our exact solutions and eliminating the pressure variable, we obtain a system of ordinary differential equations for the perturbation streamfunction and denisty with undetermined eigenvalue c

$$(\mathcal{L} - k^2)^2\hat{\psi} - i\,k\,Re\,\left((w_B - c)(\mathcal{L} - k^2)\hat{\psi} - (\mathcal{L}w_B)\hat{\psi}\right) - \frac{Re}{Fr^2}rD\hat{\rho} = 0 \tag{3.25}$$

$$\hat{\rho} = \frac{1}{r}\frac{\rho_B'}{w_B - c}\hat{\psi} \tag{3.26}$$

with homogeneous boundary conditions imposed on $\hat{\psi}(r)$ and $\hat{\psi}'(r)$ at $r = a$ and $r = 1$. $w_B(r)$ and $\rho_B(r)$ denote the exact solutions for the vertical velocity and density field respectively.

For the case of a two-fluid system, the density profile $\rho_B(r)$ is a step function and we have

$$\frac{Re}{Fr^2}\rho_B'(r) = -\kappa\delta(r - h)$$

and therefore the relationship between the perturbation density and perturbation streamfunction becomes

$$-\frac{Re}{Fr^2}\hat{\rho}(r) = \frac{\kappa\,\hat{\psi}(h)}{h(w_h - c)}\delta(r - h)$$

We substitute this relation into (3.25) and drop the hat notation for the perturbation streamfunction, to obtain the simplified stability equation for the case of a two-fluid system

$$\begin{aligned}(\mathcal{L}-k^2)^2\psi - i\,k\,Re\,\left((w_B-c)(\mathcal{L}-k^2)\psi-(\mathcal{L}w_B)\psi\right)\\ +\frac{\kappa\psi(h)}{h(w_h-c)}r\delta'(r-h)=0\end{aligned} \tag{3.27}$$

This ordinary differential equation is an extension of the axisymmetric Orr-Somerfeld equation with the additional $\delta'(r-h)$ term. Since this additional term is only supported at $r=h$, we can view this as simply the axisymmetric Orr-Somerfeld equation in two domains $a<r<h$ and $h<r<1$ with appropriate matching conditions. The axisymmetric Orr-Somerfeld equation is given by

$$(\mathcal{L}-k^2)^2\psi - i\,k\,Re\,\left((w_B-c)(\mathcal{L}-k^2)\psi-(\mathcal{L}w_B)\psi\right)=0 \tag{3.28}$$

The matching conditions are that $\psi(r)$ and its first derivative are continuous at $r=h$, along with the following jump conditions on the higher derivatives of $\psi(r)$ at $r=h$ which are imposed by the $\delta'(r-h)$ term

$$\left[D^2\psi\right] = -\frac{\kappa\psi(h)}{w_h-c} \tag{3.29}$$

$$\left[D^3\psi\right] = -\frac{\kappa\psi(h)}{h(w_h-c)} \tag{3.30}$$

If the Boussinesq approximation is not made, then the axisymmetric stability operator for the two-fluid system is given by

$$\begin{aligned}&(\mathcal{L}-k^2)^2\psi - i\,k\,Re\,\rho_B\,\left((w_B-c)(\mathcal{L}-k^2)\psi-(\mathcal{L}w_B)\psi\right)\\ &\quad+\frac{\kappa\psi(h)}{h(w_h-c)}r\delta'(r-h)+i\,k\,\kappa\,Fr^2\,\delta(r-h)\left((w_h-c)\psi'(h)-w_h'\psi(h)\right)=0\end{aligned} \tag{3.31}$$

As in the two dimensional case we perform the asymptotic expansion in small pa-

rameters $k\,Re$ and k^2

$$\begin{aligned}\psi(r) &= \psi_0(r) + k\,Re\,\psi_1(r) + k^2\psi_2(r) + O(k^2Re^2, k^4)\\ c &= c_0 + k\,Re\,c_1 + k^2c_2 + O(k^2Re^2, k^4)\end{aligned}$$

We will investigate primarily the long wave asymptotics provided by $\psi_1(r)$ and c_1.

3.2.1 Leading order

At leading order, $\psi_0(r)$ must satisfy the homogeneous differential equation

$$\mathcal{L}^2\psi_0 + \frac{\gamma}{h}\psi_0(h)r\delta'(r-h) = 0$$

where

$$\gamma = \frac{\kappa}{w_h - c_0}$$

The solution can be expressed as

$$\psi_0 = b_1^0 f_1(r) + b_2^0 f_2(r) + b_3^0 f_3(r) + b_4^0 f_4(r) + \gamma\psi_0(h)\psi_{pw}(r)$$

Each $f_k(r)$ satisfies $\mathcal{L}^2 f_k = 0$

$$\begin{aligned}f_1(r) &= (r^2-1)^2\\ f_2(r) &= 1 - r^2\left(1 - \log r^2\right)\\ f_3(r) &= (r^2-a^2)^2\\ f_4(r) &= a^2 - r^2\left(1 - \log\frac{r^2}{a^2}\right)\end{aligned}$$

This basis has been chosen to simplify the boundary conditions as much as possible. Notice that

$$\begin{aligned} f_1(1) &= f_2(1) = 0 \\ f_1'(1) &= f_2'(1) = 0 \\ f_3(a) &= f_4(a) = 0 \\ f_3'(a) &= f_4'(a) = 0 \end{aligned}$$

The piece-wise function $\psi_{pw}(r)$ is given by

$$\psi_{pw}(r) = \frac{1}{4}\begin{cases} h^2 - r^2\left(1 - \log\frac{r^2}{h^2}\right) & \text{if} \quad a \le r \le h \\ 0 & \text{if} \quad h < r \le 1 \end{cases}$$

and satisfies the jump conditions imposed by a $\delta'(r-h)$ term

$$\mathcal{L}^2\psi_{pw} + \frac{r}{h}\delta'(r-h) = 0$$

$\psi_0(r)$ must satisfy homogeneous boundary conditions

$$\begin{aligned} 0 = \psi_0(a) &= b_1^0 f_1(a) + b_2^0 f_2(a) + b_3^0 f_3(a) + b_4^0 f_4(a) + \gamma\psi_0(h)\psi_{pw}(a) \\ 0 = \psi_0'(a) &= b_1^0 f_1'(a) + b_2^0 f_2'(a) + b_3^0 f_3'(a) + b_4^0 f_4'(a) + \gamma\psi_0(h)\psi_{pw}'(a) \\ 0 = \psi_0(1) &= b_1^0 f_1(1) + b_2^0 f_2(1) + b_3^0 f_3(1) + b_4^0 f_4(1) \\ 0 = \psi_0'(1) &= b_1^0 f_1'(1) + b_2^0 f_2'(1) + b_3^0 f_3'(1) + b_4^0 f_4'(1) \end{aligned}$$

To treat these boundary conditions we form the following matrices

$$\mathbf{M_1} = \begin{pmatrix} f_1(a) & f_2(a) & 0 & 0 \\ f_1'(a) & f_2'(a) & 0 & 0 \\ 0 & 0 & f_3(1) & f_4(1) \\ 0 & 0 & f_3'(1) & f_4'(1) \end{pmatrix}$$

$$\mathbf{M_2} = \begin{pmatrix} \psi_{pw}(a) \\ \psi'_{pw}(a) \\ 0 \\ 0 \end{pmatrix} \cdot \begin{pmatrix} f_1(h) & f_2(h) & f_3(h) & f_4(h) \end{pmatrix}$$

Let

$$\mathbf{M} = \mathbf{M_1} + \gamma \mathbf{M_2}$$

Then to satisfy the homogeneous boundary conditions, we must have

$$\mathbf{M} \cdot \mathbf{b_0} = \mathbf{0}$$

As in the two dimensional case, we use the Leibniz rule, and find that $\det \mathbf{M} = 0$ if and only if $\det \mathbf{A} = 0$, where

$$\mathbf{A} = \begin{pmatrix} f_1(a) & f_2(a) \\ f'_1(a) & f'_2(a) \end{pmatrix} + \gamma \begin{pmatrix} \psi_{pw}(a) \\ \psi'_{pw}(a) \end{pmatrix} \cdot \begin{pmatrix} f_1(h) & f_2(h) \end{pmatrix} \tag{3.32}$$

For convenience, we let

$$\mathbf{c_1} = \begin{pmatrix} f_1(a) \\ f'_1(a) \end{pmatrix}, \mathbf{c_2} = \begin{pmatrix} f_2(a) \\ f'_2(a) \end{pmatrix}, \mathbf{c_3} = \begin{pmatrix} \psi_{pw}(a) \\ \psi'_{pw}(a) \end{pmatrix}$$

Then using the multilinearity of the determinant

$$\begin{aligned} \det \mathbf{A} &= \det \left((\mathbf{c_1}, \mathbf{c_2}) + \gamma (f_1(h)\mathbf{c_3}, f_2(h)\mathbf{c_3}) \right) \\ &= \det (\mathbf{c_1}, \mathbf{c_2}) + \gamma f_1(h) \det (\mathbf{c_1}, \mathbf{c_3}) - \gamma f_2(h) \det (\mathbf{c_2}, \mathbf{c_3}) \end{aligned}$$

This formula can be written more concisely in terms of Wronskians

$$\det \mathbf{A} = \mathbf{W}(f_1, f_2)(a) + \gamma \left(f_2(h)\mathbf{W}(f_1, \psi_{pw})(a) - f_1(h)\mathbf{W}(f_2, \psi_{pw})(a) \right)$$

Upon further simplification, this becomes

$$\det \mathbf{A} = \mathbf{W}(f_1, f_2)(a) + \gamma \begin{vmatrix} \mathbf{W}(f_1, \psi_{pw})(a) & \mathbf{W}(f_2, \psi_{pw})(a) \\ f_1(h) & f_2(h) \end{vmatrix}$$

Substituting the definition of γ and solving for c_0 gives

$$c_0 = w_h - \frac{\kappa}{\gamma} = w_h + \kappa \frac{\begin{vmatrix} \mathbf{W}(f_1, \psi_{pw})(a) & \mathbf{W}(f_2, \psi_{pw})(a) \\ f_1(h) & f_2(h) \end{vmatrix}}{\mathbf{W}(f_1, f_2)(a)}$$

Evaluating $f_{1,2}$ and ψ_{pw} at the appropriate values gives an expression for c_0 in terms of κ, h, and a

$$\begin{aligned} \mu\, c_0 = &\left(1 - \frac{\kappa}{2}\eta^2\right)(1 + \log h) \\ &- \left(h^2 + a^2 + a^2 \log \frac{h^2}{a^2}\right) + \frac{\kappa}{2}\left(-h^4 + a^4 + (3h^4 + a^4)\log \frac{h}{a}\right) \\ &+ h^2 a^2 (1 - 2\log a) + a^4 \log h \\ &+ \frac{\kappa}{2} h^2 a^2 \left(h^2 - a^2\right) + \frac{\kappa}{2} h^2 (h^4 + a^4) \log a \\ &+ \frac{\kappa}{2} h^2 a^2 \left(-3h^2 + a^2 + a^2 \log \frac{h^2}{a^2}\right) \log h \end{aligned} \tag{3.33}$$

This expressions has been ordered to respect the asymptotic scaling of $\kappa \gg 1$ and $a \ll h \ll 1$. Note that μ and η are defined in terms of a and h by (1.24) and (1.23) respectively. As in the two dimensional case, this formula for the propagation speed of disturbances matches the formula for the characteristics speeds (2.21) exactly. To leading order in the asymptotic limit of $\kappa \gg 1$ and $a \ll h \ll 1$, the expression for c_0 simplifies to

$$c_0 \sim \frac{1 + \log h}{1 + \log a}\left(1 - \frac{\kappa}{2}\eta^2\right) \qquad \text{for } \kappa \gg 1, a \ll h \ll 1 \tag{3.34}$$

Since c_0 is real this indicates neutral stability at leading order and stability must

be determined at the next order. Solving for the coefficients gives

$$\begin{aligned} b_1^0 &= \log\frac{h^2}{a^2} + h^2\log a^2 - a^2\log h^2 \\ b_2^0 &= -(1-a^2)\left((1+a^2)\log\frac{h^2}{a^2} - 2(h^2-a^2)\right) \\ b_3^0 &= 0 \\ b_4^0 &= 0 \end{aligned}$$

This leads to a convenient simplification

$$\gamma\psi_0(h) = -8\mu$$

The leading order eigenfunction is given by scalar multiples of

$$\psi_0(r) = b_1^0(r^2-1)^2 + b_2^0\left(1 - r^2\left(1-\log r^2\right)\right) - 8\mu\psi_{pw}(r)$$

3.2.2 First correction

At order $k\,Re$, $\psi_1(r)$ must satisfy the inhomogeneous differential equation

$$\mathcal{L}^2\psi_1 + \gamma\left(\psi_1(h) - \frac{8\mu}{\kappa}c_1\right)\frac{r}{h}\delta'(r-h) = i(w_B - c_0)\mathcal{L}\psi_0 - i(\mathcal{L}w_B)\psi_0 \tag{3.35}$$

The solution can be written as

$$\begin{aligned} \psi_1(r) =& b_1^1 f_1(r) + b_2^1 f_2(r) + b_3^1 f_3(r) + b_4^1 f_4(r) \\ &+ \gamma\left(\psi_1(h) - \frac{8\mu}{\kappa}\,c_1\right)\psi_{pw}(r) + \psi_p(r) \end{aligned}$$

$\psi_p(r)$ is a piecewise function

$$\psi_p(r) = \begin{cases} p_L(r) & a < r \le h \\ p_R(r) & h < r \le 1 \end{cases}$$

where $p_L(r)$ and $p_R(r)$ are particular solutions to the inhomogeneous ordinary differential equation. The initial conditions for these solutions are

$$p_{L,R}(h) = p'_{L,R}(h) = p''_{L,R}(h) = p'''_{L,R}(h) = 0 \tag{3.36}$$

To satisfy the homogeneous boundary conditions we must have that

$$\begin{aligned} b_1^1 f_1(a) + b_2^1 f_2(a) + \gamma\psi_1(h)\psi_{pw}(a) &= -p_L(a) + \frac{8\gamma\mu}{\kappa} c_1 \psi_{pw}(a) \\ b_1^1 f_1'(a) + b_2^1 f_2'(a) + \gamma\psi_1(h)\psi'_{pw}(a) &= -p'_L(a) + \frac{8\gamma\mu}{\kappa} c_1 \psi'_{pw}(a) \\ b_3^1 f_3(1) + b_4^1 f_4(1) &= -p_R(1) \\ b_3^1 f_3'(1) + b_4^1 f_4'(1) &= -p'_R(1) \end{aligned}$$

The last two equations allow for us to solve for b_3^1 and b_4^1 directly. Let

$$\mathbf{D} = \begin{pmatrix} f_3(1) & f_4(1) \\ f_3'(1) & f_4'(1) \end{pmatrix}$$

Then b_3^1 and b_4^1 are given by

$$\begin{pmatrix} b_3^1 \\ b_4^1 \end{pmatrix} = -\mathbf{D^{-1}} \begin{pmatrix} p_R(1) \\ p'_R(1) \end{pmatrix}$$

For convenience, let

$$\zeta = b_3^1 f_3(h) + b_4^1 f_4(h)$$

Then b_1^1 and b_2^1 must satisfy the matrix problem

$$\mathbf{A} \begin{pmatrix} b_1^1 \\ b_2^1 \end{pmatrix} = - \begin{pmatrix} p_L(a) \\ p'_L(a) \end{pmatrix} + \gamma \left(\zeta + \frac{8\,\mu\, c_1}{\kappa} \right) \begin{pmatrix} \psi_{pw}(a) \\ \psi'_{pw}(a) \end{pmatrix} \equiv \mathbf{y}$$

where $\mathbf{A}$ is defined by (3.32). For this problem to have a solution, it is required that $\mathbf{y}$

is orthogonal to the null-space of the adjoint of $\mathbf{A}$, which is given by the linear space of

$$\mathbf{v} = \begin{pmatrix} v_1 \\ v_2 \end{pmatrix} = \begin{pmatrix} 2a\left((1-h^2)^2\log a^2 + 2(1-a^2)(1-h^2+h^2\log h^2)\right) \\ -a^2(1-h^2)^2\log a^2 + (1-a^2)\left((1-h^2)(h^2-a^2) + (1-a^2)h^2\log h^2\right) \end{pmatrix}$$

For convenience we write $\mathbf{y}$ as

$$\mathbf{y} = \begin{pmatrix} y_1 \\ y_2 \end{pmatrix} = \begin{pmatrix} \alpha_1 \\ \alpha_2 \end{pmatrix} + c_1 \begin{pmatrix} \beta_1 \\ \beta_2 \end{pmatrix}$$

Then α_1 and α_2 are given by

$$\begin{pmatrix} \alpha_1 \\ \alpha_2 \end{pmatrix} = -\begin{pmatrix} p_L(a) \\ p_L'(a) \end{pmatrix} + \gamma\zeta \begin{pmatrix} \psi_{pw}(a) \\ \psi_{pw}'(a) \end{pmatrix}$$

and β_1 and β_2 are given by

$$\beta = \begin{pmatrix} \beta_1 \\ \beta_2 \end{pmatrix} = \frac{8\,\gamma\,\mu}{\kappa} \begin{pmatrix} \psi_{pw}(a) \\ \psi_{pw}'(a) \end{pmatrix}$$

Enforcing that $\mathbf{y}$ is orthogonal to $\mathbf{v}$, gives

$$c_1 = -\frac{\alpha_1 v_1 + \alpha_2 v_2}{\beta_1 v_1 + \beta_2 v_2} \tag{3.37}$$

In order to obtain the values for $p_L(a), p_L'(a), p_R(1), p_R'(1)$ we solve the fourth order inhomogeneous differential equation (3.35) with the specified initial conditions (3.36) using Mathematica - see Appendix F - and substitute the obtained values into (3.37). The resulting exact expression for c_1 can be represented as

$$\mu^3 c_1 = \frac{i\kappa}{2304}\pi_1(a^2, h^2, \log a, \log h) + \frac{i\kappa^2}{3072}\pi_2(a^2, h^2, \log a, \log h) \tag{3.38}$$

where π_1 and π_2 are each polynomials of the four variables $a^2, h^2, \log a,$ and $\log h$. The lists of coefficients of these polynomials are given in Appendix D, and the length of the

lists are 768 and 1280 respectively.

3.2.3 Axisymmetric stability discussion

Since the expression for c_1 is imaginary, its sign provides information about stability or instability. In order to obtain a more workable expression we will approximate (3.38) for the asymptotic regime under which most of the experiments are conducted: $\kappa \gg 1$ and $a \ll h \ll 1$ (allowing for the $\log a$ and $\log h$ to remain order one). The leading order expression for c_1 under this asymptotic scaling is

$$\mu^3 c_1 \sim -\frac{i}{6144}\,\log\frac{h^2}{a^2}\,\kappa\eta^2\,\left(92 - 31\kappa\eta^2 + 32\log h\left(1 - \frac{\kappa}{2}\eta^2\right)\right) \qquad \text{leading order for } \kappa \gg 1,\ a \ll h \ll 1 \tag{3.39}$$

Unfortunately, this expression has been found to be less than adequate for practical use, and therefore we compute the first correction c_1 in this asymptotic regime. This gives

$$\begin{aligned}
\mu^3 c_1 \sim\ & -\frac{i}{6144}\,\log\frac{h^2}{a^2}\,\kappa\eta^2\,\left(92 - 31\kappa\eta^2 + 32\log h\left(1 - \frac{\kappa}{2}\eta^2\right)\right) \\
& + \frac{i}{2304}\kappa h^4 \Big\{ -438 - 247\log h + 768\log^2 h - 144\log^3 h \\
& \qquad -2\log a\left(367 + 575\log h - 396\log^2 h + 72\log^3 h\right) \\
& \qquad +2\log^2 a\left(-67 - 288\log h + 72\log^2 h\right) \Big\} \\
& + \frac{i}{3072}\kappa^2 h^6 \Big\{ -36 + 538\log h + 484\log^2 h - 864\log^3 h \\
& \qquad +\log a\left(-401 + 448\log h + 2172\log^2 h - 672\log^3 h\right) \\
& \qquad +2\log^2 a\left(-257 - 504\log h + 576\log^2 h\right) \\
& \qquad -40\log^3 a\,(1 + 12\log h) \Big\} \\
& \qquad \text{first correction for } \kappa \gg 1,\ a \ll h \ll 1
\end{aligned} \tag{3.40}$$

While this expression is not as compact as (3.39) it is much more workable than the exact expression (3.38) which is a polynomial in four variables with 2048 coefficients,

and it has been found that this expression is nearly indistinguishable from the exact expression (3.38) in the regime of parameters spanned by the experiments.

Since the exact expression for c_1 (3.38) is simply a polynomial in κ and κ^2, for a fixed a and h, the value of κ that gives $c_1 = 0$ is given by

$$\kappa_0(a,h) = -\frac{4}{3}\frac{\pi_1(a^2,h^2,\log a,\log h)}{\pi_2(a^2,h^2,\log a,\log h)}$$

This gives an explicit expression for the long-wave neutral stability curve. Similar expression for the neutral stability curves corresponding to the leading order (3.39) and the first correction (3.40) can be written explicitly as $\kappa_0(a,h)$.

Figure 3.4 shows the neutral stability curves corresponding to these three formulas (exact, leading order, and first correction) with shading indicating regions of stability. The bottom neutral stability curves corresponding to the exact formula and the first correction are nearly identical, while the leading order curve shows a substantial difference even though $h < 0.1$ for these bottom curves. Even in the right panel zoom, the exact expression and first correction are indistinguishable. For the top neutral stability curves both the leading order and the first correction curves are in error since these top curves do not lie in the asymptotic regime of validity. As in two dimensions the asymptotic formula (3.38) that is exact in a and h, but asymptotic for $k \ll 1$, gives the exact neutral stability curve with no approximation made. All of these curves are independent of the Reynolds number, and as in two dimensions the Reynolds number effects only the magnitude of damping or amplification.

Limit to unbounded domain

Consider the limit to the semi-infinite domain with $L \to \infty$ and all other dimensional parameters fixed. This implies that $\kappa \to \infty$, $a \to 0$, and $h \to 0$, and so the leading order correction for c_1 (3.39) becomes valid with the $\log h$ term asymptotically dominating. This gives the asymptotic expression for c_1

$$c_1 \sim -\frac{i\,\log\frac{h^2}{a^2}\,\kappa\eta^2\,\log h}{192(1+\log a)^3}\left(1-\frac{\kappa}{2}\eta^2\right) \qquad \text{for } \kappa \gg 1,\ a \ll h \ll 1,\ |\log h| \gg 1$$

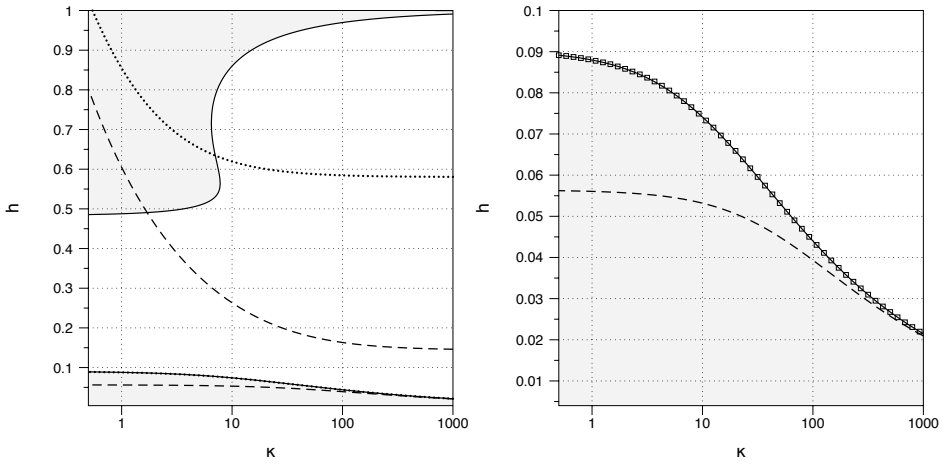

Figure 3.4: Axisymmetric bifurcation diagram. Left panel: Long-wave neutral stability curve using the exact expression for c_1 (solid line) from equation (3.38), the leading order expression (dashed line) from equation (3.39), and the first correction (dotted line) from equation (3.40), with the shading showing regions of stability and $a = 0.004$. Right panel: a blowup for small h along with the neutral stability curve given by the shooting method (boxes), with the fixed values of $Re = 1$, $k = 0.01$, and $a = 0.004$.

This expression is always negative for $\kappa\eta^2 < 2$ since both the terms $1+\log a$ and $\log h$ are negative in this limit. Thus in this limit to the semi-infinite domain ($L \to \infty$) instability is not realized unless $\kappa\eta^2 > 2$. The formula for the speed of characteristics (2.23) from lubrication theory in this same asymptotic regime shows that $\lim_{t\to\infty} \kappa\eta^2 = 2$. Therefore it can be concluded that in the limit to the semi-infinite domain the entrained layer grows to a size that is neutrally stable which is a rather striking result!

Figure 3.5 illustrates how this is different than the situation in two-dimensions. In two-dimensions for asymptotic large κ, the curve of neutral stability is given by $\kappa h^2 = 10/19$ as can be seen from formula (3.21). Meanwhile, the curve of zero propagation speed, which is equivalent to h_∞, is given by $\kappa h^2 = 1$, and so these two curves remain separated as $\kappa \to \infty$. However, in the axisymmetric geometry the curves of neutral stability and the curve of zero propagation speed are both given by the relationship $\kappa\eta^2 = 2$ as $\kappa \to \infty$, and so they approach one another in this limit. Note, however that in two dimensions although the curves of neutral stability and h_∞ remain separated the magnitude of c_1 tends to zero as $\kappa \to \infty$, so that here too h_∞ becomes neutrally stable although in a different manner than in the axisymmetric geometry.

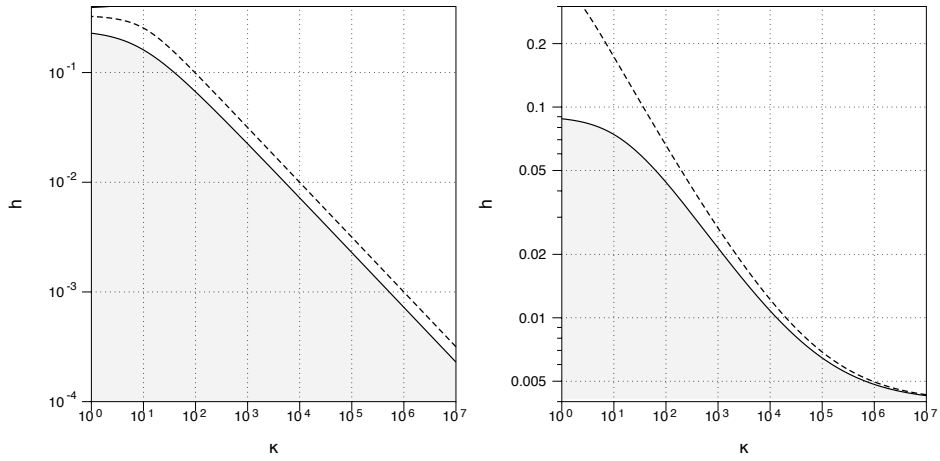

Figure 3.5: Log-log plot of neutral stability curves (solid lines) and zero-propagation speed, or h_∞, curves (dashed lines) for large κ in two-dimensons (left) and the axisymmetric geometric (right) with $a = 0.004$.

3.3 Numerical shooting method

3.3.1 Two dimensional two-fluid problem

We have developed a numerical shooting method to solve for the eigenvalue of stability operator both in the two dimensional case (3.5) and the three dimensional case (3.27). In the two dimensional case we divide the domain into two regions. The first region is $0 \leq x \leq h$ and the second is $h \leq x \leq 1$. In the first region, we have a basis of two functions ψ_{1L} and ψ_{2L}, which solve the classic Orr-Somerfeld equation (3.6) for a given eigenvalue c with the initial conditions $\psi_{1L}(0) = \psi'_{1L}(0) = \psi'''_{1L}(0) = 0$, and $\psi_{2L}(0) = \psi'_{2L}(0) = \psi''_{2L}(0) = 0$, and $\psi''_{1L}(0) = \psi'''_{2L}(0) = 1$. In the second domain, we have the basis of solutions to (3.6) ψ_{1R} and ψ_{2R}, with the initial conditions $\psi_{1R}(1) = \psi'_{1R}(1) = \psi'''_{1R}(1) = 0$, and $\psi_{2R}(1) = \psi'_{2R}(1) = \psi''_{2R}(1) = 0$, and $\psi''_{1R}(1) = \psi'''_{2R}(1) = 1$.

These four initial value problems for ψ_{1L}, ψ_{2L}, ψ_{1R}, and ψ_{2R} are solved by expressing each problem as a first order system of ordinary differential equations, and integrating using Matlab's ode45 which is an explicit Runge-Kutta scheme utilizing the Dormand-Prince (4,5) pair. For $\psi = \psi_{1L}$, ψ_{2L}, ψ_{1R}, or ψ_{2R} we let

$$\mathbf{y}(x) = (\psi, \psi', \psi'', \psi''')$$

and let

$$\mathbf{A} = \begin{pmatrix} 0 & 1 & 0 & 0 \\ 0 & 0 & 1 & 0 \\ 0 & 0 & 0 & 1 \\ A_{4,1}(x) & 0 & A_{4,3}(x) & 0 \end{pmatrix}$$

where

$$\begin{aligned} A_{4,1}(x) &= -ikRe\left(k^2(w_B - c) + w_B''\right) - k^4 \\ A_{4,3}(x) &= ikRe(w_B - c) + 2k^2 \end{aligned}$$

Then the first order system to solve is

$$\mathbf{y}'(x) = \mathbf{A}(x)\,\mathbf{y}(x) \tag{3.41}$$

with the respective initial conditions imposed for ψ_{1L} , ψ_{2L}, ψ_{1R}, and ψ_{2R}.

For a given c, the solution to the boundary value problem (3.5) is represented as a linear combination of the basis functions

$$\psi(x;c) = \begin{cases} a\,\psi_{1L}(x) + b\,\psi_{2L}(x) & \text{if} \quad 0 < x \le h \\ -c\,\psi_{1R}(x) - d\,\psi_{2R}(x) & \text{if} \quad h < x \le 1 \end{cases}$$

The continuity of ψ and its first and third derivatives at $x = h$ imply the following conditions

$$\begin{aligned} [\psi(h)] = a\,\psi_{1L}(h) + b\,\psi_{2L}(h) + c\,\psi_{1R}(h) + d\,\psi_{2R}(h) &= 0 \\ [\psi'(h)] = a\,\psi'_{1L}(h) + b\,\psi'_{2L}(h) + c\,\psi'_{1R}(h) + d\,\psi'_{2R}(h) &= 0 \\ [\psi'''(h)] = a\,\psi'''_{1L}(h) + b\,\psi'''_{2L}(h) + c\,\psi'''_{1R}(h) + d\,\psi'''_{2R}(h) &= 0 \end{aligned}$$

The jump condition on the second derivative (3.7) implies that

$$[\psi''(h)] + \frac{\kappa\psi(h)}{w_h - c} =$$
$$a\,\psi''_{1L}(h) + b\,\psi''_{2L}(h) + c\,\psi''_{1R}(h) + d\,\psi''_{2R}(h) + \frac{\kappa}{w_h - c}\left(a\,\psi_{1L}(h) + b\,\psi_{2L}(h)\right) = 0$$

For a given eigenvalue c, let the matrix $\mathbf{M_c}$ be given by

$$\mathbf{M_c} = \begin{pmatrix} \psi_{1L}(h) & \psi_{2L}(h) & \psi_{1R}(h) & \psi_{2R}(h) \\ \psi'_{1L}(h) & \psi'_{2L}(h) & \psi'_{1R}(h) & \psi'_{2R}(h) \\ \psi''_{1L}(h) & \psi''_{2L}(h) & \psi''_{1R}(h) & \psi''_{2R}(h) \\ \psi'''_{1L}(h) & \psi'''_{2L}(h) & \psi'''_{1R}(h) & \psi'''_{2R}(h) \end{pmatrix} + \frac{\kappa}{w_h - c} \begin{pmatrix} 0 & 0 & 0 & 0 \\ 0 & 0 & 0 & 0 \\ \psi_{1L}(h) & \psi_{2L}(h) & 0 & 0 \\ 0 & 0 & 0 & 0 \end{pmatrix}$$

Then the condition that $\psi(x;c)$ solves (3.5) is that $F(c) \equiv \det(\mathbf{M_c}) = 0$. The function $F(c)$ is a complex valued function of one complex variable c, and we use a standard secant method to find a root of the function and thus an eigenvalue of the stability operator (3.5). Additionally, the function $F(c)$ was multiplied by the normalization factor e^{-2k} before the root finding procedure was applied to its determinant. This normalization factor was introduced so that the norm of the function $F(c)$ would be of the same order of magnitude for varying k values and therefore the same precision of the secant method may be used for these varying k values. The factor e^{-2k} was used since for a fixed Re and large k, the eigenfunctions asymptotically tend to $e^{\pm k}$, and thus the norm of $\mathbf{M_c}$ is generically of order e^{2k} in this limit.

For the three dimensional axisymmetric geometry the shooting method is performed in a similar manner except that the functions ψ_{1L}, ψ_{2L}, ψ_{1R}, and ψ_{1R} solve the axisymmetric Orr-Somerfeld equation (3.28) with the jump condition (3.29) and (3.30) enforced at $r = h$. These jump condition result in the matrix

$$\mathbf{M_c}^{3D} = \begin{pmatrix} \psi_{1L}(h) & \psi_{2L}(h) & \psi_{1R}(h) & \psi_{2R}(h) \\ \psi'_{1L}(h) & \psi'_{2L}(h) & \psi'_{1R}(h) & \psi'_{2R}(h) \\ \psi''_{1L}(h) & \psi''_{2L}(h) & \psi''_{1R}(h) & \psi''_{2R}(h) \\ \psi'''_{1L}(h) & \psi'''_{2L}(h) & \psi'''_{1R}(h) & \psi'''_{2R}(h) \end{pmatrix} + \frac{\kappa}{w_h - c} \begin{pmatrix} 0 & 0 & 0 & 0 \\ 0 & 0 & 0 & 0 \\ \psi_{1L}(h) & \psi_{2L}(h) & 0 & 0 \\ \frac{1}{h}\psi_{1L}(h) & \frac{1}{h}\psi_{2L}(h) & 0 & 0 \end{pmatrix}$$

which must have vanishing determinant.

3.3.2 Condition of the ODE system

The system (3.41) is not well-conditioned for all values of k and Re. In particular, for k fixed and large Re, the eigenvalues of $\mathbf{A}$ (for some fixed x) are generically order ± 1 and $\pm\sqrt{Re}$ [8]. This implies that for large values of Re, there can be no integration scheme to accurately solve (3.41) either forwards or backwards, no matter how small of a step-size is taken in the scheme. A number of techniques have been developed in order to resolve this issue, including the Riccati transformation method [24, 8, 25, 26] to name just a one. See [9] pp. 207-211, for additional discussion of techniques and references.

In the present study, we are most interested in stability analysis for long waves and moderate to low Reynolds numbers, in which case the system (3.41) is well-conditioned and may be integrated directly. To make a very rough estimate for the allowable Reynolds number, we note that if $Re = 1300$, then the largest eigenvalue of $\mathbf{A}$ is generically order $\sqrt{1300} \approx 36$, in which case the corresponding eigenfunction evaluated at $x = 1$ would be roughly of order $\exp 36 \approx 4.3 \cdot 10^{15}$. For a double-precision computation in which round-off errors are of order 10^{-16}, the condition of the system would yield errors that are at least order one, where we have not even taken into account the error induced by an integration scheme. Therefore, this should be interpreted as a very high overestimate of the maximal allowable Reynolds number, above which the system (3.41) is certainly ill-conditioned. It is expected that we would need to take a Reynolds number much lower than 1300 in order to have a well-conditioned system.

3.3.3 Smooth density transition

We apply the shooting method to the background solutions corresponding to a smoothed density profile with transition lengthscale $\lambda \ll h$ given by (1.13). In this case, we have a basis of two function ψ_1 and ψ_2 which solve (3.3). The initial conditions for ψ_1 are $\psi_1(0) = \psi_1'(0) = \psi_1'''(0) = 0$ and $\psi_{1L}''(0) = 1$. The initial conditions for ψ_2 are $\psi_2(0) = \psi_2'(0) = \psi_2''(0) = 0$ and $\psi_{2L}'''(0) = 1$. As before, we solve each fourth order differential equation for ψ_1 and ψ_2 by representing it as a first-order system. We let

$$\mathbf{M_c}^{smooth} = \begin{pmatrix} \psi_1(1) & \psi_2(1) \\ \psi_1'(1) & \psi_2'(1) \end{pmatrix}$$

Then eigenvalue condition that a linear combination of ψ_1 and ψ_2 solve the homogeneous boundary value problem (3.5) is equivalent to $F(c) \equiv \det \mathbf{M_c}^{smooth} = 0$.

In the two-fluid system, the vertical layering density term in the stability operator is only supported at $x = h$, and thus as long as $w_h \neq c$, there is no singularity in the operator. However, once the two-fluid system is approximated by a smooth density profile with lengthscale λ the vertical density layering term may be supported over the entire interval $(0, 1)$ and thus if $w_B(x) = c$ somewhere in the interval, there is a singularity in the stability operator. In this case, the shooting method will not be accurate without a deformation of the path of integration into the complex plane to avoid the singularity. On the other hand, as long as the imaginary component of c is nonzero, there will be no singularity on the real line. In this case the shooting method will converge provided that c_i is not too small so that $w_B(x) - c$ is bounded away from zero to an acceptable numerical tolerance.

Therefore, to avoid the complexities of deforming the integration path we will apply the shooting method for parametric values of κ, Re, and k for which c_i is nonzero in the two-fluid case. For $\lambda \ll h$, the smooth density solution approximates the two-fluid solution, and thus it is reasonable to expect that c_i for the smooth density solution will be nonzero as well.

3.3.4 Stability results: shooting method and asymptotic formulas

The numerical shooting method has been shown to agree with the asymptotic results for both the two dimensional problem and the axisymmetric problem, and likewise demonstrates a transition from stability to instability as h is increased for a fixed κ.

Two-dimensional stability results

Figure 3.6 shows a comparison of the imaginary component of the eigenvalue as computed by the shooting method and computed by the long-wave asymptotic formula (3.20) for $h = h_\infty$ and $h = 0.5\, h_\infty$, showing excllent agreement in the slope of the c_i curve at $k = 0$. The plot shows stability for $h = 0.5\, h_\infty$ and instability for $h = h_\infty$. For this plot $\kappa = 100$ which gives $h_\infty \approx 0.0986$.

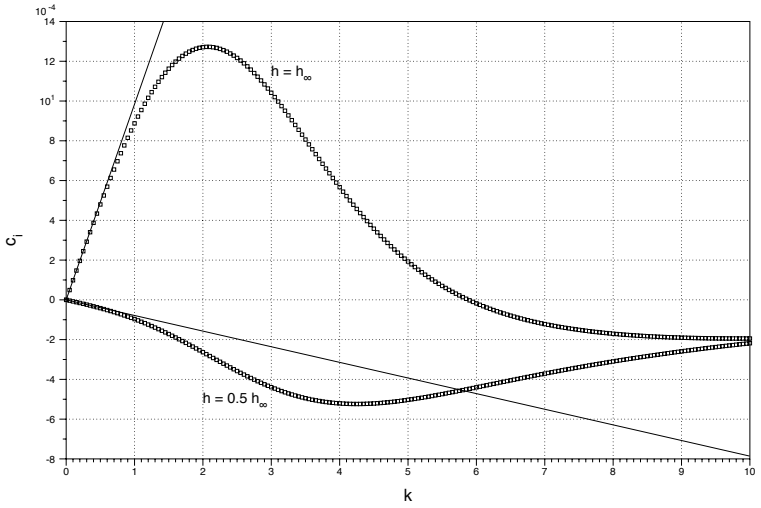

Figure 3.6: Two dimensions. Imaginary component of c from the numerical shooting method (boxes) for $h = 0.5\,h_\infty$ and h_∞ with $\kappa = 100$ and $Re = 1$, shown with formula (3.20) (solid lines).

For a fixed value of κ and Re and a fixed small k, it is possible to search for the h for which $c_i = 0$ using the shooting method, thus constructing the neutral stability curve. Figure 3.2 shows the neutral stability curve as computed by the numerical shooting method as well as that from the asymptotic formula (3.20) and demonstrates nearly exact agreement between the two.

The left panel of Figure 3.7 shows the real component of the eigenvalue as computed from the shooting method for four values of h, along with the asymptotic formula (3.15) for small k, showing agreement as $k \to 0$. The right panel shows a zoom of the imaginary component for small k values demonstrating nearly exact agreement between the shooting method and the asymptotic formula (3.20).

Figure 3.8 illustrates the dependence of c_i on the variables k, h, and Re. The left panel shows $c_i(k)$ with $\kappa = 100$ and $Re = 1$ for four different h-values showing the transition from stability to instability as h is increased. The right panel shows this same plot overlaid with a plot of $0.1\,c_i(k)$ with $Re = 10$ and the two plots are very similar for all h-values. This illustrates the important point that the Reynolds number enters the imaginary component of the eigenvalue primarily as a multiplicative factor and does not alter the character of the functional dependence of c_i upon k, even for Reynolds numbers of up to 10 and wavenumbers of up to 10. The plot of $10\,c_i(k)$ with $Re = 0.1$ cannot be discerned from the plot of $c_i(k)$ with $Re = 1$ and therefore it is not

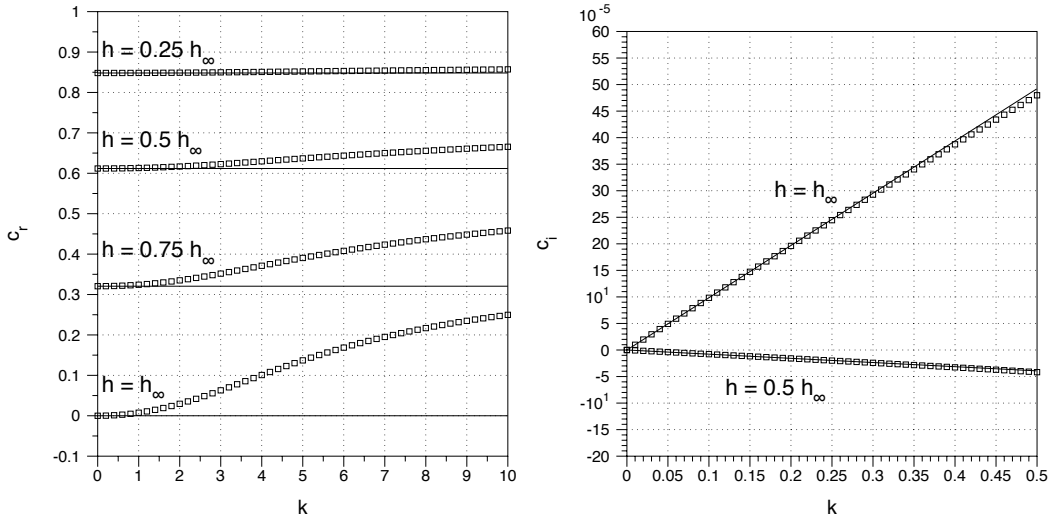

Figure 3.7: Two dimensions. Left panel: real component of c from the numerical shooting method (boxes) for $h = 0.25\,h_\infty$, $0.5\,h_\infty$, $0.75\,h_\infty$, and h_∞, with $\kappa = 100$ and $Re = 1$, shown with the asymptotic formula (3.15) (solid line). Right panel: imaginary component of c for $h = 0.5\,h_\infty$ and h_∞ for small k values, shown with formula (3.20) (solid lines).

shown, but this illustrates the role of the Reynolds number as a multiplicative factor even more dramatically for lower Reynolds numbers.

Figure 3.9 shows eigenvalue plots for the shear solutions (1.13) in which there is a smooth transition in the density profile, and illustrates the dependence of the stability properties on the length-scale λ of the transition region. As λ increases, corresponding to a more blurred density transition, both the real and imaginary parts of c decrease monotonically for all cases tested here. Therefore an unstable flow configuration becomes less unstable (slower amplification of disturbances) as the density profile is smoothed. We have no asymptotic results for the smoothed flows and therefore rely entirely on the shooting method for these results.

Axisymmetric stability results

For the axisymmetric geometry, Figure 3.10 shows a comparison of the imaginary component of the eigenvalue as computed by the shooting method and computed by the exact long-wave asymptotic formula (3.38) for $h = 0.5\,h_\infty$, $0.75\,h_\infty$ and h_∞, showing excllent agreement in the slope of the c_i curve at $k = 0$. The plot shows stability for

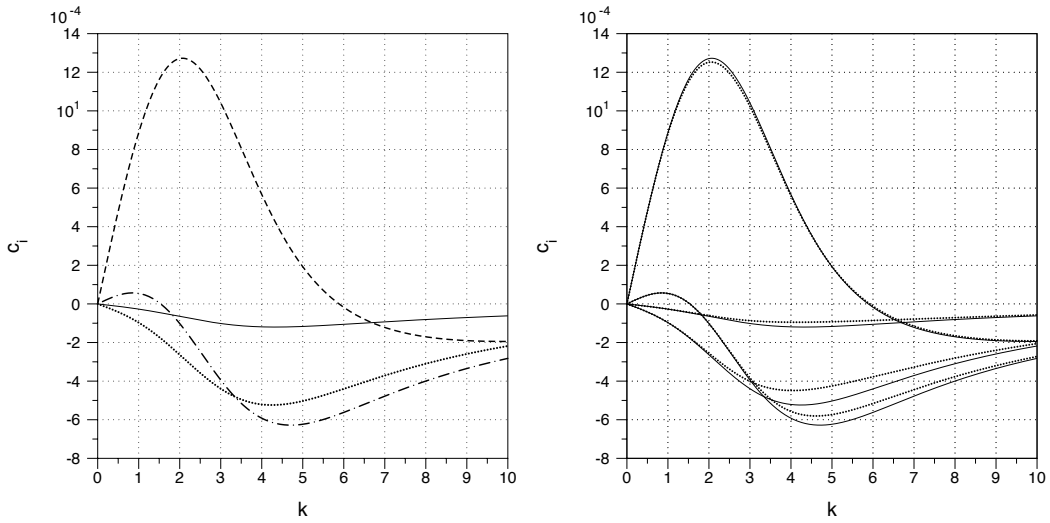

Figure 3.8: Two dimensions. Left panel: c_i from the numerical shooting method with $\kappa = 100$, $Re = 1$, and $h = 0.25\,h_\infty$ (solid line), $h = 0.5\,h_\infty$ (dotted line), $h = 0.75\,h_\infty$ (dot-dash line), $h = h_\infty$ (dashed line). Right panel: c_i rescaled by the Reynolds number: c_i for $Re = 1$ (solid lines) and $0.1\,c_i$ for $Re = 10$ (dotted lines) for the same four h values.

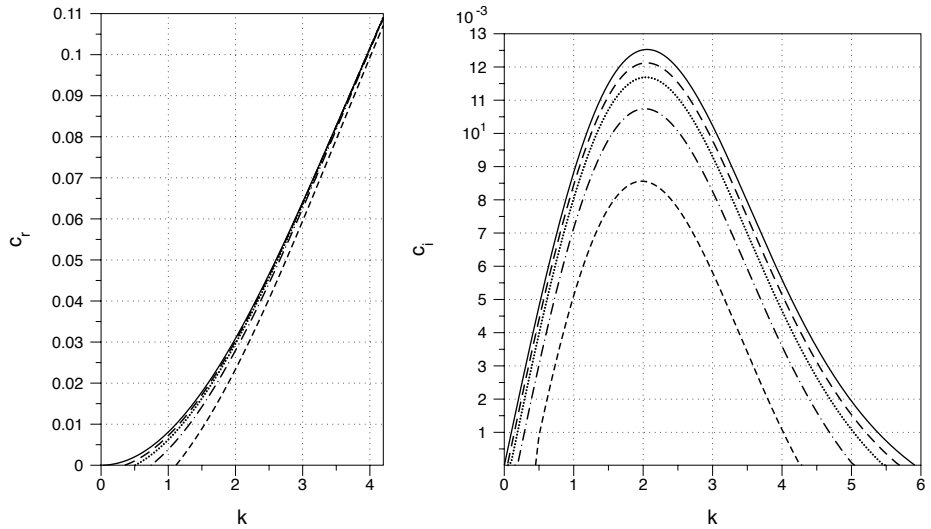

Figure 3.9: Two dimensions. The real part (left panel) and the imaginary part (right panel) of c from the numerical shooting method for the two-fluid system (solid line) compared to a smoothed density transition with lengthscale $\lambda = 0.005\,h$ (dashed line), $\lambda = 0.01\,h$ (dotted line), $\lambda = 0.02\,h$ (dot-dash line), and $\lambda = 0.04\,h$ (fine dash line), with $\kappa = 100$, $Re = 10$, and $h = h_\infty$.

$h = 0.5\,h_\infty$ and instability for $h = 0.75h_\infty$ and $h = h_\infty$. For this plot $\kappa = 25$ and $a = 0.004$ which gives $h_\infty \approx 1.1745$.

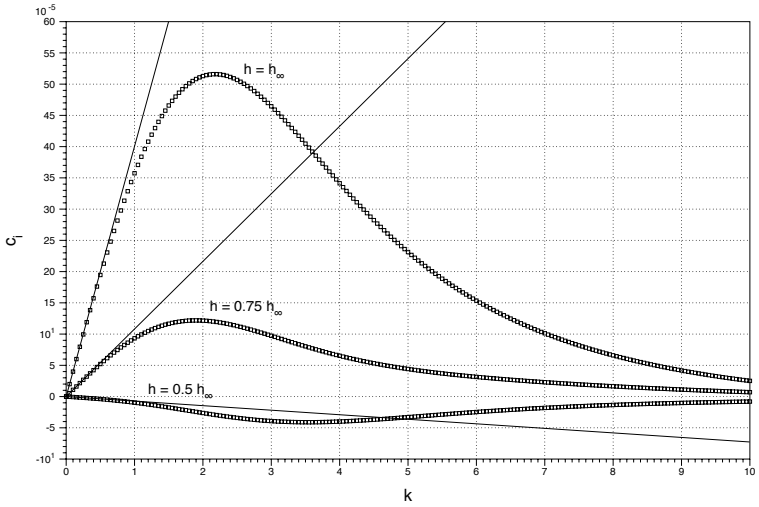

Figure 3.10: Axisymmetric geometry. Imaginary component of c from the numerical shooting method (boxes) for $h = 0.5\,h_\infty$, $0.75\,h_\infty$ and h_∞, with $\kappa = 25$, $a = 0.004$, and $Re = 1$, shown with formula (3.38) (solid lines).

Additionally, the neutral stability curve is constructed from the numerical shooting method using the same method as in two dimensions and is shown in Figure 3.4, along with the neutral stability curves from the various asymptotic formulas. This figure shows nearly exact agreement between the neutral stability curve given by the shooting method and the neutral stability curve given by the full expression for c_1 in equation (3.38).

The left panel of Figure 3.11 shows the real component of the eigenvalue as computed from the shooting method for four values of h, along with the exact asymptotic formula (3.33) for small k and the leading order formula (3.34), the two of which are nearly indistinguishable and show agreement with the numerically computed values as $k \to 0$. The right panel shows a blowup of the imaginary component for small k values demonstrating nearly exact agreement with the exact asymptotic formula (3.38) valid for small k. The leading order asymptotic formula (3.39) appears to be in substantial error, while the first correction formula (3.40) appears nearly identical to the full formula (3.38). This demonstrates that the leading order formula is an inadequate approximation, whereas the first correction is an excellent approximation to the full formula for c_1.

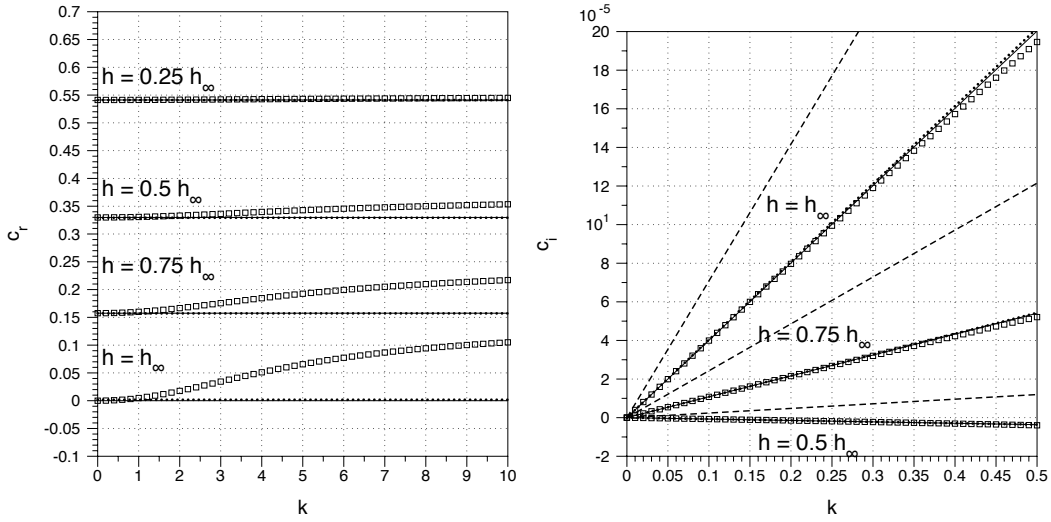

Figure 3.11: Axisymmetric geometry. Left panel: real component of c from the numerical shooting method (boxes) for $h = 0.25\,h_\infty$, $0.5\,h_\infty$, $0.75\,h_\infty$, and h_∞, with $\kappa = 25$, $a = 0.004$, and $Re = 1$, shown with formula (3.33) (solid lines) and formula (3.34) (dotted lines) which are nearly indistinguishable. Right panel: imaginary component of c for $h = 0.5\,h_\infty$, $0.75\,h_\infty$, and h_∞ for small k values, shown with formula (3.39) (dashed lines), formula (3.40) (dotted lines), and formula (3.38) (solid lines) where the latter two lines are nearly indistinguishable.

Chapter 4

Experiments

This chapter discusses the controlled laboratory experiment that has been performed to create the vertically layered flows that are the focus of this thesis. In the experiment, the axisymmetric shear flows (1.22) are created by towing a thin fiber vertically through an initially stable stratification. After a sufficient period of time, the layer of heavy fluid that is entrained by the fiber becomes oriented nearly vertically, forming what appears to be a column whose diameter is relatively constant along a large portion of the height of the experimental tank. Figure 4.1 shows a still shot from the experiment in which the columnar nature of the entrained fluid is evident.

Preliminary experiments were conducted using water as the fluid, which is presented in Section 4.2. In order to address some problems experienced in these water experiments, we used corn syrup and water solutions in later experiments and this is discussed in Section 4.3. Figure 4.1 shows an experiment conducted with corn syrup, in which the viscosity is roughly 30 Poise (viscosity measurements methods are discussed in Section 4.3.1). The Reynolds number, based on the towing velocity and the half-width of the tank L, is roughly 0.7 and the parameter κ is roughly 49.

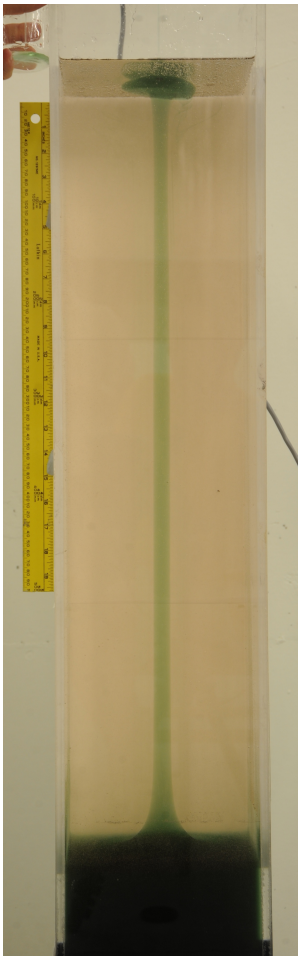

Figure 4.1: Experimental photograph using stratified corn-syrup. $Re = 0.7$ and $\kappa = 49$.

The experiment was photographed with a 12.1 megapixel Nikon D3 digital SLR camera and the images were analyzed using the software DataTank, created by David Adalsteinsson, allowing for a comparison of the dynamic evolution of the system with the theoretical predictions presented in the previous Chapters. The experimental measurements disconfirm the preliminary predictions derived from the analysis of steady solutions in semi-infinite domains in Chapter 1, while showing incontrovertible confirmation of the validity of the lubrication theory (Chapter 2) for predicting the time evolution of the miscible interface. Additionally, experimental observations are shown to be in agreement with the homogeneous density solution presented in Chapter 2 within the appropriate limit of short time.

While flows have been created in which the observed size of the entrained layer is large enough to render the flow unstable as predicted by theoretical analysis in Chapter 3, instability has not been conclusively observed in the experiment due to the small growth rates of the instabilities within the parameter range accessible by the experiments.

4.1 Experimental design

In the experiment, a layer of lower density fluid (top fluid) is poured on top of a layer of higher density fluid (bottom fluid) to create an initial stable stratification. The bottom fluid is made more dense by the addition of salt. The two fluids are miscible and the diffusivity of salt in the solution has been measured to be roughly 1.3×10^{-5} cm^2/s (see Appendix B) so that effects of diffusivity are negligible on the timescale of the experiment which is always less than twenty minutes. The fluids are poured in such a way as to maintain a sharp density transition between the two fluids. The size of the sharp density transition is not measured directly, but from optical observation it appears much less than 1 cm, and more likely on the order of 1 mm. The fiber is then impulsively towed vertically through the fluid at a constant speed, entraining a layer of the dyed bottom fluid which eventually becomes columnar in the top region of the experimental tank while still highly curved in a small region near the initial interface - see Figure 4.2b for an illustration.

We use 15 lb and 30 lb test monofilament fishing line for the fiber and it is towed by a stepper motor located atop the experimental tank. The stepper motor is the SureStep 23055 and is controlled by the SureStep micro-step drive 4035, with a signal

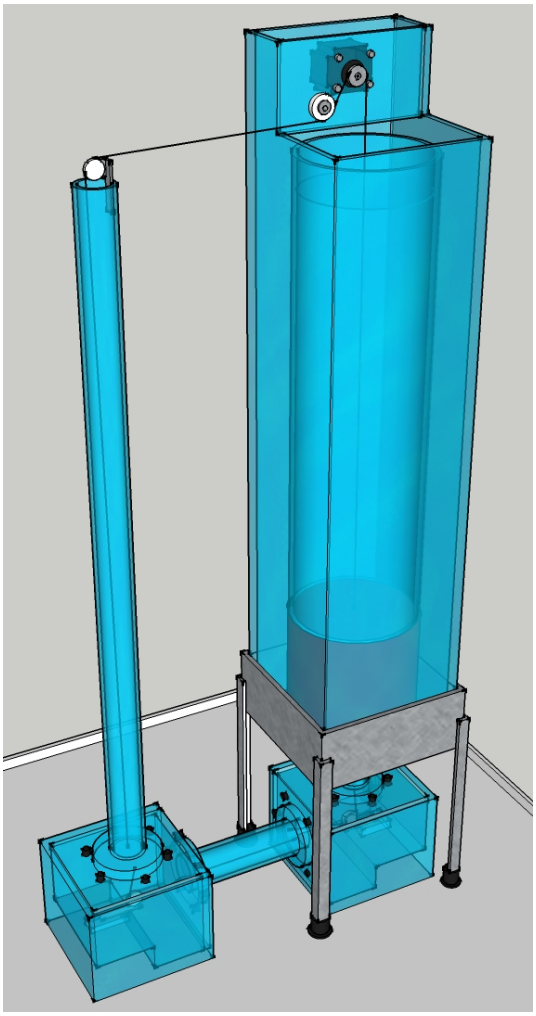

(a) Schematic

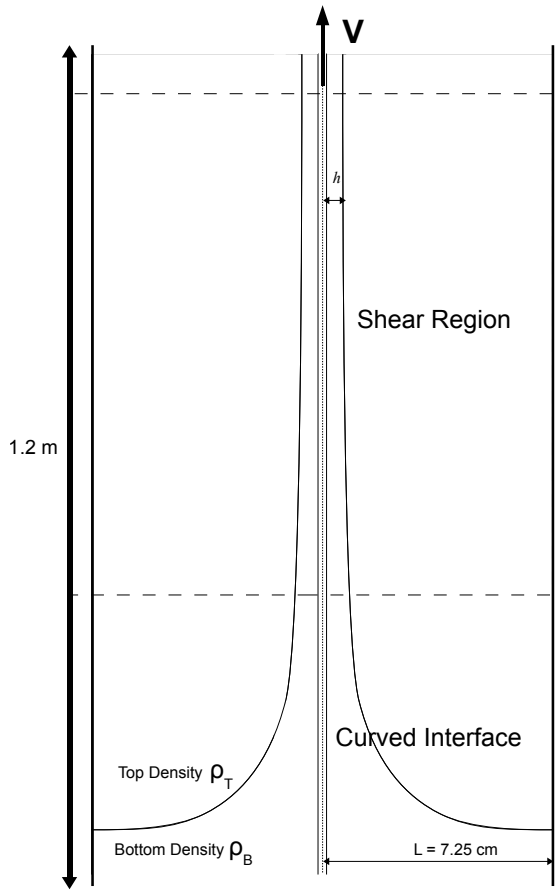

(b) Illustration of flow

Figure 4.2: Experimental design

provided by the Instek GFG-8216A Function Generator. Upon exiting the fluid domain the fiber is redirected downwards into another section of the fluid domain, forming a closed loop with itself. The fiber is redirected by low friction pulleys located both inside and outside of the tank, and the pulleys located inside the tank are isolated from the observation section of the tank so that the rotational motion of the pulleys do not alter the flow. A cylindrical insert is placed inside the observation section of the tank so that the axisymmetric boundary conditions required for the shear solutions are satisfied exactly. See Figure 4.2a for a three dimensional schematic of the experimental tank illustrating these key design features.

In very early designs of the experiment, the fiber did not form a closed loop but instead connected two spools, one of which was rotated in order to tow in the fiber. Some amount of difficulty was experienced with this spool design. First when the towing of the line was halted the rotational inertia of the spools continued to tow the fiber somewhat, which cause slack in the fiber and caused the fiber to come off of the pulleys located inside the tank. Once this occurred the experiment could not be repeated without pouring the tank again. Second, some amount of rotational wobble was observed in both of the spools which caused the fiber to vibrate somewhat. As an alternative to forming the fiber in a closed loop, this difficulty of wobble could have been mitigated by the use of bearings. Thirdly, the amount of fiber wrapped around each spool must necessarily change when the fiber is towed and one spool is releasing the fiber while the other is pulling in the fiber, which means that in order to achieve a constant towing speed with the two-spool design, the rotational speed of the towing spool must be varied at a rate in order to account for this effect.

For these reasons, the experiment was designed so that the fiber would be tied to itself to form a closed loop. In this design, there is very little inertia in the system, only the inertia of the fiber itself and the rotational inertia of the pulleys, which allows for nearly impulsive starting and stopping of the fiber. Additionally, the problem of the wobble of the spools and the induced vibrations is avoided, and it is straightforward to tow the fiber at a constant speed. The disadvantage of the closed loop design is that the fiber must be tied to itself with a knot forming a disruption in the uniform cylindrical shape of the fiber. We attempted to use other means to create the closed loop such as applying heat to the fiber in order to meld the two ends together, however had little success with this method.

As the bottom fluid is entrained by the fiber and carried to the top of the tank,

it accumulates near the free surface and eventually descends downwards back into the observational window, thus disrupting the shear flow. This effect places a limitation on the allowable time duration of the experiment. Various methods were attempted in order to combat this effect, for instance funneling the entrained bottom fluid elsewhere in the tank and suctioning out the entrained bottom fluid with a pump as it reaches the free surface, however these methods never demonstrated complete success.

4.2 Preliminary experiments in water

Initially the experiments were conducted using water as the fluid, with salt dissolved in the bottom fluid to create stratification. In these early water experiments, there was some success in creating the desired parallel flows with the interface oriented nearly vertically in a large region of the observational tank. The interface between the entrained layer of bottom fluid and the ambient fluid was made visible by the shadow graph-method, in which a gradient of the refractive index casts shadows on a background. Figure 4.3 shows a sequence of shadow-graph images in which the interface between the entrained fluid and the ambient fluid can be seen. The interface is nearly vertical at the top of the images which confirms that the flow is nearly parallel there, while this does not hold near the bottom of the images. Additionally, we observed an unexpected phenomenon in some of the experiments in which vortex rings formed around the base of the apparent interface and proceeded to rise. The image sequence in 4.3 shows the formation of multiple vortex rings.

The water experiments were limited by the passage of the knot through the observational window, which provided enough of a disruption to completely destroy the desired laminar boundary layer flow and create an incoherent flow. Thus the effect of the knot placed a limitation on the duration of the experiments, with a longer duration allowed for slower towing speeds. Figure 4.4 shows images of the experiment conducted with water, in which a laminar flow initial develops but is disrupted by the passage of the knot

At most the experiment can last as long as it takes the knot to make one revolution and the length of the fiber loop is 330 cm. The actual time of the experiment may be somewhat less depending on the knot's initial location relative to the experimental window. Thus for a towing speed of 34.5 cm/s as in Figure 4.4, the maximum allowable

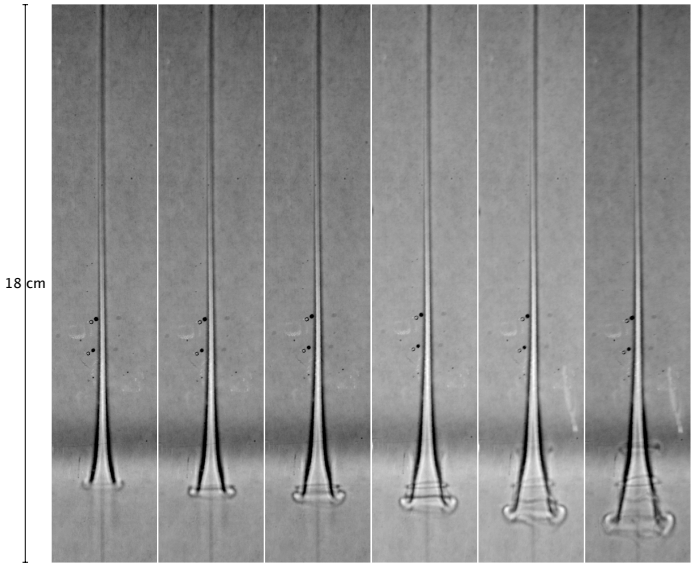

Figure 4.3: Experiment conducted with stratified water on August 5, 2008, run number 3, exhibiting vortex ring formation. The fiber radius is 0.019 cm with a towing speed of 31.1 cm/s. The bottom density is 1.0195 g/cc, and the top density is 0.997 g/cc, giving $\kappa \approx 6,000$ and $Re_h = 187$ (see text for Re_h definition). Frames are shown at 1/4 second intervals.

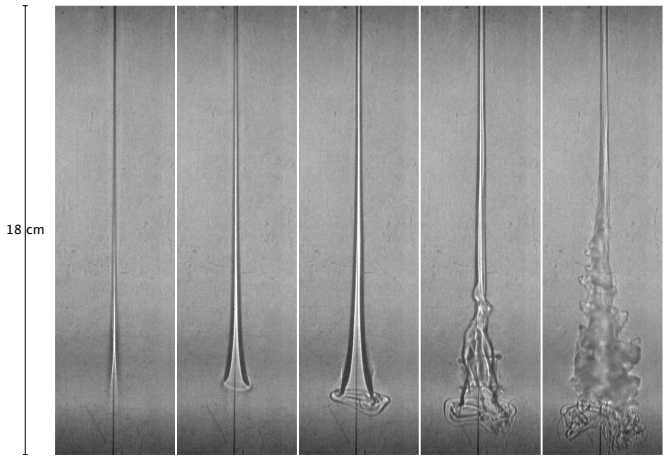

Figure 4.4: Experiment conducted with stratified water on November 6, 2008, run number 13. The fiber radius is 0.019 cm with a towing speed of 34.5 cm/s. The bottom density is 1.0213 g/cc, and the top density is 0.997 g/cc, giving $\kappa \approx 5,900$ and $Re_h = 207$. The passage of the knot destroys the laminar flow that initially develops. Frames are shown at one second intervals.

time for the experiment is 9.5 seconds. For a more typical towing speed of 10 cm/s, the maximum allowable time is 33 seconds.

Despite this time limitation placed on the experiment, the apparent diameter of the shadow-graph image of the entrained layer could be measured at each time-frame and compared to the theoretical predictions. Figure 4.5 shows such a comparison. As seen in Figure 4.5, the collected data exhibits a large spread and it is difficult to draw conclusions regarding comparison to theoretical predictions. The large spread in the data is most likely due to optical distortions in the apparent image of the interface created by the shadow graph-method and the variable refractive index of the fluid.

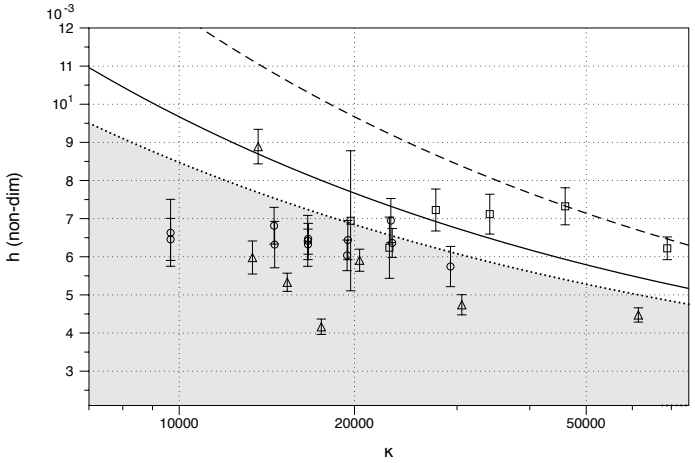

Figure 4.5: Experimental measurements of h (nondimensional) from November 6, 2008 (circles), November 11, 2008 (boxes), and February 16, 2009 (triangles) from the water experiments at a fixed height of 15 cm above the initial interface with $a^* = 0.019$ cm. Error bars show the standard deviation of the h measurements over a suitable time-window. Curves show the theoretical prediction for h_∞ using the semi-infinite theory (dashed line) and the lubrication theory (solid line). Also shown is the neutral stability curve (dotted line) with shading showing the region of stability.

In Chapter 1, the Reynolds number was defined using L the length-scale of the outer boundary, which in these experiment is 9.21 cm. However, in these water experiments the flow will not diffuse through the entire experimental tank until after a diffusive timescale of L^2/μ, which is roughly 2.4 hours for these experiments, whereas the actual timescale of the experiment is limited by the passage of the knot and is always less than one minute. Therefore defining the Reynolds number using L does not give a faithful representation of the water experiments, and so instead we define a Reynolds number

Re_h using the typical size of the entrained layer of $h^*_{ref} = .06$ cm as estimated from the data in Figure 4.5. In the experiments in corn syrup, the flow will diffuse throughout the tank during the timescale of the experiment and so the Reynolds number will be defined in terms of L as in Chapter 1.

4.3 Experiments with corn syrup solutions

In order to combat both effects of the passage of the knot and the optical distortion experienced in the water experiments, we perform the experiments using a solution of corn syrup and water as the fluid, which drastically raises the viscosity. Salt is added to the bottom batch to increase the density and the bottom batch is also dyed to make it visible. With the higher viscosity of corn syrup, the entrained layer becomes substantially larger and the dye allows it to be seen easily, making the interface visible. The disturbances created by the knot are damped by the higher viscosity of the corn syrup solution, whereas the predicted hydrodynamic instabilities exist on much longer timescales than that of the knot passing through the tank. We therefore expected that these hydrodynamic instabilities would potentially be observable in the experiment, and further expected that the passage of the knot could seed such predicted instabilities. However, the small growth rates of the instabilities ultimately prevented them from being observed in the experiment.

The problem of the bottom fluid accumulating near the free surface and eventually descending into the observation window remains in the experiments conducted with corn syrup solutions. Therefore there still remains a limitation on the allowable duration of the experiments though it is much longer than was allowed by the passage of the knot.

4.3.1 Experimental procedure and discussion of uncertainties

As preparation for the experiment, two batches of corn syrup and water solutions were mixed individually with salt added to the batch that would become the bottom fluid in order to raise the density. The two batches were carefully mixed in order to match the viscosities to within 10% of one another, with the viscosities monitored by Zahn cup measurements. A Zahn cup is a type of viscometer in which the draining

time of a fluid is measured and converted into a viscosity. These measurement provided quick, simple monitoring of the viscosity which was indispensable to the experimental preparation. The Zahn cup measurements do not offer a high degree of accuracy, and it was found that the measurements were systematically low by roughly $15\% - 20\%$. However, once the viscosities of the two batches were matched to an acceptable tolerance of 10%, more accurate viscosity measurements were obtained with a falling sphere viscometer that required a substantially longer operational time.

The addition of the salt to the bottom batch raised the density but also raised the viscosity somewhat and therefore it was necessary to add more water in order to compensate for this effect. The addition of water in turn lowered the density, however once both salt and water are added to the bottom batch to match the viscosity of the top fluid, the density of the bottom batch was still higher than that of the top. Thus, as a simple "rule of thumb", salt was used primarily to modify density values and water was used primarily to alter viscosity values.

Once the batches were satisfactorily mixed, the temperature, density, and viscosity of each batch was measured and recorded. The densities were measured with the Anton Paar DMA4500 which is accurate to $5 \times 10^{-5} g/cc$, and the viscosities were measured with the Anton Paar AMVn which has a quoted accuracy of 0.5%. The AMVn viscometer is a falling sphere viscometer, and was calibrated with $G350$ and $G200$ standard fluids at temperatures $20°C$ and $25°C$, and therefore viscosity measurements of each batch may only be taken at these two temperatures. The viscosity of each batch at the measured temperature can then be found by interpolation. Additionally the densitometer requires the measured temperature of the sample as input. Therefore it was desired that we obtain accurate temperature measurements of both batches to be used as input into both the density and viscosity measurements. We set a desired accuracy for the temperature measurements of roughly $0.2°C$ This desired accuracy was not always obtained in our experiments, however we typically obtained a tolerable accuracy of less than about $0.5°C$.

The temperature of each batch was taken with a handheld digital RTD thermometer with a precision of $0.01°C$ or a mercury thermometer with a precision of $0.02°C$. Often the temperature measurements of the two batches differed somewhat (typically by about $0.2°C$), despite the fact that the batches were positioned next to each and the measurements were taken at the same time. This may be due to the fact that the batches were of different volumes and therefore changed temperatures at different

rates even with the same fluctuations in the ambient room temperature. When the two batches were poured into the experimental tank and came into contact there was inevitably an exchange of temperature between the batches. Both batches would eventually reach the same equilibrium temperature, likely to be somewhere in between the two measured temperatures if additional influences such as a change in the ambient room temperature or some heating due to viscous dissipation from fluid motion are neglected. In order to account somewhat for the exchange of temperatures, we measured the density of each sample at its original measured temperature as well as $0.5°C$ less than and greater than this temperature so that an estimate of the coefficient of thermal expansion could be obtained. Finally, this thermal expansion coefficient was used to calculate the densities of each batch at the estimated equilibrium temperature, which was simply the average of the two measured temperatures.

During the time period over which the experiments were conducted, it was found that the digital RTD thermometer was out of calibration, and upon calibration it was found that the thermometer had been giving readings which were higher than the true temperatures by approximately $1.6°C$. Therefore, in the interim in which the RTD thermometer was being calibrated, temperature readings were taken with the mercury thermometer. Upon calibration of the RTD thermometer, it was found to be in agreement with the mercury thermometer up to approximately $0.1°C$. For the experiments conducted before it was realized that the RTD thermometer was inaccurate, we corrected the recorded temperatures by the value $1.6°C$ found during the calibration process. For these experiments we estimate that our temperature uncertainty is roughly $0.5°C$. For the measurements with the calibrated RTD thermometer or the mercury thermometer, in which the measured temperature difference between the two batches is no more than $0.2°C$, we estimate that the uncertainty in the temperature is within the desired range of $0.2°C$.

The high accuracy viscosity measurements were made with the falling sphere viscometer at $20°C$ and $25°C$, and then the viscosity value at the estimated equilibrium temperature was found by interpolation. The viscosity values for the experiments conducted with corn syrup ranged from 1.5 Poise (with a concentration of roughly 30% water by volume) to 25 Poise (pure corn syrup with no water added). Define the

dependence of the viscosity on the temperature by the value

$$\beta = -\frac{1}{\mu_{Avg}}\frac{d\mu}{dT}$$

Within the range of viscosities used, this value measured in $1/^{\circ}C$ was found to lie within the range of $6 - 9 \times 10^{-2}$. Therefore, the tolerable temperature uncertainty of $0.5^{\circ}C$ results in an uncertainty in viscosity of no more than 5% which is smaller than the allowable difference in viscosities between the two batches of 10%. We will take this higher value of 10% as the uncertainty in the viscosity measurements.

The coefficient of thermal expansion is defined as

$$\alpha = -\frac{1}{\rho}\frac{d\rho}{dT}$$

The values of the thermal expansion coefficient measured in $1/^{\circ}C$ were typically in the range of $2 - 6 \times 10^{-4}$. Therefore the desired accuracy of $0.2^{\circ}C$ in the temperature measurements results in an uncertainty in the density measurements of no more than $6 \times 10^{-5} g/cc$ which is nearly the same as the accuracy of the densitometer. The tolerable accuracy of $0.5^{\circ}C$ in the temperature measurements results in an uncertainty in the density measurements of no more than $3 \times 10^{-4} g/cc$. Of greatest importance is the uncertainty in the density difference $\Delta\rho$ of the two batches. The density difference was varied in the experiments within the range of $1 - 30 \times 10^{-3} g/cc$. Therefore, in the worst case scenario with smallest density difference used, $1 \times 10^{-3} g/cc$, and the tolerable temperature uncertainty of $0.5^{\circ}C$, we can expect up to a 30% uncertainty in the measurement of $\Delta\rho$. With the more typical values of $\Delta\rho = 5 \times 10^{-3} g/cc$, even with the tolerable temperature uncertainty of $0.5^{\circ}C$, the uncertainty in $\Delta\rho$ is less than 6%.

Compared to a mixture of water and salt only, it is more difficult to obtain a homogeneous mixture of corn syrup, water, and salt solution through mechanical mixing since the corn syrup increases the viscosity dramatically. Therefore, after the mixing process we took multiple fluid samples from different regions of the fluid batches in order to measure the density and determine to what degree the fluid batch was homogeneous. With a well-mixed batch, the smallest variation in density between these multiple samples was on the order of $1 - 2 \times 10^{-4} g/cc$, indicating that the batch was not completely homogeneous. We found that more stirring did not seem decrease this

variation any further, and therefore we set a tolerable density variation of $2 \times 10^{-4} g/cc$. If the density variation was found to be above this tolerance, we mixed the batches until it was less than the tolerance. Additionally, for a well-mixed batch we observed roughly the same density variation of $1 - 2 \times 10^{-4} g/cc$ from varying the fluid measured within a single $50\,mL$ sample taken in one location of the batch. This indicates that the density of the batch did not only vary on larger spatial scales, but also within the smaller spatial scale of $50\,mL$ sample. The density variation due to inhomogeneity of each batch is nearly the same as the uncertainty in the density measurement with the tolerable temperature uncertainty, and therefore will result in similar uncertainties for $\Delta\rho$: a 30% uncertainty in for the extreme value of $\Delta\rho = 1 \times 10^{-3} g/cc$ and a 6% uncertainty for the more typical value of $\Delta\rho = 5 \times 10^{-3} g/cc$.

The diameter of the fiber was measured with a set of micrometers to a precision of $\pm 0.5/1000''$. Two different fishing lines were used: one with a measured diameter of $15/1000'' \pm 0.5/1000''$ and the other with a measured diameter of $23/1000'' \pm 0.5/1000''$, giving values of the radius a^* of 0.019 ± 0.0006 cm and 0.029 ± 0.0006 cm respectively. In initial experiments the square walls of the tank provided the exterior boundary, which of course was not axisymmetric. For these experiments, we use the inscribed circle to compute the distance L and get $L = 9.21$ cm. In an improvement of the experimental design, a cylindrical insert is placed inside the square tank to match the cylindrical boundary conditions used in the theoretical modeling. In the experiments with the cylindrical insert, $L = 7.25$ cm.

In order to compare the experimental measurements with the theoretical predictions, it is necessary to compute the non-dimensional fiber radius $a = a^*/L$. In the early experiments without the cylindrical insert, in which $a^* = 0.019$ cm and $L = 9.21$ cm, we get $a = 0.0021$. In later experiments in which $a^* = 0.019$ cm and $L = 7.25$ cm, we get $a = 0.0026$, and in experiments in which $a^* = 0.029$ and $L = 7.25$ cm, we get $a = 0.0040$.

4.3.2 Image analysis

Images of the experiment were taken with the 12.1 megapixel Nikon D3 digital SLR camera at the rate of one frame per second. A ruler was attached to the outside experimental tank, in plane with the vertical fiber, so that a physical lengthscale could be ascertained from the images. The images exhibit some amount of spatial distortion

which becomes evident when measuring the number of pixels per given physical length-scale, say 1 cm, on the reference ruler. From the middle of the image to the lowest or highest point in the image the spatial distortion can be as high as 5%, and further does not appear to be symmetric around the center of the image which is most likely due to a misalignment of the optical axis and the physical axis of the lens. Within the middle 50% of the images the distortion is less than in the full image, and normally it is on the order of 2.5%. Since most measurements are made near the middle of the images, the value of 2.5% will be taken as an estimate for the uncertainty in length measurements instead of the more conservative estimate of 5%.

In addition to the ruler attached to the outside of the tank another ruler was temporarily placed into the fluid inside the tank and in plane with the fiber so that effects of magnification due to the difference in the refractive index of the corn syrup solution and air could be assessed. This second ruler was removed from the fluid prior to the experiment so as not to influence the flow.

If d_1 is the distance from the lens to the front face of the experimental tank, d_2 is the distance from the plane of the fiber to the inside of the front face of the tank, and n_1 is the refractive index of the corn syrup solution then the magnification of objects in the plane of the fiber is given by

$$m = \frac{d_1 + d_2}{d_1 + d_2/n_1} \tag{4.1}$$

In the experiment $d_2 = 9.21$ cm and d_2 varied somewhat but was roughly 80 cm in all experiments. Assuming a refrective index of $n_1 = 1.5$ for the corn syrup solution gives an estimate for the magnification of $m = 1.036$, or about 3.6%. The measured values of this magnification vary somewhat, but most typically roughly agree with this estimate of 3.6%, the lowest measurement being 2.8% and the highest being 4.9%. Unfortunately, these measurements of the magnification are only slightly larger than the assumed uncertainty in length measurement of 2.5%, and therefore are not reliable to a high precision. For this reason, a flat magnification of 3.6% in length measurements is assumed for all of the experiments.

The bottom fluid entrained by the fiber is visible in the images since it is dyed. In order to maximize the contrast between this dyed bottom fluid and the ambient top fluid, the RGB images are projected onto the vector in RGB space connecting the two

colors. Thus, the RGB images are converted into an optimal color-scale that is scalar valued.

Often the images are not perfectly aligned with respect to the experimental tank and so the images are rotated by a small angle in order to correct for this. The rotation angle is computed using the vertical fiber as reference and is typically on the order of 1°. Additionally, standard Gaussian and median filtering techniques are applied to the images to smooth out noisy features and render the images more suitable for analysis.

These three processes of color projection, rotation, and filtering are applied in a preprocessing stage so as to save computational expense during analysis. See Figure 4.6 for an image that has been preprocessed in this manner with a false coloring to represent the projected color-scale. It is noted that this color-scale only indicates dye concentration, perceived as color in the images, and does not directly indicate a density field obtained through optical properties such as in the 'synthetic schlieren' method [28].

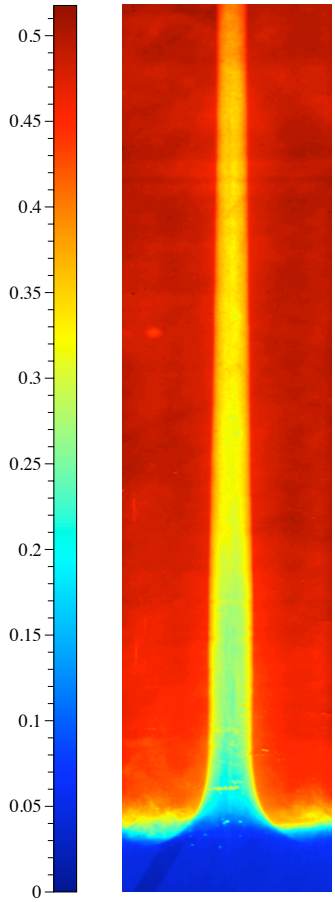

Figure 4.6: An experimental image projected onto the optimal color-scale with false coloring. The image has been compressed in the vertical direction by 30% to exaggerate features. $Re = 2.4$ and $\kappa = 10.2$.

Once the preprocessing stage is complete the images are put through an analysis script. The goals of the analysis script roughly in the order of difficulty are to

1. measure the diameter of the entrained column of bottom fluid as it grows in time.

2. estimate the limiting time value of the entrained column.

3. measure the speed of characteristics for varying values of h for comparison with the lubrication theory.

4. overlay the images with the prediction given by lubrication theory for the time evolution of the interface.

5. overlay the images with the prediction given by the homogeneous density fluid for the time evolution of a marked plane.

Edge detection techniques are utilized in order to measure the diameter of the entrained column. First a line is placed horizontally across the image, perpendicular to the entrained column, along which the scalar color-value (hereafter referred to as color) is measured, thus producing a one dimensional plot of color $C(x)$. The edges of the entrained column would theoretically correspond to the points of discontinuity of the color, however since there is inevitable some amount of optical blur (in additional to the smoothing that is performed intentionally) the edges correspond to points of optimal derivative dC/dx, i.e. points of sharpest color change. In general settings, an edge point corresponds to a point where the gradient magnitude assumes a local maximum in the gradient direction [7]. However in the case under investigation, since the entrained column is oriented nearly vertically the approximate gradient direction is known, i.e. the horizontal direction, and therefore the above one-dimensional analysis is sufficient for edge detection. See Figure 4.10 which illustrates the features of the edge detection.

In primitive versions of the analysis process, the column diameter and thus the radius h were measured at three fixed heights. This method gave fairly accurate measurements at these fixed heights, however the measurements exhibited considerable time-dependent noise that was roughly on the order of 5% of the measurement. By the time that the experiment was necessarily ended due to the descent of the bottom fluid that had accumulated at the free surface, the growth rate of h appeared undetectable relative to this temporal noise - see the left panel of Figure 4.9 - and therefore it was expected that the measurements of h would be near to the time-asymptotic value h_∞ as predicted by the lubrication theory. However, upon comparison with the theoretical prediction it was found that the measured values of h were smaller than the predicted values from lubrication theory by roughly 30%, although the measurements did seem to indicate the scaling trend in κ as predicted by both the lubrication theory and the semi-infinite theory.

Figure 4.7 shows these initial measurements along with the theoretical predictions. The measurements for this figure are from experiments conducted on eight separate dates between August 1, 2009 and October 15, 2009 all with a fiber radius of $a^* = 0.019$ cm.

To complicate matters even further, the measured data seemed to lie along the theoretical neutral stability curve for a range of κ-values, and therefore we hypothesized that it was the stability properties of the system that restrained the entrained layer

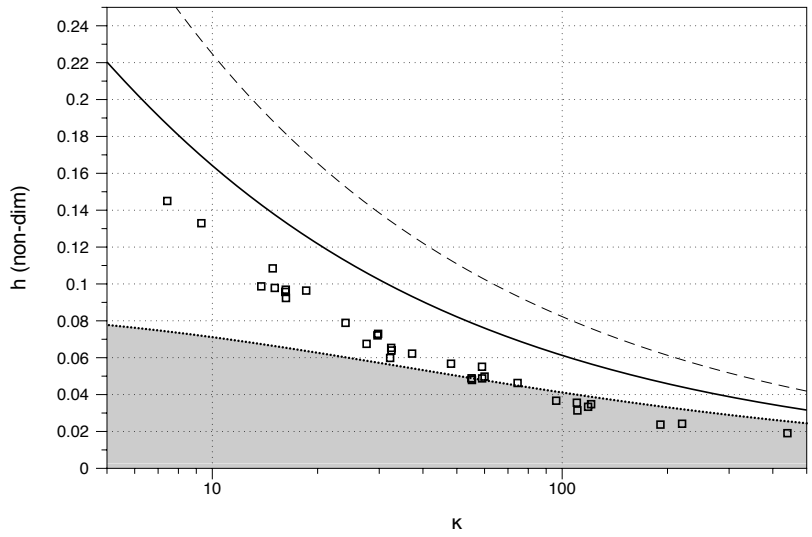

Figure 4.7: Experimental measurements of h (non-dimensional) at the fixed height of 35 cm above the initial interface (boxes), along with the lubrication prediction (solid line), the semi-infinite prediction (dashed line), and the neutral stability curve (dotted line) with the shading indicating the region of stability.

from growing to the full size as predicted by the lubrication theory. This hypothesis was later disconfirmed upon collecting data over a larger range of κ-values, and as seen in Figure 4.7 the entrained layer size is observed to cross the neutral stability threshold for smaller values of κ. This is in important observation since it indicates that for these values of κ the flow eventually develops into an unstable configuration, however the small amplification rates allow the flow to persist for a long duration of time.

Attempts were made to extrapolate the $h(t)$ measurements to longer times in order to determine if the theoretical values could be obtained, however these attempts were problematic even after applying smoothing techniques to the time-dependent data. This was due largely to the fact that in this primitive method, h was only measured at a few heights individually and so there was no spatial smoothing in the vertical direction which would be of clear value since the orientation of the column is vertical. Thus with the primitive version of image analysis, no conclusions could be made regarding the predictive power of the lubrication theory, the semi-infinite domain theory, or the stability theory, other than the observation that the measurements followed the scaling trend in κ which is the same in all three of these theories. Therefore, in order to draw a conclusive comparison to the theory it was necessary to improve the image analysis

techniques used.

Currently the images are processed with a dramatically improved script that relies on the same basic elements of edge detection as in the primitive version. In the current script the edge detection measurement is applied to fifty uniformly spaced heights at a given time and a ninth-degree polynomial is fit to the measurements, thus creating a digital reconstruction of the interface shape at every time. It is then possible to compare the measured time evolution of interface with the predictions from lubrication theory. Figure 4.8 shows the digital reconstruction of the interface at a fixed time.

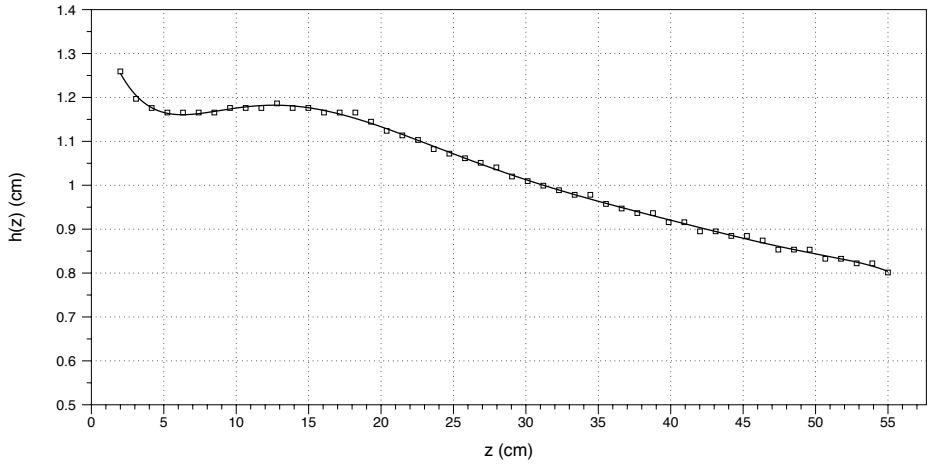

Figure 4.8: Measurements of h at fifty different heights (boxes) to which a ninth degree polynomial is fit (solid line) to digitally reconstruct the shape of the interface. This plot corresponds to the exact image shown in Figure 4.6.

We note that due to the higher complexity of the improved script, it is somewhat less robust than the primitive script and therefore requires more contrast than was previously necessary. Therefore, with the development of the new script, we began adding more dye to the bottom layer so as to dramatically increase the contrast. The improved script was not applied to all of the data taken before this change was implemented due to the lak of sufficient contrast in this old data.

As a first application of the improved script, it is possible to sample the constructed interface $h(z,t)$ at a fixed z-value, resulting in a time-dependent measurement of h at a fixed height much like is done in the primitive method. The important difference is that since the sampling is performed on the reconstructed interface which is a smooth polynomial fit of data taken at several heights, spatial smoothing in the vertical direc-

tion has been fully exploited. The resulting measurements of $h(t)$ exhibit much less temporal noise than in the primitive method. Figure 4.9 shows a comparison of the two measurement techniques for the same experimental image set and demonstrates the benefits of the current technique.

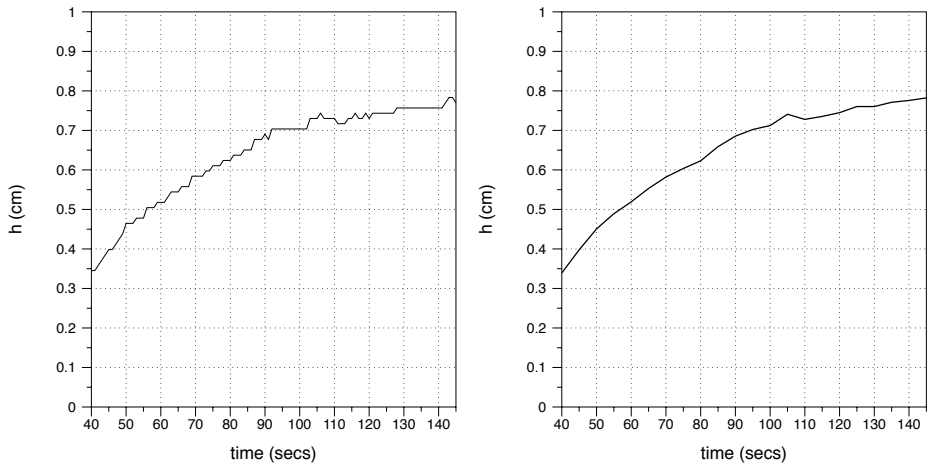

Figure 4.9: Experimental measurements of h using the primitive technique (left) versus the current technique (right). Both measurements are made at a height of 35 cm above the initial interface. The experiment is from October 1, 2008 run number 4.

With the digital reconstruction of the interface, it is also possible to compare measurements with some of the more sophisticated predictions provided by the lubrication theory. The speed of characteristics can be measured by the following method. First fix a value of $h = h_1$ and find the z that gives that particular h-value along the constructed $h(z,t)$ curve. Repeat this at several time values, generating a plot of $z_1(t)$ that corresponds to the single fixed value h_1. The lubrication theory predicts that for fixed h_1, characteristics should travel at a fixed speed (since the characteristics speed is a function of h only), and thus the plot of $z_1(t)$ should be a linear function. The plot of $z_1(t)$ generated from the images, which exhibits some amount of noise, is fit with a linear function and the slope of the linear fit gives the measured value of the characteristics speed dz_1/dt corresponding to h_1. This procedure is then repeated for a range of h values which can be used to generate a plot of the characteristics speeds $dz/dt(h)$.

Figure 4.12 shows the plots generated by this procedure. This method of measuring characteristics speeds does not apply well for very small values of h since the edge

detection exhibits more noise there, nor for very large values of h since for larger h values the interface is much flatter and therefore the z-find is subject to larger errors (since a root-find applied to a flatter function gives larger errors). Therefore, the method should be applied to the h values laying near the middle of the detectible range for a given experiment.

Upon comparing the measured characteristics speeds with the theoretical curve from lubrication theory, it was observed that the measured curve consistently appeared shifted relative to the theoretical curve as to indicate either slower measured characteristics speed or an underestimate of h from the edge detection. By overlaying the positions of the measured edges with the actual image, is was observed that the edge detection method did appear to underestimate the true layer size. In the images, there appeared to be a narrow shell enclosing the entrained layer not picked up by the edge detection - in Figure 4.10 this undetected narrow shell appears as a faint orange color.

These independent observations both seemed to suggest that the edge detection technique was underestimating the measured size of the entrained layer and so various ad-hoc methods were used to attempt to correct for this under-measurement, such as fitting a constant shift to the characteristic speeds measurements. These methods, though adequate for some purposes, were unsatisfying since they relied on a fitting parameter thus rendering suspect agreement found between the measurements and theoretical predictions.

This issue was finally laid to rest with the implementation of a new method of edge detection able to systematically detect the "outer" edge of the entrained layer. Whereas, the "inner" edge detector searched for extrema of the first derivative of the color function across a horizontal slice, it was found that the "outer" edge could be detected through an extrema search of the second derivative. Figure 4.10 illustrates the difference between these two detection methods. Notice that the difference between the two results appears quite small when comparing the lines superimposed on the experimental image of the layer in Figure 4.10.

The difference between the inner and outer edge detection methods, though seemingly small when overlaid with the images, appears to become more pronounced in the characteristics speed measurements as shown in Figure 4.12. Furthermore, the difference between the inner and outer edges does not appear to scale with the size of the layer, but rather seems to be a constant shift *independent* of the value of h. Figure 4.11 demonstrates this constant shift, as the measured value of h varies by more than

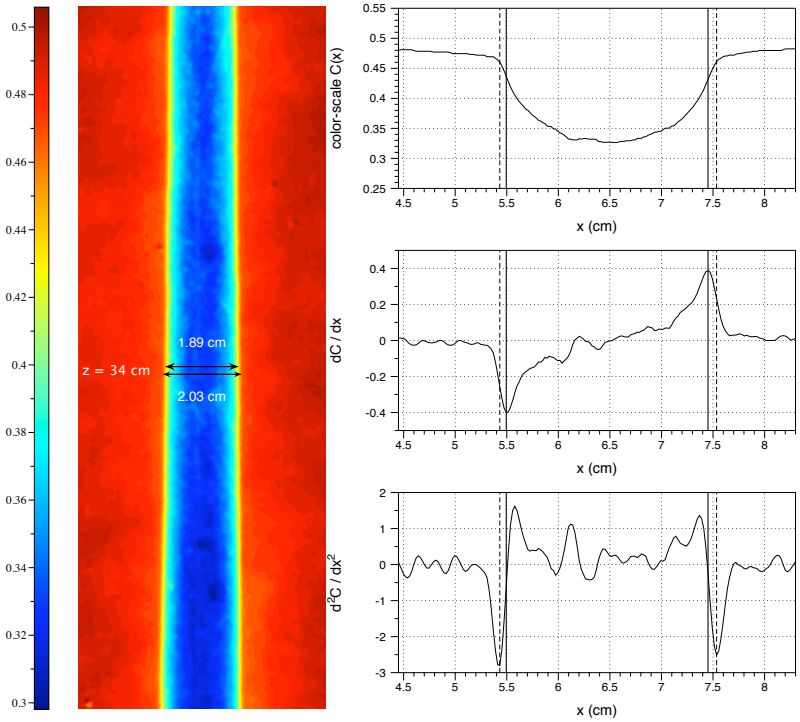

Figure 4.10: Illustration of the edge detection. Left panel: a zoom of an experimental image with a false color scale and two measurements of the layer diameter taken at the same height of 34 cm. The inner layer measurement is on top and the outer layer measurement on bottom. Right: Plot of the color-scale (top), and the first derivative (middle) and second derivative (bottom), along with the position of the layer detected inner edges (solid vertical lines) and outer edges (dashed vertical lines).

a factor of three from the lowest z to the highest z, however the difference between the inner and outer measurements of h remains relatively constant over this entire range. It is unclear if the difference seen by the inner and outer edge detection methods is a product of an optical effect from the varying refractive index in the fluid, or an effect from the smoothing applied to the images and applied to the $C(x)$ plots during the edge detection process, or a different effect.

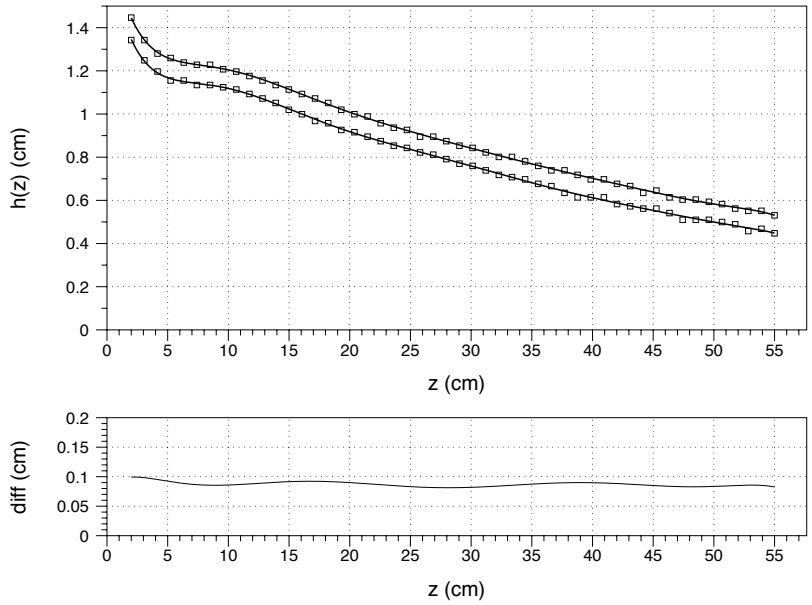

Figure 4.11: Top: $h(z)$ obtained from the measurements of the outer edges and the inner edges. Bottom: outer h minus inner h measurements as z varies.

With the outer edge detection method, the measured characteristics speeds fit closer to the curve predicted by the lubrication theory - see Figure 4.12. Accounting for the uncertainty in the viscosity of roughly 10%, the uncertainty in the density difference which can by up to 30% but is typically much less than 10%, the uncertainty in the non-dimensional parameter κ can be estimated to be roughly 10% (yet again as high as 30% for very small $\Delta\rho$ values). Along with the estimate 2.5% uncertainty in distance measurements, the measurements of the characteristics speeds show agreement with the theoretical predictions to well within this uncertainty range as is shown in Figure 4.12. As seen in Figure 4.12 the theoretical curve passes in between the measurements for the inner edge detection and the outer edge detection, while coming closer to the outer measurements.

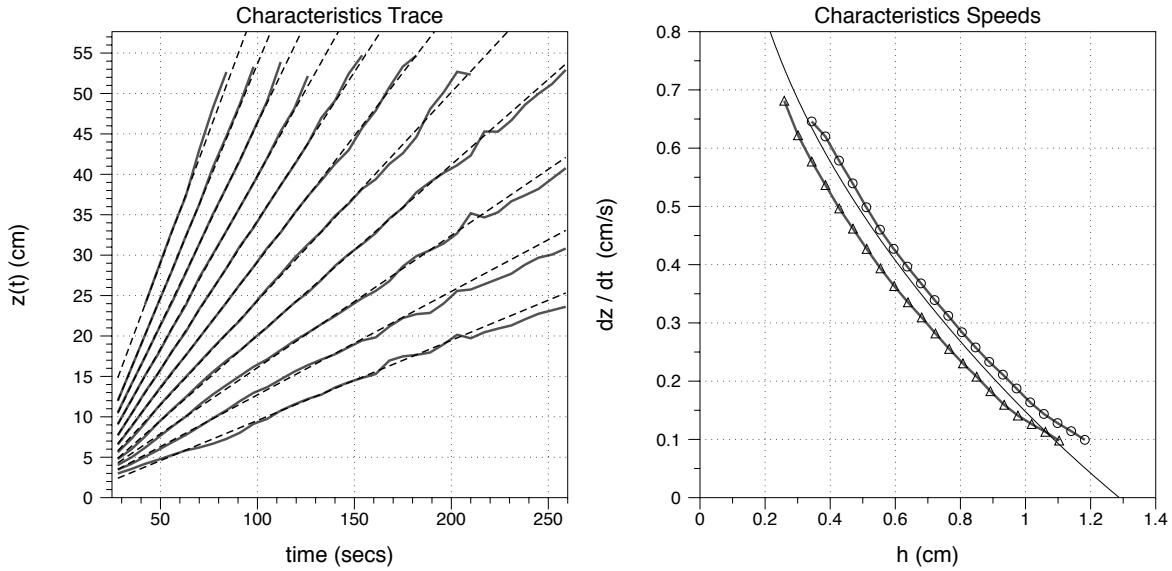

Figure 4.12: Left panel: measurement of $z(t)$ for 11 different fixed values of h (thick gray lines) and a linear fit of each measurement set (fine dashed lines). Right panel: the resulting characteristics speeds measurements for 21 different fixed values of h for the inner edge detection (triangles) and the outer edge detection (circles). The solid black line shows the theoretical curve for the speeds of characteristics. All measurements from experiment performed on December 3, 2009 run number 1.

As compared to the primitive method, the current image analysis method is a significant improvement due to its ability to exploit spatial smoothing through a polynomial fit of several h measurements and its ability to measure the outer edges of the entrained layer. From the use of spatial smoothing, the measurements of $h(t)$ at a fixed height are considerably smoother, as is seen in Figure 4.9, and thus they are more amenable to extrapolation to longer times so that an experimental estimate of the time-asymptotic value h_∞ can be made. Further, this extrapolation can be applied the outer edge measurements since they appear to yield slightly more accurate measurements for the characteristic speeds. The extrapolation is performed by fitting the measured $h(t)$ with a first order series in $1/t$, and then the estimate of h_∞ is given by the constant term in this fit. Figure 4.13 shows this extrapolation procedure applied to $h(t)$ measured at five different heights. Once an estimate of h_∞ is obtained for several fixed heights the median is taken for improved accuracy and error estimates are obtained from the lowest and highest measurements.

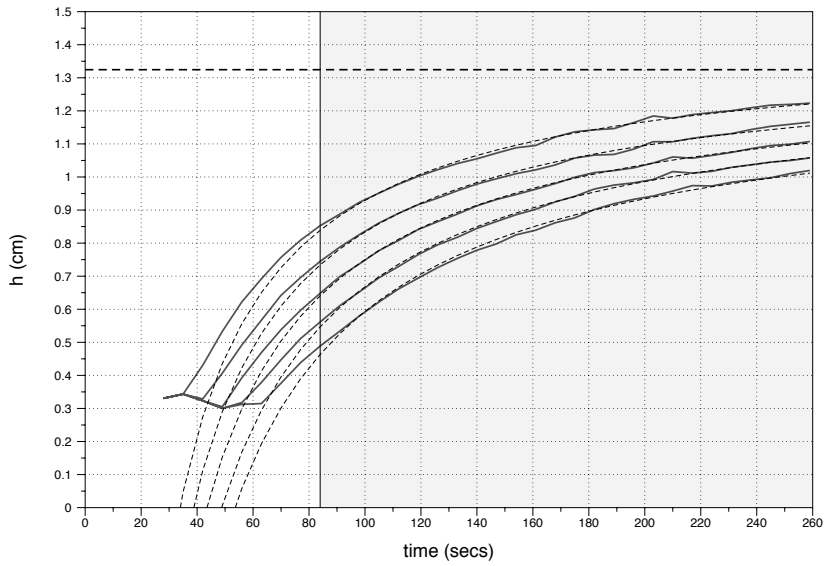

Figure 4.13: h measured from the reconstructed interface at five fixed heights: 20 cm, 25 cm, 30 cm, 35 cm, and 40 cm above the initial interface (thick gray curves) and fit with a first order series in $1/t$ (fine dashed curves). The horizontal dashed line indicates the median of the extrapolated h_∞ from the five curves.

4.4 Comparison of measurements and theory.

With the image analysis techniques greatly improved, it is possible to compare the measured values of h with the theoretical prediction furnished by the lubrication theory (2.24) and the semi-infinite theory (1.19). Plot 4.14 shows final experimental measurements using four different methods: the inner or outer edge detection method evaluated at the final time of the experiment or extrapolated to infinite time. Measurements are shown from experiments in which either $a^* = 0.029$ or $a^* = 0.019$ (as distinguished in the figure caption) all using the cylindrical insert so that $L = 7.25$ cm, which implies that the non-dimensional fiber radius is either $a = 0.0026$ or $a = 0.0040$ for the theoretical calculations. Notice that despite this difference of a factor of roughly 50% in the fiber radius, both the experimental measurements and the theoretical curves show a very small change, indicating a very weak dependence on the fiber radius. Also, it is noted that these measurements were only taken for the experiments conducted after October 1, 2009 in which the dyed bottom fluid showed sufficient contrast, which is the reason that there are fewer data points than in the old measurements shown in Figure 4.7.

As might be expected, the best agreement is seen between the outer edge detection extrapolated to infinite time and the prediction for h_∞ as provided by the lubrication theory (2.24). The prediction provided by the semi-infinite theory is always much larger than the measurements even when extrapolated to infinite time. The outer edge extrapolated data is shown by itself in the right panel of Figure (4.14) with error bars added. The vertical error bars show the spread in h of the measurements as obtained from the five different fixed heights, and the horizontal error bars show an error estimate for the measured κ of 20% for the experiments in which $\Delta\rho < 0.005$ g/cc and 10% for experiments in which $\Delta\rho > 0.005$ g/cc. As seen in this figure, all of the experimental measurements agree with the theoretical predictions within the allowed error tolerance, with the possible exception of the lowest κ-value which is very close.

Another important observation is that many of the final-time observed h-values (given by the diamonds and the squares in the left panel of Figure 4.14) lie within the region of instability. Therefore, all such data points correspond to unstable flow configurations created in the experiment, but once again instability was not observed due to the small amplification rates. The small amplification rates are quantified in Appendix A, in which an upper bound is found on the amplification rate kc_i^* for each

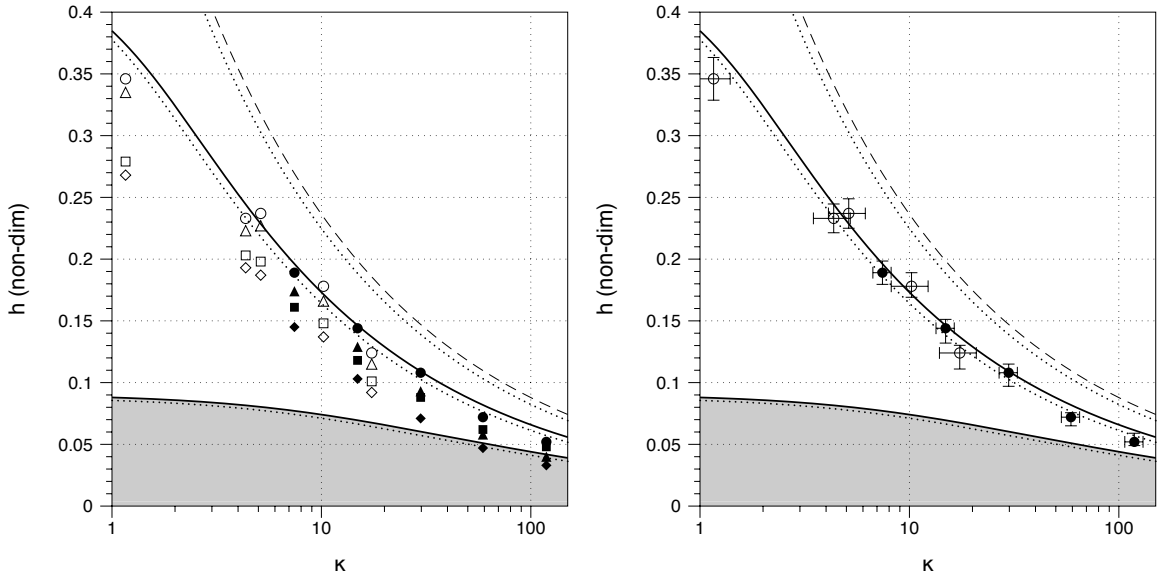

Figure 4.14: Left: Experimental measurements of h (non-dimensional) from inner edges, final time (diamonds); outer edges, final time (squares); inner edges, extrapolated (triangle); and outer edges, extrapolated (circles). The filled points correspond to experiments performed on October 1, 2009 and October 15, 2009 with $a^* = 0.019$ cm and the unfilled points correspond to experiments performed on November 19, 2009 and December 3, 2009 with $a^* = 0.029$ cm. Also shown is the prediction for h_∞ from lubrication theory (solid line) and from semi-infinite theory (dashed line), as well as the neutral stability curve (bottom solid line) with shading to indicate stability. All three of these curves are for $a^* = 0.029$ cm, and the faint dotted curves indicate corresponding curves for $a^* = 0.019$ cm. Right: the Experimental h measurements using the outer edges extrapolated to infinite time with estimated error bars - see the text for discussion of the error bars.

experiment. The resulting upper bounds are typically on the order of $10^{-4}\,1/s$ and the highest amplification rate is $11.1 \times 10^{-4}\,1/s$ which corresponds to experiment 12/3/09, run 2. Using this highest upper bound on the amplification rate, the instability can grow on a timescale of 15 minutes. However, it is possible that the instability will grow to an observable size only after the passage of a large constant multiple of this timescale.

As an even more conclusive experimental verification of the lubrication theory, it is possible to superimpose the solution to the lubrication partial differential equation (2.20) obtained via the method of characteristics upon the experimental images. It is not necessary to solve the partial differential equation in closed form, but rather it is possible to utilize the characteristics mapping (2.22) to advance a plot of $h(z)$ forward in time.

Assume an initial condition $h(z,0) = f(z)$ is given. From this initial condition, form a discretized plot given by n pairs of points (z_i, f_i) where $f_i = f(z_i)$. Then simply advance the z-coordinates via the characteristic map (2.22), so that

$$z_i(t) = z_i(0) + t\ \frac{1}{\pi}\frac{d\hat{J}}{d\zeta}(f_i)$$

Then the pairs of points $(z_i(t), f_i)$ gives a discretized plot of the time dependent solution $h(z,t)$.

The initial condition can be obtained from the digitally reconstructed interface at a suitable time for which the lubrication approximation is satisfied. Figure 4.15 shows an overlay with the experimental images in which the lubrication solution is initialized 30 seconds after the towing starts, so that the layer has not developed to its final form, yet it is already oriented primarily in the vertical direction so as to satisfy the lubrication approximation. The subsequent evolution of the interface shows excellent agreement with the lubrication solution. Also shown is the evolution of a material surface in a homogeneous fluid (2.53) which is observed to depart from the observed interface. The departure is in accordance with intuition since in the experiment the lower fluid has a higher density and therefore would tend to sag relative to a material surface advected in a homogeneous fluid.

The homogeneous fluid thoery (2.53) provides an asymptotic approximation to the evolution of the interface in the experiment for short times. This is demonstrated in

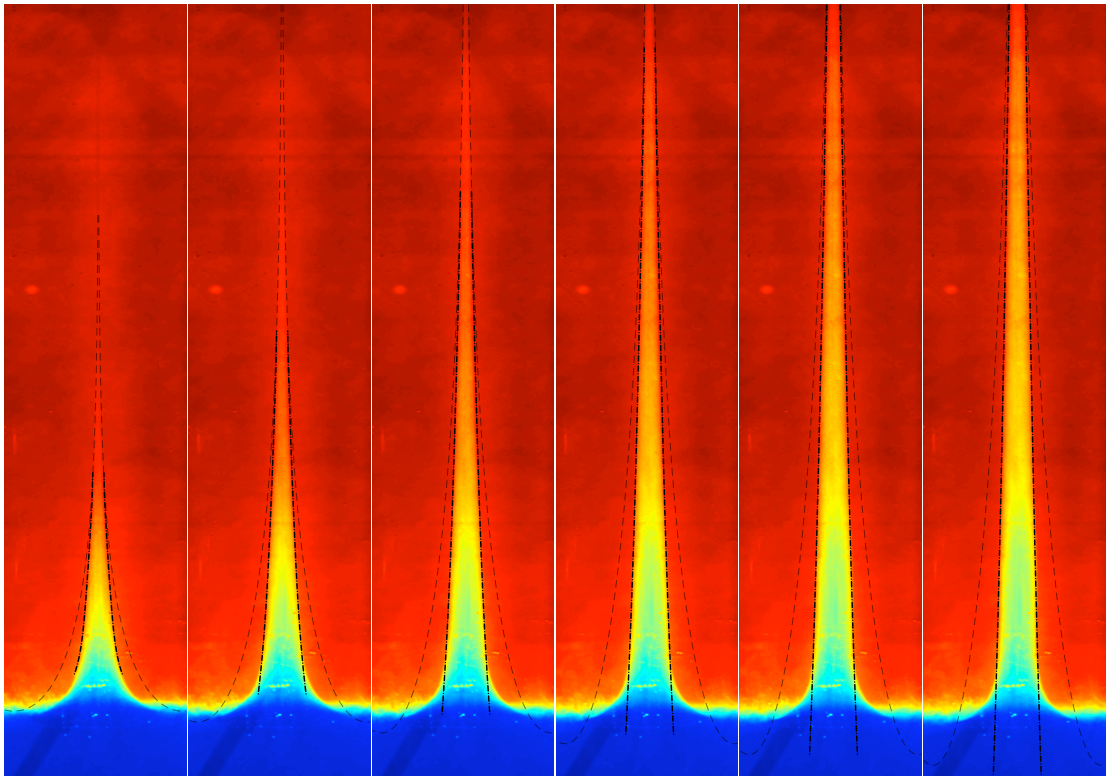

Figure 4.15: Time sequence of experimental images with overlay of the time dependent lubrication solution initialized at the time of the first frame (bold black dot-dash curves), as well as the time dependent solution for a homogeneous fluid (faint sparse dashed curves). Images are from experiment performed on December 3, 2009 run number 1 and are compressed vertically by 30% to exaggerate features. $Re = 2.4$ and $\kappa = 10.2$. The time increment is 20 seconds, beginning 30 seconds after the towing starts and ending 130 seconds after. Physical height of imaged region is 69 cm.

Figure 4.16 in which the evolution of a material surface in a homogeneous fluid (2.53) is overlaid with the experimental image for very short times. The homogeneous theory does show relatively good agreement with the observed interface for very short times and begins to depart rather quickly as the actual interface begins to sag due to the higher density of the bottom fluid.

For the homogeneous fluid theory, Figure 4.16 shows a plot equation (2.53) truncated at the fourth term as well as truncated at the leading order term, which corresponds to the retention of only the steady-state velocity profile (2.52). Surprisingly there is only a very small difference that is discernible between these two truncations, despite the fact that the Reynolds number is 2.4 and therefore not within the Stokes regime. A crude estimate from 2.2 predicts that the effect of the first transient should be roughly of order Re/λ_1, where $\lambda_1 \approx 31.7$. This results in an estimate of a 7.5% error introduced by truncating the first transient mode, whereas the error seen in Figure 2.53 appears to be much less.

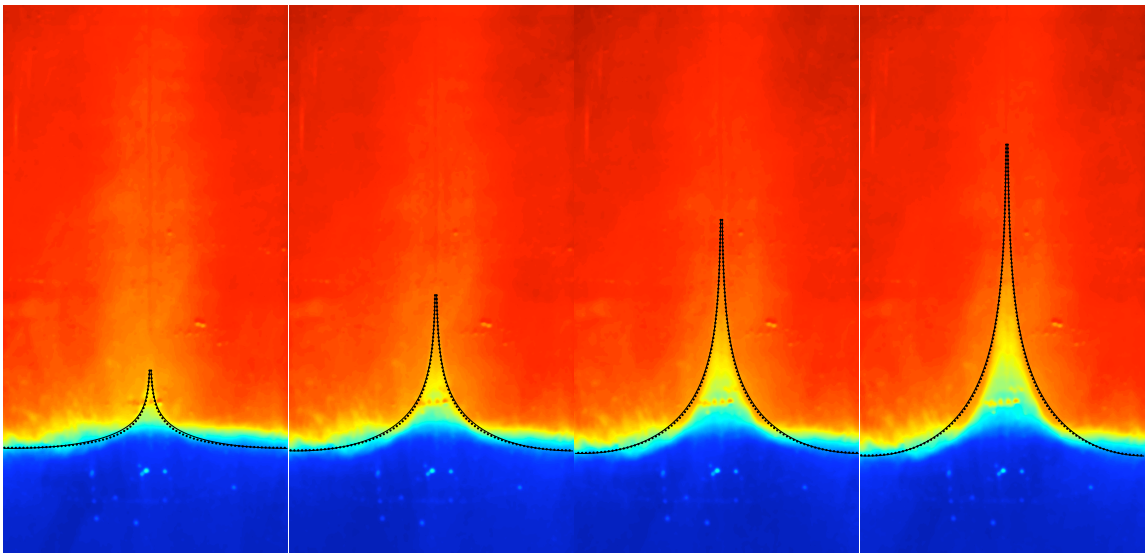

Figure 4.16: Time sequence of experimental images with overlay of the time dependent solution for a homogeneous fluid with only the steady state velocity profile (solid line), as well as with four transient modes (dotted lines). The two curves are only barely distinguishable. Images are from experiment performed on December 3, 2009 run number 1 with $Re = 2.4$ and $\kappa = 10.2$. Time values are 2, 4, 6, and 8 seconds after the towing starts. Physical height of imaged region is 20 cm.

Chapter 5

Summary

This thesis has focused on the exploration of the hydrodynamic properties of flows exhibiting vertical density layering created by moving boundaries, both in two dimensions and in axisymmetric geometry. In 1.2 and 1.3 we gave a theoretical construction of the idealized flows as steady, shear solutions to the Navier-Stokes or Boussinesq equations, and discussed the differences that occur in the semi-infinite domain versus the bounded domain. A simple condition giving a relationship between the size of the entrained layer and the towing velocity (for fixed values of the other parameters) was found through analysis of steady, shear flows in the semi-infinite domain. This relationship was disconfirmed by both experimental measurements and subsequent analysis, however it holds value in that it correctly predicts the scaling relationship between the relevant physical parameters.

We found that in the bounded domain, no such condition was required to hold in order to obtain a steady, shear solution, and in fact an additional condition needed to be *enforced* for there to be a unique solution. We enforced the physical condition of vanishing vertical flux, a condition that holds to a close approximation in the experiments, in order to obtain a two-parameter family of steady, shear solutions parameterized by the non-dimensional κ and h.

In 1.4 we introduced the careful laboratory experiments that were conducted in order to create the shear flows, as these experiments motivated the subsequent analysis in Chapter 2. In 2.1 we used the tools of lubrication theory to determine the dynamical evolution of the flow seen in the experiment. From an initial value problem in which the fluid stratification is stable, this theory captures the evolution of the flow as it tends

to the desired steady, shear flow with vertical density layering, and has been shown to be in excellent agreement with experimental observations in 4.4.

To complement the lubrication model, we also developed theory to model the flow for short times in 2.2. In this section, we solved the time dependent problem of shear flow in homogeneous fluid resulting from an impulsively towed boundary, analogous to the first problem of Stokes, however in a bounded domain and with the condition of vanishing vertical flux enforced at all time. We note that this modification is nontrivial, as it results in an eigenvalue problem with an operator that is a sum of a differential operator and a functional. This short-time theory was confirmed by experimental observations in 4.4. It was observed that for the experimental parameters used, there is a negligible effect produced by retention of the transient modes in the homogeneous theory, which is somewhat contrary to the preliminary estimates in 2.2.

In Chapter 3, the shear solutions were analyzed for their linear stability through a fourth-order eigenvalue problem. A long-wave expansion was used to obtain asymptotic solutions to the eigenvalue problem, and a shooting method was used to determine eigenvalues numerically, the two of which demonstrated agreement in the appropriate asymptotic limit of long waves. A bifurcation was discovered in the (κ, h)-plane, demonstrating a transition from stability to instability as the layer size h crosses a critical length-scale. Further, the analysis of the time-dependent problem in Chapter 2 shows that this unstable length-scale is accessible by the initial value problem and thus by the experiments. Remarkably it was found that the bifurcation behavior is independent of the Reynolds number and the Reynolds enters only as a multiplicative factor in the rate of damping or amplification of disturbances.

Additionally, in 1.2 shear solutions were found that correspond to a smooth approximation to a discontinuous density profile with a small region of sharp density transition. The analysis of these solutions was motivated by the experimental investigation, in which such a transition region is inevitably present between two miscible fluids. Using the numerical shooting method, it was determined that increasing the size of the transition region can diminish the amplification rate of disturbances, although the flow can remain unstable.

In Chapter 4, we discussed the details of the laboratory experiment that was conducted to create the vertically layered shear flows. Preliminary observations from the experiment did not seem to confirm the theoretical predictions from Chapters 1 and 2, and it was only after the image analysis methods were drastically improved that obser-

vations could be successful reconciled with the theoretical predictions. The improved analysis methods showed incontrovertible confirmation of the lubrication model, and good agreement with the short time model, and confirmed that the desired shear flows were successfully created to a close approximation.

The duration of the experiments was limited by the aggregation of the entrained fluid at the free-surface and eventual descent into the observational window. It was observed that in the experiment the size of the entrained layer did cross the critical length-scale to create an unstable configuration, however instabilities were never conclusively observed due to the fact that the magnitude of the instability was too small to be observable under this allowable timescale. Recent efforts have been made to extend the allowable timescale of the experiment so as to observe the instability. We have attempted to funnel and suction the entrained fluid away before it is able to collect on the free-surface, and have been able to extend the duration somewhat, perhaps by a factor of three, but problems still exist and the instability has not yet been observed. The primary goal for future work on this project is to successfully observe the predicted instability in the experiment.

Additionally, a future goal for this project would be to assess the effects of surface tension along the fluid-fluid interface, both theoretically and experimentally. It is likely that the stability properties of the system would be altered, as the resulting problem would bear similarity to the Rayleigh instability - see [22] pp.473-476 - with a reversal of the density field and the addition of viscous entrainment provided by a moving boundary. Additionally, for dominating surface tension, the steady state flow would presumably be that predicted by Landau and Levich in [14], thus providing the potential for comparison with a previously determined result.

Appendix A

Measurements of physical parameters

The following tables show the physical parameters as measured in the experiments organized by the date. Table A.1 shows the parameters that are fixed on a given date: the radius of the fiber a^*, the length-scale of the outer boundary L, the equilibrium temperature T, the dynamic viscosity μ, and the density difference $\Delta\rho$. The equilibrium temperature is found by averaging the temperature measurements of the top batch and the bottom batch. The ‡ indicates temperature measurements which were made with the RTD thermometer when it was out of calibration, and these temperatures are corrected by the value $1.6°C$ found upon calibration. The viscosity measurements are found by the falling sphere viscometer readings taken at $20°C$ and $25°C$, and then interpolated to the equilibrium temperature. The † indicates viscosity measurements not made with the falling sphere viscometer, but instead with the Zahn cups and with a flat 17.5% correction applied.

The date 10/8/09 is marked with a § because on this date the height of the free surface was varied in order to assess its effect on the measurements. We concluded that changing the height of the free surface did not significantly alter measurements.

The Tables A.2 and A.3 show the towing speed of the fiber V, and the non-dimensional parameters κ and Re, for each individual run for the dates 8/1/09 - 8/27/09 (Table A.2) and 10/1/09 - 12/3/09 (Table A.3). Also shown is the maximal amplification rate of disturbances $(kc_i)^*_{max}$ as computed by the numerical shooting method using the measured parameters for each run and the infinite-time entrained layer size h_∞. For this calculation we compute c_i (non-dimensional) in the range of $0 \leq k \leq 10$ (non-dimensional) and find the maximal value of kc_i over this range. This value is then

Date	a^* (cm)	L (cm)	T (°C)	μ (Poise)	$\Delta\rho$ (10^{-3} g/cc)
8/1/09	0.019	9.21	23.5	23.2†	10.2
8/6/09	0.019	9.21	23.2	12.0†	9.6
8/13/09	0.019	9.21	23.3	13.1†	6.6
8/21/09	0.019	9.21	24.8	6.81	8.6
8/27/09	0.019	9.21	22.6	14.0	3.5
10/1/09	0.019	7.25	22.5‡	12.5	10.0
10/8/09§	0.019	7.25	21.9‡	13.3	5.8
10/15/09	0.019	7.25	21.8‡	13.1	5.2
11/19/09	0.029	7.25	22.1‡	14.6	3.4
12/3/09	0.029	7.25	21.8‡	5.52	1.5

Table A.1: Measured physical parameters

converted into a quantity with dimensions $1/s$ via $(kc_i)^* = (kc_i)V/L$. Additionally the dimensional wavenumber k^*_{max} corresponding to maximal growth is shown. The value $(kc_i)^*_{max}$ should be interpreted as an upper bound on the amplification rate for the following reasons:

1. h_∞ is only obtained after infinite time and smaller h-values tend to be less unstable.

2. A small transition region is likely present in the experiment and can render the system less unstable.

In addition, Table A.3 shows the time duration of each experiment τ before the bottom fluid that aggregates at the free-surface descended into the observation window to an extent that the analysis script could not be applied. For the date 10/1/09, Run 3 and Run 6 are shown with the symbol $^\flat$ to indicate that problems that occurred during these runs caused the data set to be unusable by the analysis script, while the more robust but less powerful primitive script was still applied to these runs.

Date / Run	V (cm/s)	κ	Re	$(kc_i)^*_{max}(10^{-4}\,1/s)$	$k^*_{max}(1/cm)$
8/1/09					
Run 1	0.345	111	0.188	0.111	0.456
Run 2	0.691	55.2	0.377	0.418	0.413
Run 3	1.38	27.6	0.755	1.40	0.369
Run 4	2.76	13.8	1.51	4.37	0.347
8/6/09					
Run 1	0.348	191	0.363	0.252	0.565
Run 2	0.692	96.1	0.721	0.892	0.456
Run 3	1.38	48.1	1.44	3.09	0.413
Run 4	2.77	24.0	2.87	10.2	0.369
8/13/09					
Run 1	0.345	121	0.330	0.212	0.499
Run 2	0.695	60.0	0.665	0.757	0.413
8/21/09					
Run 1	0.346	440	0.915	0.723	0.869
Run 2	0.691	220	1.83	2.58	0.608
Run 3	1.38	110	3.66	9.22	4.99
Run 4	2.76	55.1	7.32	32.3	0.413
8/27/09					
Run 1	0.345	74.6	0.378	0.223	0.434
Run 2	0.691	37.2	0.756	0.760	0.391
Run 3	1.39	18.6	1.52	2.49	0.347
Run 4	2.77	9.31	3.03	7.27	0.326

Table A.2: Experimental data for individual runs: 8/1/09 - 8/27/09

Date / Run	V (cm/s)	κ	Re	τ (s)	$(kc_i)^*_{max}(10^{-4}\,1/s)$	$k^*_{max}(1/cm)$
10/1/09						
Run 1	0.347	119	0.274	569	0.242	0.635
Run 2	0.697	59.1	0.550	319	0.866	0.552
Run 3[þ]	1.39	29.7	1.095	-	2.83	0.497
Run 4	2.76	14.9	2.18	126	8.79	0.441
Run 5	1.38	29.8	1.09	192	See Run 3	See Run 3
Run 6[þ]	0.697	59.0	0.550	-	See Run 2	See Run 2
10/8/09[§]						
Run 1	0.690	32.5	0.511	209	0.682	0.497
Run 2	1.38	16.2	1.02	139	2.15	0.441
Run 3	0.692	32.5	0.512	289	See Run 1	See Run 1
Run 4	1.38	16.2	1.02	150	See Run 2	See Run 2
Run 5	0.697	32.2	0.515	316	See Run 1	See Run 1
Run 6	1.39	16.2	1.03	231	See Run 2	See Run 2
10/15/09						
Run 1	2.77	7.43	2.08	158	5.74	0.414
11/19/09						
Run 1	0.693	17.4	0.467	410	0.551	0.441
Run 2	2.77	4.35	1.87	208	3.68	0.386
Run 3	10.4	1.16	7.00	61	8.51	0.331
12/3/09						
Run 1	1.39	10.2	2.43	251	4.46	0.414
Run 2	2.77	5.13	4.85	171	11.1	0.386

Table A.3: Experimental data for individual runs: 10/1/09 - 12/3/09

Appendix B

Experimental diffusivity measurement

A small experiment was performed to measure the rate of diffusivity D of salt in a corn syrup and water solution that is typical of the solutions used in the main experiment. The conductivity was measured for samples of the corn syrup water solution with five different known salinities, so that conductivity could be used to measure salinity when the salinity is unknown. A tank was prepared with a stable stratification of corn syrup water solution, with the two layers having the same corn syrup and water concentrations and the bottom layer having a known salt concentration as well. A density probe was mounted inside the tank, half-way in between the bottom of the tank and the position of the initial, sharp density transition.

In this geometry, the problem of determining the salt concentration inside the tank reduces to a one dimensional diffusion equation for $u(x,t)$

$$\frac{\partial u}{\partial t} = \hat{D}\frac{\partial^2 u}{\partial x^2}$$

with no flux boundary conditions

$$\begin{aligned} \frac{\partial u}{\partial x}(0,t) &= 0 \\ \frac{\partial u}{\partial x}(\pi,t) &= 0 \end{aligned}$$

and a step function initial condition

$$u(x,0) = u_0(x) = \begin{cases} -1 & \text{if} \quad 0 < x < \frac{\pi}{2} \\ 1 & \text{if} \quad \frac{\pi}{2} < x < \pi \end{cases}$$

Here the length has been non-dimensionalized by the height of the tank $L = 40$ cm so that $\hat{D} = \pi^2 D/L^2$, and $u(x,t)$ is the salinity value shifted and scaled so that the range of u is $(-1, 1)$.

This problem can by solved exactly in terms of a Fourier Series by forming an even extension of $u(x,t)$ onto the interval $[-\pi, \pi]$ and solving for this extension in terms of a cosine series. The solution is

$$u(x,t) = \frac{4}{\pi} \sum_{k=1}^{\infty} \frac{(-1)^k}{2k-1} \, e^{-(2k-1)^2 \kappa t} \, \cos{(2k-1)x}$$

The probe is positioned inside the tank at $x = \pi/4$ (non-dimensional). Evaluating the solution at $x = \pi/4$ gives

$$u\left(\frac{\pi}{4}, t\right) = \frac{2\sqrt{2}}{\pi} \sum_{k=1}^{\infty} \frac{(-1)^k}{4k-3} e^{-(4k-3)^2 \kappa t} + \frac{(-1)^k}{4k-1} e^{-(4k-1)^2 \kappa t} \tag{B.1}$$

The experimental measurements have been taken once or twice a day over a span of 80 days. Equation (B.1) is shifted and rescaled to fit the experimentally measured range of salinity values, and then D is chosen to best fit the experimental measurements of salinity. The resulting measured diffusivity value is $1.3 \times 10^{-5} cm^2/s$. This value should be interpreted as an upper bound on the actual diffusivity, since there may be some amount of thermal convection inside the experimental tank that boosts the measured diffusivity value. See Figure B.1.

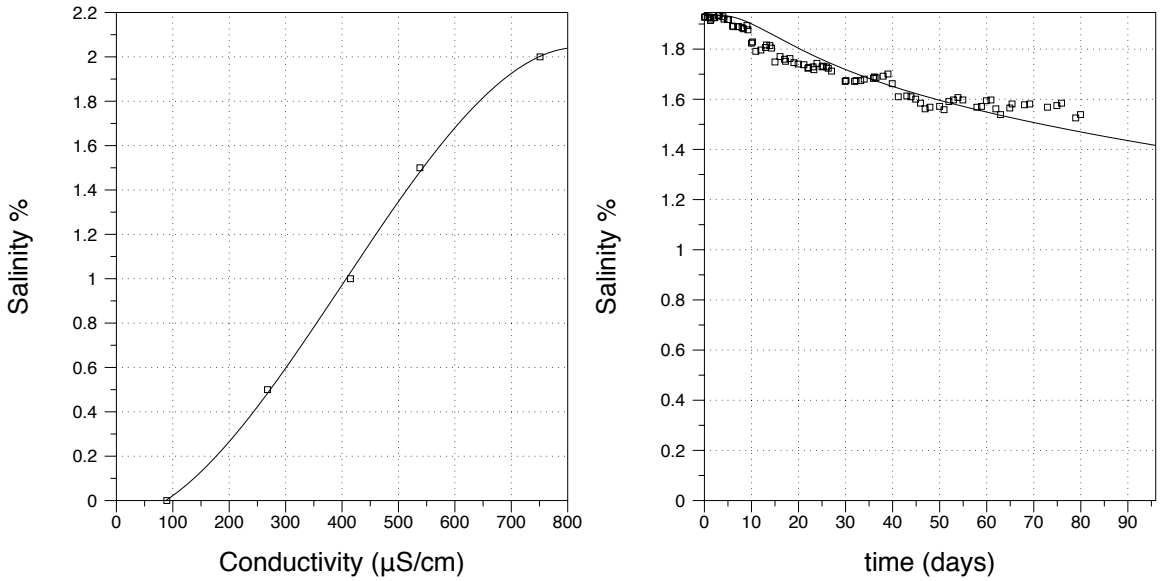

Figure B.1: Left: a cubic fit of salinity versus conductivity readings. Right: experimental measurements of salinity based on the salinity-to-conductivity fit (boxes) and equation (B.1) with D chosen to best fit the measurements.

Appendix C

Two dimensional stability analysis particular solutions

For the two dimensional stability analysis the particular solutions to the inhomogeneous ordinary differential equations evaluated at the points $x = 0$ and $x = 1$ are given by

$$p_L(0) = \frac{i}{420}(1-h)h^5\left\{-28-7h(\kappa-27)+7h^2(15\kappa-61)-h^3(467\kappa-264)\right.$$
$$\left.+903\kappa h^4-790\kappa h^5+256\kappa h^6\right\}$$

$$p'_L(0) = -\frac{i}{60}(1-h)h^4\left\{-20-5h(\kappa-24)+h^2(65\kappa-252)-3h^3(91\kappa-50)\right.$$
$$\left.+511\kappa h^4-438\kappa h^5+140\kappa h^6\right\}$$

$$p_R(1) = \frac{i}{420}(1-h)^5h\left\{-26+197h+h^2(62\kappa-421)-h^3(365\kappa-264)\right.$$
$$\left.+793\kappa h^4-746\kappa h^5+256\kappa h^6\right\}$$

$$p'_R(1) = \frac{i}{60}(1-h)^4h\left\{-14+108h+h^2(32\kappa-234)-h^3(191\kappa-150)\right.$$
$$\left.+421\kappa h^4-402\kappa h^5+140\kappa h^6\right\}$$

Appendix D

Axisymmetric stability analysis: c_1 full expression

The full expression for the first correction c_1 at order $k\,Re$ to the eigenvalue is given by

$$\mu^3 c_1 = \frac{i\kappa}{2304}\pi_1(a^2, h^2, \log a, \log h) + \frac{i\kappa^2}{3072}\pi_2(a^2, h^2, \log a, \log h)$$

where π_1 and π_2 are each polynomials of the four variables $a^2, h^2, \log a,$ and $\log h$. The order of the polynomial π_1 in the variables $a^2, h^2, \log a,$ and $\log h$ is $8, 6, 4,$ and4 respectively, so that π_1 has 768 terms (several of which may be zero). The order of π_2 in these same variables is $8, 8, 4,$ and5, so that π_2 has 1280 terms.

Both coefficient lists for π_1 and π_2 are shown on the proceeding pages. The lists are shown as 4th order tensors that have been flattened. If $A_{i,j,k,l}$ is the coefficient of $a^{2i}h^{2j}\log^k(a)\log^l(h)$ in π_1, then the corresponding coefficient in the flattened array is

$$\tilde{A}[4\cdot 4\cdot 6\cdot i + 4\cdot 4\cdot j + 4\cdot k + l] = A_{i,j,k,l}$$

The coefficients of π_1 are given by

$0, 0, 0, 0, 0, 0, 0, 0, 0, 0, 0, 0, 0, 0, 0, 0, 0, 0, 0, 69, -114, -48, -69, 252, 96, 0, -138, -48, 0, 0, 0, 0, 0, 0,$
$-438, -247, 768, -144, -734, -1150, 792, -144, -134, -576, 144, 0, 0, 0, 0, 0, 588, -658, -216,$
$0, 1131, -514, -216, 0, 426, 48, 0, 0, 0, 0, 0, 0, -150, 260, 0, 0, -360, 260, 0, 0, -186, 0, 0, 0, 0, 0,$
$0, 0, 0, 0, 0, 0, 32, 0, 0, 0, 32, 0, 0, 0, 0, 0, 0, 0, 0, -69, -24, 0, 69, 24, 0, 0, 0, 0, 0, 0, 0, 0, 0, 0, 444, 843,$
$1054, 480, 255, -650, -512, 144, 196, -104, -144, 0, -8, 0, 0, 0, 1584, 624, -3168, 576, 2695,$
$4652, -1488, 288, 500, 1168, -288, 0, 104, 0, 0, 0, -2628, 3386, 504, 0, -3647, 1734, -504, 0,$
$-260, 1008, -576, 0, 168, 576, 0, 0, 600, -1040, 0, 0, 724, 0, 0, 0, -468, 520, 0, 0, -328, 0, 0, 0, 0,$
$0, 0, 0, -96, 0, 0, 0, 32, 0, 0, 0, 64, 0, 0, 0, -6, 268, 96, 0, -385, -308, -96, 0, 128, 168, 0, 0, 0, 0, 0, 0,$
$-2196, -5121, -3666, -1728, 808, 1790, 1832, -432, -172, -248, 576, 0, -72, -144, 0, 0,$
$-1530, 177, 4320, -720, -5177, -8302, -1704, 144, 88, 984, -288, 0, 144, 144, 0, 0, 4632,$
$-6964, 144, 0, 4670, -1412, 1872, 0, -1340, -2400, 0, 0, -72, 0, 0, 0, -900, 1560, 0, 0, -12,$
$-1560, 0, 0, 1456, -520, 0, 0, 0, 0, 0, 0, 0, 0, 0, 0, 96, 0, 0, 0, -160, 0, 0, 0, 0, 0, 0, 0, 24, -317, -120,$
$0, 838, 924, 384, 0, -436, -552, 0, 0, 192, 0, 0, 0, 4344, 10609, 6510, 3120, -4322, -5424,$
$-4168, 288, 1336, 2384, -576, 0, -472, 288, 0, 0, -960, -2008, -960, 0, 7662, 8056, 5856,$
$-576, -3376, -5248, 864, 0, 184, -288, 0, 0, -4008, 7156, -1296, 0, -3438, -1028, -432, 0,$
$3144, 1056, 1152, 0, -360, -1152, 0, 0, 600, -1040, 0, 0, -708, 2080, 0, 0, -764, -520, 0, 0,$
$520, 0, 0, 0, 0, 0, 0, 0, 0, -32, 0, 0, 0, 96, 0, 0, 0, -64, 0, 0, 0, -36, -32, 0, 0, -894, -1144, -576, 0,$
$564, 600, 0, 0, -264, 0, 0, 0, -4296, -10501, -6470, -3120, 6603, 8232, 5232, 288,$
$-2834, -3648, -288, 0, 984, 0, 0, 0, 2790, 2427, -2880, 720, -7864, -3626, -4344, 144,$
$5666, 5168, -144, 0, -1368, 0, 0, 0, 1692, -3674, 1224, 0, 1799, 1926, -1656, 0, -3358,$
$816, 0, 0, 840, 0, 0, 0, -150, 260, 0, 0, 356, -780, 0, 0, -38, 520, 0, 0, -192, 0, 0, 0, 0, 0, 0, 0, 0,$
$0, 0, 0, 0, 0, 0, 0, 0, 0, 0, 0, 0, 0, 0, 24, 353, 120, 0, 469, 608, 384, 0, -332, -216, 0, 0, 0, 0, 0, 0, 0,$
$2124, 4965, 3594, 1728, -4333, -5594, -3344, -432, 2196, 1944, 720, 0, -288, -288,$
$0, 0, -1872, -1176, 2592, -576, 4379, -68, 624, 288, -3252, -912, -576, 0, 864, 288, 0,$
$0, -276, 754, -360, 0, -515, -706, 936, 0, 1388, -528, -576, 0, -576, 576, 0, 0, 0, 0, 0, 0, 0,$

(continued on next page)

(continuation of π_2 coefficients)

$0, 0, 0, 0, 0, 0, 0, 0, 0, 0, 0, 0, 0, 0, 0, 0, 0, 0, 0, 0, 0, 0, 0, 0, 0, 0, 0, -6, -268, -96, 0, -97, -84, -96,$
$0, 76, 0, 0, 0, 72, 0, 0, 0, -420, -799, -1014, -480, 1058, 1374, 904, 144, -584, -280, -288,$
$0, -144, 144, 0, 0, 426, 203, -672, 144, -961, 438, 264, -144, 508, -584, 288, 0, 72, -144,$
$0, 0, 0, 0, 0, 0, 0, 0, 0, 0, 0, 0, 0, 0, 0, 0, 0, 0, 0, 0, 0, 0, 0, 0, 0, 0, 0, 0, 0, 0, 0, 0, 0, 0, 0, 0, 0, 0, 0, 0, 0,$
$0, 0, 0, 0, 0, 0, 0, 0, 0, 0, 65, 24, 0, 0, -20, 0, 0, 0, 0, 0, 0, 0, 0, 0, 0, 0, -65, 106, 48, 0, 20, -40, 0,$
$0, 0, 0, 0, 0, 0, 0, 0, 0, 0, 0, 0, 0, 0, 0, 0, 0, 0, 0, 0, 0, 0, 0, 0, 0, 0, 0, 0, 0, 0, 0, 0, 0, 0, 0, 0, 0, 0, 0, 0, 0,$
$0, 0, 0, 0, 0, 0, 0, 0, 0, 0, 0, 0, 0, 0, 0, 0, 0, 0, 0, 0, 0, 0, 0, 0, 0, 0, 0, 0, 0, 0, 0$

The coefficients of π_2 are given by

$$
\begin{aligned}
&0, 0, 0, 0, 0, 0, 0, 0, 0, 0, 0, 0, 0, 0, 0, 0, 0, 0, 0, 0, 0, 0, 0, 0, 0, 0, 0, 0, 0, 0, 0, 0, 0, 0, 0, 0, 0, 0, 0, 0, 0, 0,\\
&31, -108, 60, 64, -31, 232, -244, -192, 0, -124, 308, 192, 0, 0, -124, -64, 0, 0, 0, -36, 538,\\
&484, -864, 0, -401, 448, 2172, -672, 0, -514, -1008, 1152, 0, 0, -40, -480, 0, 0, 0, -168,\\
&-1049, 848, 416, 0, 285, -2452, -64, 416, 0, 930, -752, -704, 0, 0, 336, 288, 0, 0, 0, 204, 0,\\
&-360, 0, 0, 37, 568, -136, 0, 0, -566, 248, 224, 0, 0, -320, -224, 0, 0, 0, 0, 0, 0, 0, 0, 110, -236,\\
&0, 0, 0, 298, -236, 0, 0, 0, 172, 0, 0, 0, 0, 0, 0, 0, 0, 0, 0, 0, 0, 0, 0, -24, 0, 0, 0, 0, -24, 0, 0, 0, 0, 0, 0,\\
&0, 0, 0, 0, 0, 0, 0, 0, 0, 0, 0, 0, 0, 0, 0, 0, 0, 0, 0, -62, 92, 64, 0, 62, -216, -128, 0, 0, 124, 64, 0, 0, 0,\\
&0, 0, 0, 0, 0, 312, -449, -1620, -924, -320, 974, 1136, -208, 208, 0, 490, 880, 112, 0, 0, 0, 0,\\
&0, 0, 0, 0, 244, 88, 2112, 0, 12, 192, -3584, -384, 0, 216, 1728, 384, 0, 0, 0, 0, 0, 0, 0, 504,\\
&3147, -2544, -1248, 0, -644, 5796, 2016, -416, 0, -1396, -140, 416, 0, 0, 0, 0, 0, 0, 0, -816,\\
&0, 1440, 0, 0, -74, -1856, 272, 0, 0, 1052, 112, 0, 0, 0, 0, 0, 0, 0, 0, 0, 0, 0, 0, 0, -330, 708, 0, 0,\\
&0, -534, 236, 0, 0, 0, 0, 0, 0, 0, 0, 0, 0, 0, 0, 0, 0, 0, 0, 0, 0, 48, 0, 0, 0, 0, 0, 0, 0, 0, 0, 0, 31, 16, 0, 0,\\
&-31, -16, 0, 0, 0, 0, 0, 0, 0, 0, 0, 0, 0, 0, 0, -276, -476, -592, -256, 0, -265, 328, 552, 128, 0,\\
&-282, -304, -112, 0, 0, -28, -16, 0, 0, 0, -936, 1161, 5508, 2412, 576, -2529, -6884, -2484,\\
&-592, 0, 692, -800, -160, 0, 0, 488, 176, 0, 0, 0, 324, -5818, -4708, -672, 0, 3037, 1352,\\
&-788, 2784, 0, -306, -120, -4320, 0, 0, -76, 1536, 0, 0, 0, -336, -2098, 1696, 832, 0, -542,\\
&-3432, -4480, -832, 0, 510, 3420, 1536, 0, 0, -668, -704, 0, 0, 0, 1224, 0, -2160, 0, 0, 0,\\
&2160, 0, 0, 0, -764, -992, -448, 0, 0, 496, 448, 0, 0, 0, 0, 0, 0, 0, 0, 330, -708, 0, 0, 0, 174,\\
&236, 0, 0, 0, -236, 0, 0, 0, 0, 0, 0, 0, 0, 0, 0, 0, 0, 0, 0, -24, 0, 0, 0, 0, 24, 0, 0, 0, 0, 0, -93, -48, 0, 0,\\
&172, 200, 64, 0, 0, -30, -36, 0, 0, 0, 0, 0, 0, 0, 0, 1104, 2462, 1540, 448, 0, -318, -640,\\
&-912, -256, 0, 236, 848, 384, 0, 0, -128, -128, 0, 0, 0, 624, -743, -3780, -1548, -320,\\
&2578, 9460, 7968, 1568, 0, -3030, -5420, -1632, 0, 0, 576, 384, 0, 0, 0, -576, 10072,\\
&8272, -1152, 0, -5036, -8272, 1728, 0, 0, 3352, 1472, 384, 0, 0, -1024, -384, 0, 0, 0,\\
&-336, -2098, 1696, 832, 0, 2640, 40, 1984, 832, 0, -1226, -3044, -960, 0, 0, 896, 128,\\
&0, 0, 0, -816, 0, 1440, 0, 0, 74, -1024, -272, 0, 0, 636, 656, 0, 0, 0, -384, 0, 0, 0, 0, 0, 0, 0, 0, 0,
\end{aligned}
$$

(continued on next page)

(continuation of π_2 coefficients)

−110, 236, 0, 0, 0, 62, −236, 0, 0, 0, 64, 0, 0, 0, 0, 0, 0, 0, 0, 0, 0, 0, 0, 0, 0, 0, 0, 0, 0, 0, 0, 0, 0, 0, 0,
0, 62, 32, 0, 0, −330, −488, −192, 0, 0, 182, 164, 0, 0, 0, −36, 0, 0, 0, 0, −1656, −3848, −2080,
−512, 0, 1924, 2080, 768, 0, 0, −668, −1008, −160, 0, 0, 376, 160, 0, 0, 0, 624, −743,
−3780, −1548, −320, −1835, −1900, −3324, −288, 0, 2650, 5872, 1152, 0, 0, −1576,
−544, 0, 0, 0, 324, −5818, −4708, −672, 0, 2781, 8064, 2804, −2784, 0, −3662, −3712,
4032, 0, 0, 1656, −1248, 0, 0, 0, 504, 3147, −2544, −1248, 0, −2503, −708, 1728, 416,
0, 1856, 148, −832, 0, 0, −628, 416, 0, 0, 0, 204, 0, −360, 0, 0, −37, 152, 136, 0, 0, −358,
−24, 224, 0, 0, 208, −224, 0, 0, 0, 0, 0, 0, 0, 0, 0, 0, 0, 0, 0, 0, 0, 0, 0, 0, 0, 0, 0, 0, 0, 0, 0, 0, 0, 0,
0, 0, 0, 0, 0, 0, 0, 0, 0, 0, 0, 0, 0, 0, 0, 0, 62, 32, 0, 0, 268, 424, 192, 0, 0, −274, −220, 0, 0, 0,
64, 0, 0, 0, 0, 1104, 2462, 1540, 448, 0, −2144, −2440, −432, 256, 0, 1136, 368, −384,
0, 0, −256, 128, 0, 0, 0, −936, 1161, 5508, 2412, 576, 1368, −4132, −4752, −1712, 0,
−684, 1468, 1520, 0, 0, 384, −384, 0, 0, 0, 0, 244, 88, 2112, 0, −256, −368, −2752, 384,
0, 496, 896, −768, 0, 0, −256, 384, 0, 0, 0, −168, −1049, 848, 416, 0, 764, 756, −1184,
−416, 0, −674, 368, 544, 0, 0, 64, −128, 0, 0, 0, 0, 0, 0, 0, 0, 0, 0, 0, 0, 0, 0, 0, 0, 0, 0, 0, 0, 0, 0,
0, 0, 0, 0, 0, 0, 0, 0, 0, 0, 0, 0, 0, 0, 0, 0, 0, 0, 0, 0, 0, 0, 0, 0, 0, 0, 0, 0, 0, 0, 0, 0, 0, 0, 0, 0, 0, 0, 0, 0,
0, 0, −93, −48, 0, 0, −79, −104, −64, 0, 0, 122, 92, 0, 0, 0, −28, 0, 0, 0, 0, −276, −476, −592,
−256, 0, 741, 856, 216, −128, 0, −546, 32, 272, 0, 0, 36, −144, 0, 0, 0, 312, −449, −1620,
−924, −320, −525, 2104, 2980, 1072, 0, 6, −2308, −1184, 0, 0, 252, 432, 0, 0, 0, −36,
538, 484, −864, 0, −137, −1416, 420, 672, 0, 418, 744, −864, 0, 0, −260, 192, 0, 0, 0, 0,
0, 0, 0, 0, 0, 0, 0, 0, 0, 0, 0, 0, 0, 0, 0, 0, 0, 0, 0, 0, 0, 0, 0, 0, 0, 0, 0, 0, 0, 0, 0, 0, 0, 0, 0, 0, 0, 0, 0,
0, 0, 0, 0, 0, 0, 0, 0, 0, 0, 0, 0, 0, 0, 0, 0, 0, 0, 0, 0, 0, 0, 0, 0, 0, 0, 0, 0, 0, 0, 0, 0, 0, 0, 0, 0, 0, 0, 0,
0, 0, 31, 16, 0, 0, 0, −16, 0, 0, 0, 0, 0, 0, 0, 0, 0, 0, 0, 0, 0, 0, −62, 92, 64, 0, 0, 32, −64, 0, 0, 0, 0,
0, 0, 0, 0, 0, 0, 0, 0, 0, 31, −108, 60, 64, 0, −16, 64, −64, 0, 0, 0, 0, 0, 0, 0, 0, 0, 0, 0, 0, 0, 0, 0, 0,
0, 0, 0, 0, 0, 0, 0, 0, 0, 0, 0, 0, 0, 0, 0, 0, 0, 0, 0, 0, 0, 0, 0, 0, 0, 0, 0, 0, 0, 0, 0, 0, 0, 0, 0, 0, 0, 0, 0, 0,
0, 0, 0, 0, 0, 0, 0, 0, 0, 0, 0, 0, 0, 0, 0, 0, 0, 0, 0, 0, 0, 0, 0, 0, 0, 0, 0, 0, 0, 0, 0, 0, 0, 0, 0, 0, 0, 0, 0, 0,
0, 0, 0, 0, 0, 0, 0, 0, 0, 0, 0, 0, 0, 0, 0

Appendix E

Two-dimensional stability analysis:

Mathematica script

In[588]:=
```
(* For the 3D Axisymmetric calculation; Calculate c1 *)
(* Updated on 6/15/10 to use Thesis formulas *)
ClearAll["Global`*"]

(* Definitions *)
mu = 1 + Log[a] - 2 * a^2 + a^4 (1 - Log[a]);
etaSq = h^2 * (Log[h^2 / a^2] - 1) + a^2;


(* basis functions f1,f2, and the piecewise function psiPW *)
f1 = (r^2 - 1)^2;
f2 = 1 - r^2 * (1 - Log[r^2]);
f1p = D[f1, r];
f2p = D[f2, r] // Simplify;
psi = 1 / 4 * (h^2 - r^2 * (1 - Log[r^2 / h^2]));
psip = D[psi, r] // Simplify;

(*evaluated at a *)
f1a = f1 /. r → a;
f2a = f2 /. r → a;
f1pa = f1p /. r → a;
f2pa = f2p /. r → a;
psia = psi /. r → a;
psipa = psip /. r → a;

(* Wronskians *)
Wf1f2a = Simplify[f1a * f2pa - f2a * f1pa];
Wf1psia = Simplify[f1a * psipa - psia * f1pa];
Wf2psia = Simplify[f2a * psipa - psia * f2pa];

(* f1,f2 evaluated at h *)
f1h = f1 /. r → h;
f2h = f2 /. r → h;

(* gamma *)
det = Simplify[Wf1psia * f2h - Wf2psia * f1h];
gamma = Simplify[-Wf1f2a / det];

(* ratio of b10 to b20 for psi0 *)
b1b20ratio = -(f2a + gamma * psia * f2h) / (f1a + gamma * psia * f1h)  // Simplify;
(* b10, b20 after my own simplification *)
b10 = Log[h^2 / a^2] + h^2 * Log[a^2] - a^2 * Log[h^2];
b20 = -(1 - a^2) * ( (1 + a^2) * Log[h^2 / a^2] - 2 * (h^2 - a^2) );

(* Define psi0 *)
(* psi0 to right *)
psi0R = b10 * f1 + b20 * f2 // Simplify;
psi0pR = D[psi0R, r] // Simplify;
(* psi0(h) *)
psi0h = psi0R /. r → h // PowerExpand // Simplify;
(* psi0 to left *)
psi0L = psi0R + gamma * psi0h * psi // PowerExpand // Simplify;
psi0pL = D[psi0L, r] // PowerExpand // Simplify;

(* Nullspace of A adjoint *)
v1 = 2 a * ( (1 - h^2)^2 * Log[a^2] + 2 * (1 - a^2) * (1 - h^2 + h^2 * Log[h^2]) );
v2 =
  -a^2 * (1 - h^2)^2 * Log[a^2] + (1 - a^2) * ( (1 - h^2) * (h^2 - a^2) + (1 - a^2) * h^2 * Log[h^2] );

(* Expression for c_1 *)
alpha1 = -pLa  + gamma * zeta * psia;
alpha2 = -pLpa + gamma * zeta * psipa;
beta1 = 1 / kappa * 8 * gamma * mu * psia;
beta2 = 1 / kappa * 8 * gamma * mu * psipa;
```

```
c1 = -(alpha1 * v1 + alpha2 * v2) / (beta1 * v1 + beta2 * v2) // Simplify;
(* STILL NEED TO define zeta, pLa, pLpa, pR1, pRp1, zeta, ... *)
```

In[625]:=
```
(* Define zeta *)

Dinv = Inverse[{{f31, f41}, {f3p1, f4p1}}];
tempv = Dinv.{pR1, pRp1};
zeta = {f3h, f4h}.tempv // Simplify;

(* basis functions f3,f4 *)
f3 = (r^2 - a^2)^2;
f4 = a^2 - r^2 (1 - Log[r^2 / a^2]);
f3p = D[f3, r];
f4p = D[f4, r];
(* evaluated at 1 *)
f31 = f3 /. r → 1;
f41 = f4 /. r → 1;
f3p1 = f3p /. r → 1;
f4p1 = f4p /. r → 1;
(* evaluate at h *)
f3h = f3 /. r → h;
f4h = f4 /. r → h;

zeta = zeta // PowerExpand // Simplify;
(* NEED ONLY define pLa,pLpa,pR1,pRp1 now *)

(* KEEP? *)
(* Define b31 and b41 to check the boundary conditions later *)
b341 = -Dinv.{pR1, pRp1};
b31 = b341[[1]] // PowerExpand // Simplify;
b41 = b341[[2]] // PowerExpand // Simplify;
```

In[642]:=
```
(* Define terms for the inhomogeneity in the ODE *)

(* define velocity profile *)
(* Velocity Profile Coefficients from Thesis *)
A1 = 1 - kappa / 4 * etaSq - 2 * a^2 + kappa / 4 * (h^2 - a^2) ^2 +
   a^2 * (a^2 - kappa / 4 * h^2 * (h^2 - a^2 - a^2 * Log[h^2 / a^2]));
A1 = A1 / mu;

A2 = -1 + kappa / 4 * etaSq + a^2 -
   2 * a^2 * Log[a] - kappa / 4 * (a^2 * etaSq - (h^2 - a^2) ^2 * Log[a]);
A2 = A2 / mu;

(* vel profile in entrained region minus the exterior flow *)
wPW = 1 / 4 * kappa * (r^2 - h^2 - 2 * h^2 * Log[r / h]);
(* vel profile in the exterior region *)
wExt = A1 * Log[r] + A2 * (r^2 - 1);
(* velocity profile to right and left *)
wL = wPW + wExt // PowerExpand // Simplify;
wR = wExt // PowerExpand // Simplify;
(* w_E(h) *)
wh = wExt /. r → h // PowerExpand // Simplify;
(* Define L(psi0) to left and right *)
Lpsi0L = D[psi0L, {r, 2}] - 1 / r * D[psi0L, r] // PowerExpand // Simplify;
Lpsi0R = D[psi0R, {r, 2}] - 1 / r * D[psi0R, r] // PowerExpand // Simplify;
(* Define L(wExact) to left and right *)
LwL = D[wL, {r, 2}] - 1 / r * D[wL, r] // PowerExpand // Simplify;
LwR = D[wR, {r, 2}] - 1 / r * D[wR, r] // PowerExpand // Simplify;

(* define c0 *)
c0 = PowerExpand[wh - kappa / gamma];
c0 = Simplify[c0];

(* Define the inhomogeneous part of the ODE for the right and left *)
inhomL = I * (wL - c0) * Lpsi0L - I * LwL * psi0L // PowerExpand // Simplify;
inhomR = I * (wR - c0) * Lpsi0R - I * LwR * psi0R // PowerExpand // Simplify;
```

In[659]:=
```
(* Check the simplificiation of c0 in the thesis *)
muc0Thesis = (1 - kappa / 2 * etaSq) * (1 + Log[h]) - (h^2 + a^2 + a^2 * Log[h^2 / a^2]) + \
              +kappa / 2 * (-h^4 + a^4 + (3 * h^4 + a^4) * Log[h / a]) + \
              +h^2 * a^2 * (1 - 2 * Log[a]) + a^4 * Log[h] + \
              +kappa / 2 * h^2 * a^2 * (h^2 - a^2) + \
              +kappa / 2 * h^2 * a^2 * (-3 * h^2 + a^2 + a^2 * Log[h^2 / a^2]) * Log[h] + \
              +kappa / 2 * h^2 * (h^4 + a^4) * Log[a];

diff = mu * c0 - muc0Thesis // PowerExpand // Simplify
```

Out[660]= 0

In[661]:=
```
(*****************************************************************)
(*****************************************************************)
(********************** SOLVE THE ODE ****************************)
(*****************************************************************)
(*****************************************************************)

(* This step takes a LONG TIME to execute *)
ODE = y''''[r] - 2 / r * y'''[r] + 3 / r^2 * y''[r] - 3 / r^3 * y'[r] ;
pL = y[r] /. DSolve[{ODE == inhomL, y[h] == 0, y'[h] == 0, y''[h] == 0, y'''[h] == 0}, y[r], r][[1]];
pR = y[r] /. DSolve[{ODE == inhomR, y[h] == 0, y'[h] == 0, y''[h] == 0, y'''[h] == 0}, y[r], r][[1]];
pLp = D[pL, r];
pRp = D[pR, r];
(*****************************************************************)
(*****************************************************************)
(********************** SOLVE THE ODE ****************************)
(*****************************************************************)
(*****************************************************************)
```

In[666]:=
```
(* The terms needed *)
pLa  = pL /. r → a  // PowerExpand // Simplify;
pLpa = pLp /. r → a  // PowerExpand // Simplify;
pR1  = pR /. r → 1  // PowerExpand // Simplify;
pRp1 = pRp /. r → 1  // PowerExpand // Simplify;
(* write out c1 *)
c1mu3 = c1 * mu^3 // PowerExpand // Simplify;
```

In[671]:=
```
(* Look at leading order terms of c1mu3 *)
c1mu3 = Collect[c1mu3, kappa];
c1k1 = Coefficient[c1mu3, kappa, 1] // Simplify;
c1k2 = Coefficient[c1mu3, kappa, 2] // Simplify;
(* make sure that is all *)
c1k12 = c1k1 * kappa + c1k2 * kappa^2;
c1mu3 - c1k12  // PowerExpand // Simplify
```

Out[675]= 0

In[676]:=
```
"LEADING ORDER TERMS"
(* kappa^1 a^0 h^2 *)
c1k1a0 = Coefficient[c1k1, a, 0] / I;
c1k1a0h2 = Coefficient[c1k1a0, h, 2] // PowerExpand // Simplify;
(* kappa^1 a^2 h^0 *)
c1k1a2 = Coefficient[c1k1, a, 2] / I;
c1k1a2h0 = Coefficient[c1k1a2, h, 0] // PowerExpand // Simplify;
(* kappa^2 a^0 h^4 *)
c1k2a0 = Coefficient[c1k2, a, 0] / I;
c1k2a0h4 = Coefficient[c1k2a0, h, 4] // PowerExpand // Simplify;
(* kappa^2 a^2 h^2 *)
c1k2a2 = Coefficient[c1k2, a, 2] / I;
c1k2a2h2 = Coefficient[c1k2a2, h, 2] // PowerExpand // Simplify;
(* kappa^2 a^4 h^0 *)
c1k2a4 = Coefficient[c1k2, a, 4] / I;
c1k2a4h0 = Coefficient[c1k2a4, h, 0] // PowerExpand // Simplify;

(* Simplify this *)
c1mu3LO = I * kappa * (c1k1a0h2 * h^2 + c1k1a2h0 * a^2) + I * kappa^2 *
      (c1k2a0h4 * h^4 + c1k2a2h2 * a^2 * h^2 + c1k2a4h0 * a^4)      // PowerExpand // Simplify;

(* Check my simplification *)
eta = a^2 - h^2 + h^2 * Log[h^2 / a^2];
c1mu3S =
  -I * kappa / 6144 * Log[h^2 / a^2] * eta * (92 + 32 * Log[h] - (31 + 16 * Log[h]) * kappa * eta);
c1mu3LO - c1mu3S // PowerExpand // Simplify
```

Out[676]= LEADING ORDER TERMS

Out[690]= 0

In[691]:=
```
"First Correction"

(* Leading order of First Correction since a<<h *)
(* kappa^1 a^0 h^4 *)
c1k1a0 = Coefficient[c1k1, a, 0] / I;
c1k1a0h4 = Coefficient[c1k1a0, h, 4] // PowerExpand // Simplify;
(* kappa^2 a^0 h^6 *)
c1k2a0 = Coefficient[c1k2, a, 0] / I;
c1k2a0h6 = Coefficient[c1k2a0, h, 6] // PowerExpand // Simplify;

(* Higher Order *)
(* kappa^1 a^2 h^2 *)
c1k1a2 = Coefficient[c1k1, a, 2] / I;
c1k1a2h2 = Coefficient[c1k1a2, h, 2] // PowerExpand // Simplify;
(* kappa^1 a^4 h^0 *)
c1k1a4 = Coefficient[c1k1, a, 4] / I;
c1k1a4h0 = Coefficient[c1k1a4, h, 0] // PowerExpand // Simplify;
(* kappa^2 a^2 h^4 *)
c1k2a2 = Coefficient[c1k2, a, 2] / I;
c1k2a2h4 = Coefficient[c1k2a2, h, 4] // PowerExpand // Simplify;
(* kappa^2 a^4 h^2 *)
c1k2a4 = Coefficient[c1k2, a, 4] / I;
c1k2a4h2 = Coefficient[c1k2a4, h, 2] // PowerExpand // Simplify;
(* kappa^2 a^6 h^0 *)
c1k2a6 = Coefficient[c1k2, a, 6] / I;
c1k2a6h0 = Coefficient[c1k2a6, h, 0] // PowerExpand // Simplify;
```

Out[691]= First Correction

In[736]:=
```
(* Write the coefficients of kappa^1 and kappa^2 as polynomials of four variables: a,
h, loga, logh *)
c1k1p = (2304 * c1k1 / I) /. {Log[a] → loga, Log[h] → logh};
c1k2p = (3072 * c1k2 / I) /. {Log[a] → loga, Log[h] → logh};

k1Coeff = CoefficientList[c1k1p, {a^2, h^2, loga, logh}];
k2Coeff = CoefficientList[c1k2p, {a^2, h^2, loga, logh}];

Dimensions[k1Coeff]
Dimensions[k2Coeff]

k1Coeff // Flatten;
k2Coeff // Flatten;

k1Coeff // MatrixForm;
k2Coeff // MatrixForm;
```

Out[740]= {8, 6, 4, 4}

Out[741]= {8, 8, 4, 5}

Appendix F

Axisymmetric stability analysis: Mathematica script

hello

In[588]:=
```
(* For the 3D Axisymmetric calculation; Calculate c1 *)
(* Updated on 6/15/10 to use Thesis formulas *)
ClearAll["Global`*"]

(* Definitions *)
mu = 1 + Log[a] - 2 * a^2 + a^4 (1 - Log[a]);
etaSq = h^2 * (Log[h^2 / a^2] - 1) + a^2;


(* basis functions f1,f2, and the piecewise function psiPW *)
f1 = (r^2 - 1)^2;
f2 = 1 - r^2 * (1 - Log[r^2]);
f1p = D[f1, r];
f2p = D[f2, r] // Simplify;
psi = 1 / 4 * (h^2 - r^2 * (1 - Log[r^2 / h^2]));
psip = D[psi, r] // Simplify;

(*evaluated at a *)
f1a = f1 /. r → a;
f2a = f2 /. r → a;
f1pa = f1p /. r → a;
f2pa = f2p /. r → a;
psia = psi /. r → a;
psipa = psip /. r → a;

(* Wronskians *)
Wf1f2a = Simplify[f1a * f2pa - f2a * f1pa];
Wf1psia = Simplify[f1a * psipa - psia * f1pa];
Wf2psia = Simplify[f2a * psipa - psia * f2pa];

(* f1,f2 evaluated at h *)
f1h = f1 /. r → h;
f2h = f2 /. r → h;

(* gamma *)
det = Simplify[Wf1psia * f2h - Wf2psia * f1h];
gamma = Simplify[-Wf1f2a / det];

(* ratio of b10 to b20 for psi0 *)
b1b20ratio = -(f2a + gamma * psia * f2h) / (f1a + gamma * psia * f1h)  // Simplify;
(* b10, b20 after my own simplification *)
b10 = Log[h^2 / a^2] + h^2 * Log[a^2] - a^2 * Log[h^2];
b20 = -(1 - a^2) * ( (1 + a^2) * Log[h^2 / a^2] - 2 * (h^2 - a^2) );

(* Define psi0 *)
(* psi0 to right *)
psi0R = b10 * f1 + b20 * f2 // Simplify;
psi0pR = D[psi0R, r] // Simplify;
(* psi0(h) *)
psi0h = psi0R /. r → h // PowerExpand // Simplify;
(* psi0 to left *)
psi0L = psi0R + gamma * psi0h * psi // PowerExpand // Simplify;
psi0pL = D[psi0L, r] // PowerExpand // Simplify;

(* Nullspace of A adjoint *)
v1 = 2 a * ( (1 - h^2)^2 * Log[a^2] + 2 * (1 - a^2) * (1 - h^2 + h^2 * Log[h^2]) );
v2 =
  -a^2 * (1 - h^2)^2 * Log[a^2] + (1 - a^2) * ( (1 - h^2) * (h^2 - a^2) + (1 - a^2) * h^2 * Log[h^2] );

(* Expression for c_1 *)
alpha1 = -pLa  + gamma * zeta * psia;
alpha2 = -pLpa + gamma * zeta * psipa;
beta1 = 1 / kappa * 8 * gamma * mu * psia;
beta2 = 1 / kappa * 8 * gamma * mu * psipa;
```

```
c1 = -(alpha1 * v1 + alpha2 * v2) / (beta1 * v1 + beta2 * v2) // Simplify;
(* STILL NEED TO define zeta, pLa, pLpa, pR1, pRp1, zeta, ... *)
```

In[625]:=
```
(* Define zeta *)

Dinv = Inverse[{{f31, f41}, {f3p1, f4p1}}];
tempv = Dinv.{pR1, pRp1};
zeta = {f3h, f4h}.tempv // Simplify;

(* basis functions f3,f4 *)
f3 = (r^2 - a^2)^2;
f4 = a^2 - r^2 (1 - Log[r^2 / a^2]);
f3p = D[f3, r];
f4p = D[f4, r];
(* evaluated at 1 *)
f31 = f3 /. r → 1;
f41 = f4 /. r → 1;
f3p1 = f3p /. r → 1;
f4p1 = f4p /. r → 1;
(* evaluate at h *)
f3h = f3 /. r → h;
f4h = f4 /. r → h;

zeta = zeta // PowerExpand // Simplify;
(* NEED ONLY define pLa,pLpa,pR1,pRp1 now *)

(* KEEP? *)
(* Define b31 and b41 to check the boundary conditions later *)
b341 = -Dinv.{pR1, pRp1};
b31 = b341[[1]] // PowerExpand // Simplify;
b41 = b341[[2]] // PowerExpand // Simplify;
```

In[642]:=
```
(* Define terms for the inhomogeneity in the ODE *)

(* define velocity profile *)
(* Velocity Profile Coefficients from Thesis *)
A1 = 1 - kappa / 4 * etaSq - 2 * a^2 + kappa / 4 * (h^2 - a^2) ^2 +
   a^2 * (a^2 - kappa / 4 * h^2 * (h^2 - a^2 - a^2 * Log[h^2 / a^2]));
A1 = A1 / mu;

A2 = -1 + kappa / 4 * etaSq + a^2 -
   2 * a^2 * Log[a] - kappa / 4 * (a^2 * etaSq - (h^2 - a^2) ^2 * Log[a]);
A2 = A2 / mu;

(* vel profile in entrained region minus the exterior flow *)
wPW = 1 / 4 * kappa * (r^2 - h^2 - 2 * h^2 * Log[r / h]);
(* vel profile in the exterior region *)
wExt = A1 * Log[r] + A2 * (r^2 - 1);
(* velocity profile to right and left *)
wL = wPW + wExt // PowerExpand // Simplify;
wR = wExt // PowerExpand // Simplify;
(* w_E(h) *)
wh = wExt /. r → h // PowerExpand // Simplify;
(* Define L(psi0) to left and right *)
Lpsi0L = D[psi0L, {r, 2}] - 1 / r * D[psi0L, r] // PowerExpand // Simplify;
Lpsi0R = D[psi0R, {r, 2}] - 1 / r * D[psi0R, r] // PowerExpand // Simplify;
(* Define L(wExact) to left and right *)
LwL = D[wL, {r, 2}] - 1 / r * D[wL, r] // PowerExpand // Simplify;
LwR = D[wR, {r, 2}] - 1 / r * D[wR, r] // PowerExpand // Simplify;

(* define c0 *)
c0 = PowerExpand[wh - kappa / gamma];
c0 = Simplify[c0];

(* Define the inhomogeneous part of the ODE for the right and left *)
inhomL = I * (wL - c0) * Lpsi0L - I * LwL * psi0L // PowerExpand // Simplify;
inhomR = I * (wR - c0) * Lpsi0R - I * LwR * psi0R // PowerExpand // Simplify;
```

In[659]:=
```
(* Check the simplificiation of c0 in the thesis *)
muc0Thesis = (1 - kappa / 2 * etaSq) * (1 + Log[h]) - (h^2 + a^2 + a^2 * Log[h^2 / a^2]) + \
              +kappa / 2 * (-h^4 + a^4 + (3 * h^4 + a^4) * Log[h / a]) + \
              +h^2 * a^2 * (1 - 2 * Log[a]) + a^4 * Log[h] + \
              +kappa / 2 * h^2 * a^2 * (h^2 - a^2) + \
              +kappa / 2 * h^2 * a^2 * (-3 * h^2 + a^2 + a^2 * Log[h^2 / a^2]) * Log[h] + \
              +kappa / 2 * h^2 * (h^4 + a^4) * Log[a];

diff = mu * c0 - muc0Thesis // PowerExpand // Simplify
```

Out[660]= 0

In[661]:=
```
(*****************************************************************)
(*****************************************************************)
(********************** SOLVE THE ODE ****************************)
(*****************************************************************)
(*****************************************************************)

(* This step takes a LONG TIME to execute *)
ODE = y''''[r] - 2 / r * y'''[r] + 3 / r^2 * y''[r] - 3 / r^3 * y'[r] ;
pL = y[r] /. DSolve[{ODE == inhomL, y[h] == 0, y'[h] == 0, y''[h] == 0, y'''[h] == 0}, y[r], r][[1]];
pR = y[r] /. DSolve[{ODE == inhomR, y[h] == 0, y'[h] == 0, y''[h] == 0, y'''[h] == 0}, y[r], r][[1]];
pLp = D[pL, r];
pRp = D[pR, r];
(*****************************************************************)
(*****************************************************************)
(********************** SOLVE THE ODE ****************************)
(*****************************************************************)
(*****************************************************************)
```

In[666]:=
```
(* The terms needed *)
pLa  = pL /. r → a  // PowerExpand // Simplify;
pLpa = pLp /. r → a  // PowerExpand // Simplify;
pR1  = pR /. r → 1  // PowerExpand // Simplify;
pRp1 = pRp /. r → 1  // PowerExpand // Simplify;
(* write out c1 *)
c1mu3 = c1 * mu^3 // PowerExpand // Simplify;
```

In[671]:=
```
(* Look at leading order terms of c1mu3 *)
c1mu3 = Collect[c1mu3, kappa];
c1k1 = Coefficient[c1mu3, kappa, 1] // Simplify;
c1k2 = Coefficient[c1mu3, kappa, 2] // Simplify;
(* make sure that is all *)
c1k12 = c1k1 * kappa + c1k2 * kappa^2;
c1mu3 - c1k12  // PowerExpand // Simplify
```

Out[675]= 0

In[676]:=
```
"LEADING ORDER TERMS"
(* kappa^1 a^0 h^2 *)
c1k1a0 = Coefficient[c1k1, a, 0] / I;
c1k1a0h2 = Coefficient[c1k1a0, h, 2] // PowerExpand // Simplify;
(* kappa^1 a^2 h^0 *)
c1k1a2 = Coefficient[c1k1, a, 2] / I;
c1k1a2h0 = Coefficient[c1k1a2, h, 0] // PowerExpand // Simplify;
(* kappa^2 a^0 h^4 *)
c1k2a0 = Coefficient[c1k2, a, 0] / I;
c1k2a0h4 = Coefficient[c1k2a0, h, 4] // PowerExpand // Simplify;
(* kappa^2 a^2 h^2 *)
c1k2a2 = Coefficient[c1k2, a, 2] / I;
c1k2a2h2 = Coefficient[c1k2a2, h, 2] // PowerExpand // Simplify;
(* kappa^2 a^4 h^0 *)
c1k2a4 = Coefficient[c1k2, a, 4] / I;
c1k2a4h0 = Coefficient[c1k2a4, h, 0] // PowerExpand // Simplify;

(* Simplify this *)
c1mu3LO = I * kappa * (c1k1a0h2 * h^2 + c1k1a2h0 * a^2) + I * kappa^2 *
      (c1k2a0h4 * h^4 + c1k2a2h2 * a^2 * h^2 + c1k2a4h0 * a^4)      // PowerExpand // Simplify;

(* Check my simplification *)
eta = a^2 - h^2 + h^2 * Log[h^2 / a^2];
c1mu3S =
  -I * kappa / 6144 * Log[h^2 / a^2] * eta * (92 + 32 * Log[h] - (31 + 16 * Log[h]) * kappa * eta);
c1mu3LO - c1mu3S // PowerExpand // Simplify
```

Out[676]= LEADING ORDER TERMS

Out[690]= 0

In[691]:=
```
"First Correction"

(* Leading order of First Correction since a<<h *)
(* kappa^1 a^0 h^4 *)
c1k1a0 = Coefficient[c1k1, a, 0] / I;
c1k1a0h4 = Coefficient[c1k1a0, h, 4] // PowerExpand // Simplify;
(* kappa^2 a^0 h^6 *)
c1k2a0 = Coefficient[c1k2, a, 0] / I;
c1k2a0h6 = Coefficient[c1k2a0, h, 6] // PowerExpand // Simplify;

(* Higher Order *)
(* kappa^1 a^2 h^2 *)
c1k1a2 = Coefficient[c1k1, a, 2] / I;
c1k1a2h2 = Coefficient[c1k1a2, h, 2] // PowerExpand // Simplify;
(* kappa^1 a^4 h^0 *)
c1k1a4 = Coefficient[c1k1, a, 4] / I;
c1k1a4h0 = Coefficient[c1k1a4, h, 0] // PowerExpand // Simplify;
(* kappa^2 a^2 h^4 *)
c1k2a2 = Coefficient[c1k2, a, 2] / I;
c1k2a2h4 = Coefficient[c1k2a2, h, 4] // PowerExpand // Simplify;
(* kappa^2 a^4 h^2 *)
c1k2a4 = Coefficient[c1k2, a, 4] / I;
c1k2a4h2 = Coefficient[c1k2a4, h, 2] // PowerExpand // Simplify;
(* kappa^2 a^6 h^0 *)
c1k2a6 = Coefficient[c1k2, a, 6] / I;
c1k2a6h0 = Coefficient[c1k2a6, h, 0] // PowerExpand // Simplify;
```

Out[691]= First Correction

In[736]:=
```
(* Write the coefficients of kappa^1 and kappa^2 as polynomials of four variables: a,
h, loga, logh *)
c1k1p = (2304 * c1k1 / I) /. {Log[a] → loga, Log[h] → logh};
c1k2p = (3072 * c1k2 / I) /. {Log[a] → loga, Log[h] → logh};

k1Coeff = CoefficientList[c1k1p, {a^2, h^2, loga, logh}];
k2Coeff = CoefficientList[c1k2p, {a^2, h^2, loga, logh}];

Dimensions[k1Coeff]
Dimensions[k2Coeff]

k1Coeff // Flatten;
k2Coeff // Flatten;

k1Coeff // MatrixForm;
k2Coeff // MatrixForm;
```

Out[740]= {8, 6, 4, 4}

Out[741]= {8, 8, 4, 5}

Bibliography

[1] N. Abaid, D. Adalsteinsson, A. Agyapong, R.M. McLaughlin, *An internal splash: falling spheres in stratified fluids*, Physics of Fluids, **16** (2004), no. 5, 1567-1580.

[2] G. K. Batchelor *An Introduction to Fluid Dynamics*, Cambridge University Press, 2000.

[3] T.B. Benjamin, *Wave formation in laminar flow down an inclined plane*, Journal of Fluid Mechanics **2** (1957), 554-574.

[4] F. Blanchette and W.W. Zhang, *Force balance at the transition from selective withdrawal to viscous entrainment*, Physical Review Letters **102** (2009), 144501.

[5] R. Camassa, C. Falcon, J. Lin, R.M. McLaughlin, R. Parker, *Prolonged residence times for particles settling through stratified miscible fluids in the Stokes regime*, Physics of Fluids **21** (2009), 031702.

[6] R. Camassa, R.M. McLaughlin, M.N.J. Moore, A. Vaidya, *Brachistochrones in potential flow and the connection to Darwin's theorem*, Physics Letters A **372** (2008), 6742-6749.

[7] J. Canny, *A computational approach to edge detection*, IEEE Transactions on Pattern Analysis and Machine Intelligence **8** (1986), 679-698.

[8] A. Davey, *On the numerical solution of difficult eigenvalue problems*, Journal of computational physics **24** (1977), 331-338.

[9] P.G. Drazin and W.H. Reid, *Hydrodynamic stability*, Cambridge University Press, 1981.

[10] C. Dombrowski, B. Lewellyn, A.I. Pesci, J.M. Restrepo, J.O. Kessler, R.E. Goldstein, *Coiling, entrainment, and hydrodynamic coupling of decelerated fluid jets*, Physical Review Letters **95** (2005), 184501.

[11] S. Goldstein, *On the stability of superposed streams of fluid of different densities*, Proceedings of the Royal Society of London. Series A, Containing Papers of a Mathematical and Physical Character **132** (1931), 524-548.

[12] T.W. Kao, *Stability of two-layer viscous stratified flow down an inclined plane*, The Physics of Fluids **8** (1965), 812-820.

[13] T.W. Kao, *Role of the interface in the stability of stratified flow down an inclined plane*, The Physics of Fluids **8** (1965), 2190-2194.

[14] L. Landau and B. Levich, *Dragging of a liquid by a moving plate*, ACTA Physicochimica U.R.S.S. **12** (1942), 42-54.

[15] N.N. Lebedev, *Special functions and their applications*, Dover Publications (1972).

[16] J.R. Lister, *Long-wavelength instability of a line plume*, Journal of Fluid Mechanics **175** (1987), 413-428.

[17] J.R. Lister, *Selective withdrawal from a viscous two-layer system*, Journal of Fluid Mechanics **198** (1989), 231-254.

[18] C.W. Oseen, *Hydrodynamik* (Akademische Verlagsgesellschaft, Leipsizg, 1927).

[19] R. Parker, B. Huff, J. Lin, R. McLaughlin, R. Camassa, *An internal splash: levitation and long transients of falling spheres in stratified fluids*, Poster Presentation, 2006 APS March Meeting, Baltimore, MD.

[20] F. Blanchette, T. Peacock, R. Cousin, *Stability of a stratified fluid with a vertically moving sidewall*, Journal of Fluid Mechanics **609** (2008), 305-317.

[21] A.I. Pesci, M.A. Porter, R.E. Goldstein, *Inertially driven buckling and overturning of jets in a Hele-Shaw cell*, Physical Review E **68** (2003), 056305.

[22] C. Pozrikidis *Introduction to Theoretical and Computational Fluid Dynamics*, Oxford University Press, 1997.

[23] W.M. Sangster, *The stability of stratified flows on nearly vertical slopes*, Dissertation (1964), State University of Iowa.

[24] M.R. Scott, *An initial value method for the eigenvalue problem for systems of ordinary differential equations*, Journal of Computational Physics **12** (1973), 334-347.

[25] D.M. Sloan, *Eigenfunctions of systems of linear ordinary differential equations with separated boundary conditions using Riccati transformations*, Journal of Computational Physics **24** (1977), 320-330.

[26] D.M. Sloan and G. Wilks, *The Ricatti transformation method and the computation of eigenvalues of complex linear differential systems*, Journal of Computational and Applied Mathematics **3** (1977), 195-199.

[27] H.A. Stone, Private Communication, 2008.

[28] B.R. Sutherland, S.B. Dalziel, G.O. Hughes, P.F. Linden, *Visualization and measurement of internal waves by 'synthetic schlieren'. Part 1. Vertically oscillating cylinder*, Journal of Fluid Mechanics **390** (1999), 93-126.

[29] G.I. Taylor, Dispersion of soluble matter in solvent flowing slowly through a tube, Proceedings of the Royal Society of London. Series A, Mathematical and Physical Sciences **219** (1953), 186-203.

[30] G.I. Taylor, *Effect of variation of density on the stability of superposed streams of fluid*, Proceedings of the Royal Society of London. Series A, Containing Papers of a Mathematical and Physical Character **132** (1931), 499-523.

[31] S.A. Thorpe, P.K. Hutt, R. Soulsby, *The effect of horizontal gradients on thermohaline convection*, Journal of Fluid Mechanics **38** (1969), 375-400.

[32] F.G. Tricomi, *Integral Equations*, Dover Publications (1985)

[33] J.S. Turner, *Multicomponent Convection*, Annual Review of Fluid Mechanics **17** (1985), 11-44.

[34] C.S. Yih, *Stability of liquid flow down an inclined plane*, The Physics of Fluids **6** (1963), 321-334.

[35] C.S. Yih, *Instability due to viscosity stratification*, Journal of Fluid Mechanics **27** (1967), 337-352.